Booming Sand Dunes

Thesis by

Nathalie Vriend

In Partial Fulfillment of the Requirements

for the Degree of

Doctor of Philosophy

California Institute of Technology

Pasadena, California

2010

(Defended December 1st, 2009)

Acknowledgements

First and foremost I would like to thank my thesis advisor, Dr. Melany Hunt, for giving me the opportunity to pursue research on this intriguing topic. Despite possible limitations on funding you told me: "we will make it work" and we did. I am forever grateful that you gave me this fantastic opportunity. I learned valuable and important lessons from you along the way, and my growth as an independent researcher has been largely due to your encouragement and feedback. I would also like to express my gratitude to my co-advisor, Dr. Rob Clayton. From the very first day that I set foot on the Caltech campus, you motivated me to pursue my interest in geophysics and welcomed me as an engineer in the geophysics department. You allowed me to use various pieces of geophysical equipment that brought an extra dimension to my thesis research. I embarked on several adventurous geophysical field expeditions with you and I will not likely forget the rocking motion of the Nathaniel B. Palmer, nor the wind-devastated campsite after we came back from Eureka dunes.

I would like to thank Dr. Christopher Earls Brennen for your advice and encouragement on personal matters and toward career decisions. Your door was always open and no, I usually needed more than "only a minute" of your time. I value your opinion very highly and I am grateful that I had the opportunity to interact with you and learn from your wide range of life experiences. I will never forget the "adventure hike" through Rubio Canyon together with you– it was one of the most daunting hikes I ever did. I also would like to thank the other members of my thesis committee, Dr. Chiara Daraio and Dr. Michael Lamb, who took time out of their busy schedules to read my thesis and provide valuable comments and suggestions. Chiara, I enjoyed our coffee breaks and I learned valuable lessons from your experience as a young faculty member and from your extensive knowledge on wave propagation in granular materials.

I also would like to thank other faculty and staff members that provided advice along the way in their specialism. Dr. Norm Brooks, thank you for your patient and clear explanation

on the sieving of sediments. Your knowledge on the details of statistics and sieving was valuable in the beginning stages of my research. Dr. George Rossman, I would like to thank you for your insight on the geochemistry of sand and your offer to use your microscopes to investigate the details of the grains. Dr. Sebastien Leprince, thank you for your patient assistance in understanding the marvels of the COSI-CORR software. John van Deusen, I would like to thank you for your invaluable help in the machine shop, many students benefit from your ability to think along in the design stage. Dr. Tom Heaton, thank you for providing a critical voice on the theoretical part of the model. Cheryl Geer, you are the center of the research group, what would we do without you?

There are a few students that I would like to thank explicitly. Kathy Brantley, your enthusiasm and dedication reactivated and propelled the interest in the topic of booming sand dunes at Caltech. Dr. Angel Ruiz-Angelo, initially you kept the booming research going as a side project and your brawns were invaluable in the field. Natalie Becerra, we shared much time together in the laboratory and in the field and your enthusiasm and positive spirit enlightened every research effort. Field research like this type cannot be done without a large number of volunteers who are helping out and I would like to thank every one of them. Thanks to Patricio, Erin, Daniel, Mike, Vala, Peter, Fu-Ling, Steve, John, Alison, Elizabeth, Mark, Mary, Xiaobai, Tamer, Nithya, Shu-San, Nick, Arjen, Georgie, Carter, Jackson, Michelle, Mathieu, Denis, Matt, Nathan, Eric, Brian, Esperanza, Remco, Marion, Dan, Pablo, Zach, Madeline, Joe, and the dozen students from the UCLA geology class and the three dozen students from the Caltech Ge 1 class for all your hard work in such a hostile and hot environment.

I thoroughly enjoyed my entire time at Caltech and this is largely due to the friendship and support of a few close friends. I especially would like to thank Sam and Dan Daly, Zuleikha Kurji, Harmony Gates and Sally and Thomas Bane with whom I shared many hours together, whether it was a much-needed coffee or lunch break on campus or a board game night with some good homemade food.

Above all I would like to thank my family for this journey together with me. You form the most stable part of my life and you are always there to provide support and a listening ear. To you I dedicate this thesis.

Abstract

"Booming" sand dunes are able to produce low-frequency sound that resembles a pure note from a music instrument. The sound has a dominant audible frequency (70-105 Hz) and several higher harmonics and may be heard from far distances away. A natural or induced avalanche from a slip face of the booming dune triggers the emission that may last for several minutes. There are various references in travel literature to the phenomenon, but to date no scientific explanation covered all field observations.

This thesis introduces a new physical model that describes the phenomenon of booming dunes. The waveguide model explains the selection of the booming frequency and the amplification of the sound in terms of constructive interference in a confined geometry. The frequency of the booming is a direct function of the dimensions and velocities in the waveguide. The higher harmonics are related to the higher modes of propagation in the waveguide.

The experimental validation includes quantitative field research at the booming dunes of the Mojave Desert and Death Valley National Park. Microphone and geophone recordings of the acoustic and seismic emission show a variation of booming frequency in space and time. The analysis of the sensor data quantifies wave propagation characteristics such as speed, dispersion, and nonlinear effects and allows the distinction between the source mechanism of the booming and the booming itself.

The migration of sand dunes results from a complicated interplay between dune building, wind regime, and precipitation. The morphological and morphodynamical characteristics of two field locations are analyzed with various geophysical techniques. Ground-penetrating radar images the subsurface structure of the dunes and reveal a natural, internal layering that is directly related to the history of dune migration. The seismic velocity increases abruptly with depth and gradually increases with downhill position due to compaction. Sand sampling shows local cementation of sand grains within the discrete layers that explains the increase

in velocity and decrease in porosity. The subsurface layering may influence the speed of dune migration and therefore have important consequences on desertification.

The positive qualitative and quantitative correlation between the subsurface layering in the dune and the manifestation of the booming sound implies a close relation between environmental factors and the booming emission. In this thesis, the frequency of booming is correlated with the depth of the waveguide and the seismic velocities. The variability on location and season suggests that the waveguide theory successfully unravels the phenomenon of booming sand dunes.

Contents

List of Figures

List of Tables

Nomenclature

Greek characters

α	compressional wave speed (m/s), page 11
α	constant relating the depth to the speed (–), page 56
β	shear wave speed (m/s), page 11
γ	lop sidedness or skewness (m), page 9
δc	error on the velocity (m/s), page 51
δf_1	error on the calculated booming frequency (Hz), page 51
δf_m	error on the measured booming frequency (Hz), page 51
δH	error on the depth (m), page 51
δh	width of the shear band (m), page 11
δt	error on the radar travel time (s), page 100
δu	relative particle velocity between layers in flow direction (m/s), page 28
δV_r	error on the radar velocity (m/s), page 100
ϵ_{10}	phase lag at interface between medium 1 and 0 (–), page 36
ϵ_{12}	phase lag at interface between medium 1 and 2 (–), page 36
Γ	measure of the inelastic grain-grain collisions (–), page 29
Γ	velocity gradient (m/s/m), page 30
θ	local angle of inclination (–), page 4

θ_m maximum angle of stability (–), page 5

θ_r angle of repose (–), page 5

κ degree of peakedness or kurtosis (m), page 9

λ wavelength (m), page 30

λ Lamé constant (Pa), page 67

λ linear concentration (–), page 26

λ_1 Lamé constant in medium 1 (Pa), page 38

λ_n wavelength of mode n (m), page 36

μ coefficient of kinetic friction (–), page 29

μ central tendency or mean (m), page 9

μ shear modulus (Pa), page 67

ρ density (kg/m^3), page 5

ρ_0 density of the atmosphere (kg/m^3), page 34

ρ_1 density of the surficial layer (kg/m^3), page 34

ρ_2 density of the subsurface half space (kg/m^3), page 34

ρ_a density of the air (kg/m^3), page 27

ρ_p particle density (kg/m^3), page 27

σ degree of sorting or standard deviation (m), page 9

σ normal stress (N/m^2), page 5

τ shear stress (N/m^2), page 5

ϕ internal angle of friction (–), page 5

ϕ trial function (–), page 38

ϕ_{cr} critical angle of refraction (–), page 35

ω_1 angular frequency of mode 1 (rad/s), page 38

ω_n angular frequency of mode n (rad/s), page 38

Latin characters

A constant (m^2), page 68

A local amplitude of booming (–), page 51

A proportionality constant ($m^{\alpha-1}s$), page 56

a longest axis of an ellipse (m), page 123

A_0 maximum amplitude of booming (–), page 51

B constant ($m^{3/2}$), page 70

b shortest axis of an ellipse (m), page 123

BSh steppe climate in the subtropics, page 2

BSk steppe climate in the mid-latitudes, page 2

BWh desert climate in the subtropics, page 2

BWk desert climate in the mid-latitudes, page 2

C volume concentration of packing (–), page 26

c intermediate axis of an ellipse (m), page 123

c speed of sound at the surface (m/s), page 30

c_0 speed of sound of the atmosphere (m/s), page 34

c_1 speed of sound of the surficial layer (m/s), page 34

c_{1A} speed of sound of the surficial layer at point A (m/s), page 39

c_{1i+} velocity c_1(z), with $z = z_{\text{interface}}$ (m/s), page 56

c_2 speed of sound of the subsurface half space (m/s), page 34

c_{2A} speed of sound of the subsurface half space at point A (m/s), page 39

c_{2i-} velocity c_2(z), with $z = z_{\text{interface}}$ (m/s), page 56

c_c characteristic velocity of the coupling wave (m/s), page 32

c_{cd} threshold velocity for the field experiments (m/s), page 32

c_{cl} threshold velocity for the laboratory experiments (m/s), page 32

$C^\star$ maximum volume concentration at closest packing (–), page 26

$c(z)$ speed of sound at depth z (m/s), page 56

D average sand grain diameter (m), page 4

dH change in depth of waveguide (m), page 109

e coefficient of restitution (–), page 29

f booming frequency (Hz), page 13

f function describing elliptical motion (–), page 70

f_1 calculated first mode of booming frequency (Hz), page 51

f_1 frequency of mode 1 (Hz), page 38

f_{bp} burping frequency (Hz), page 13

f_{bt} beating frequency (Hz), page 23

$f_{\text{half,max}}$ maximum frequency of the half width (Hz), page 54

$f_{\text{half,min}}$ minimum frequency of the half width (Hz), page 54

f_m measured first mode of booming frequency (Hz), page 51

f_n frequency of mode n (Hz), page 36

f_{osc} frequency of oscillations (1/s), page 28

f_{peak} peak frequency of booming (Hz), page 54

f_s sampling frequency (Hz), page 128

f_{si} silo music frequency (Hz), page 13

f_{sq} squeaking frequency (Hz), page 11

g gravitational acceleration (m/s^2), page 27

H depth of the subsurface layer (m), page 88

H thickness of the waveguide (m/s), page 34

h thickness of the sheared layer (m), page 30

H_1 lateral horizontal, positive to the right (–), page 73

H_2 longitudinal horizontal, positive downhill (–), page 73

H_A thickness of the waveguide at point A (m), page 39

h_s average height of saltation (m), page 4

k fitting constant (1/s), page 56

k_n wave number of mode n (m^{-1}), page 36

k_r wave number in r-direction (m^{-1}), page 37

k_z wave number in z-direction (m^{-1}), page 37

l_s average length of saltation (m), page 4

m mass of the overburden (kg), page 27

N number of shear bands (–), page 11

n mode n (–), page 36

n mode number (–), page 13

P confining pressure (Pa), page 31

P normal dispersive stress (kg m/s^2), page 27

q_1 dimensionless factor in the expression for the shear stress (–), page 29

R reflection coefficient (–), page 35

r radial coordinate (m), page 37

r_1 ratios of length r_1 = b/a (–), page 123

r_2 ratios of length r_2 = c/b (–), page 123

Re Reynolds number Re (–), page 27

s position of mass during free fall (m), page 28

St Stokes number St (–), page 27

t time of free fall (s), page 28

T transmission coefficient (–), page 35

t time (s), page 37

t_0 two-way travel time (s), page 88

u velocity of free fall (m/s), page 28

U shear velocity (m/s), page 22

U_a maximum velocity of avalanching grains (m/s), page 30

U_c critical displacement velocity (m/s), page 27

U_n forcing function (–), page 68

$u^\star$ minimum surface friction speed (m/s), page 4

u_z displacement (m), page 67

V phase speed of the acoustic emission (m/s), page 72

V vertical direction, positive away from the dune (–), page 73

V_1 phase speed within medium 1 (m/s), page 38

v_{bar} average random fluctuation velocity (m/s), page 28

V_g group speed of the Rayleigh wave (m/s), page 70

V_{gb} group speed of the burping emission (m/s), page 76

V_{int} phase speed along the interface (m/s), page 35

V_p pestle velocity (m/s), page 11

V_p phase speed of the Rayleigh wave (m/s), page 68

V_{pb} phase speed of the burping emission (m/s), page 76

V_r radar ground velocity (m/s), page 88

V_s speed of the slide (m/s), page 52

V_{sur} phase speed along the surface (m/s), page 37

Z number of atoms (–), page 91

z depth coordinate (m), page 37

Chapter 1

Introduction

1.1 Characteristics of Desert, Dunes and Sand

1.1.1 Deserts

Desertification is defined as the loss of vegetation and soil moisture in arid and semiarid regions due to climatic variations and human activity. Drought currently affects 41% of land surfaces in Asia, Africa, the Americas and southern Europe, inhabited by one-fifth of the world's population. This number may rise to 70% in 2025 (Nations, 2009). The social and economical impact of expanding deserts not only limits the production of crops and the availability of freshwater, but also influences the environment, the infrastructure and the economy of an entire region as well.

Although more than 70% of the Earth is covered with it, water is not abundant on all of the remaining land surface. Dry climate is the most frequently occurring type of climate– almost one-third of the Earth's land surface falls into this category. The arid regions have an annual evaporation that exceeds the annual precipitation. The Köppen-Geiger climate classification (figure 1.1) is the most widely used climate classification system (Peel *et al.*, 2007) and identifies five major climates based on average monthly and annual temperature and precipitation, the seasonality of precipitation and the native vegetation of a region.

Approximately 14% of Earth's surface is classified as a desert dry climate; it is also the most common climate type by land area (Peel *et al.*, 2007). The desert dry climate (BWh) is part of a subdivision of class B in the Köppen-Geiger system:

- Wh: desert climate in the subtropics, average temperature $>$ 18°C
- Wk: desert climate in the midlatitudes, average temperature $<$ 18°C

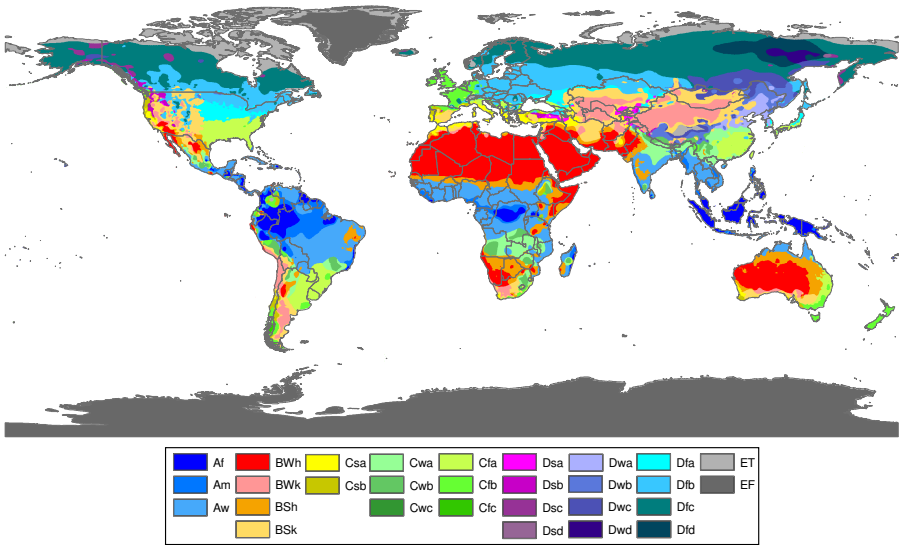

Figure 1.1: Köppen-Geiger climate type map of the Earth. Reproduced with permission from Peel *et al.* (2007). Major climates classes include tropical humid climate (class A), dry (arid, $<$ 250 mm rainfall/year and semiarid, 250-500 mm rainfall/year) climate (class B), temperate/mild mid-latitude climate (class C), continental/severe mid latitude climate (class D), polar climate (class E).

- Sh: steppe climate in the subtropics, average temperature $>$ 18°C
- Sk: steppe climate in the midlatitudes, average temperature $<$ 18°C

"Trade wind deserts" (type BWh), such as the Sahara desert, exist due to dissipating cloud cover and increased sunlight impact in the subtropics. The Sonoran desert is an example of a "midlatitude desert" (type BWk) that forms in interior basins far from oceans. Other types of deserts are the "rain shadow desert" on the leeward side of tall mountains, "coastal deserts" on western edges of continents due to cold ocean currents parallelling the coast, "monsoon deserts" due to seasonal temperature and precipitation variations and "polar deserts" in arctic regions.

The polar Arctic and Antarctic deserts are the largest single deserts on Earth, the Sahara trails far behind in third position. Only 20% of Earth's deserts are actually covered by sand– bedrock and gravel plains or ice fields are far more common. Aeolian, wind-driven, processes are the common denominator in creating desert landscapes and sand dunes are one of the most impressive features of the wind.

1.1.2 Dunes

A single dune can be defined as a mound or hill of sand that rises to a single summit (Bagnold, 1941, p. 188). Dunes are stable on a surface without topography, but also occur in areas with surface relief–surrounding mountains may directly influence the wind regime and the sand transport. Isolated dunes exist individually, but dunes may collectively form a colony or dune chain.

Dunes form under the influence of water or wind. Subaqueous dunes are sand dunes that form underwater under the action of water currents. These dunes can obtain a wavelength of up to 220 meter and a height of up to 10 meters (Barnard *et al.*, 2006). Back beach or coastal sand dunes are usually lined up parallel to the shoreline. Onshore winds provide sand blown off the beach and vegetation increases the dune stability and prevents the dune from migrating inland. The sand grains usually are eroded sea shells and therefore have a large calcium carbonate component. Ergs are large, wind-laid, sand dunes occurring in vast sand seas associated with ancient lake or sea beds. Several prerequisites need to be met to create and sustain inland sand dunes: quantities of loose sand, usually quartz and/or feldspar, with vegetation should be available and the wind source should be energetic enough to move the grains. Obstacles or topography are not necessary for sand accumulation. Topography will promote momentum loss of grains thus enhancing settling, but self-accumulation is possible on flat surfaces. Even an existing dune can still be subject to a shift in its location and size based on the interaction with the wind.

Dune building

Whether sediment can move and form dunes depends on the particle size or weight, and the wind speed. The threshold curve relates the particle size to the minimum wind speed (or the shear stress exerted on the surface) that is required to initiate motion. The minimum surface friction speed $u^\star \approx 0.21$ m/s (Bagnold, 1941) on Earth occurs at $D \approx 100$ μm and hence sand particles around this range are most easily transported. Transport of sediment occurs due to suspension, saltation and impact creep and depends strongly on size. The fine sediments, colloids, clay and silt particles with $D < 3.9$ μm, spray into the air where turbulent eddies keep them lifted in *suspension*. *Saltation* is a process where a sediment particle quivers and rolls along several grain diameters before it flies in the air at a steep

angle. The particle is too heavy to remain in this state and is carried back to the surface by the wind where it impacts and bounces back impacts and bounces back into the air. The average height for saltating particles is $h_s \approx$ 3 m and the length between bounces is $l_s \approx$ 3 m (Bagnold, 1941). Sand-size particles with 62.5 μm $< D <$ 2 mm may be transported by the wind in saltation depending on wind speed. In *impact creep* the particles are too large to be lifted from the ground, but they can roll, slide and be pushed along the ground by the wind. Impact creep is based on surface traction and may occur after impact of particles by saltation on stationary sediments.

A stationary dune has a rate of sand removal due to suspension, saltation and impact creep processes, equal to the total deposition of sand supplied by infinite upstream sources. For a non-zero divergence in sand flux, sand is effectively removed or added to the system and the dune migrates in space (Bagnold, 1941). The divergence depends on the specific weight of sand, the distance of migration of the dune and the local angle of inclination θ.

The local angle of inclination, θ, is directly dependent on the angle of repose, θ_r. The mechanical concept of the angle of repose prescribes the angle of a cone-shaped heap of sand when grains are dropped on a surface (Kakalios, 2004). The angle between the horizontal and the free surface is the maximum angle of stability θ_m. For smaller inclination angles ($\theta < \theta_m$), the random configuration of grains balances contact normal forces, intergrain friction and gravity. For larger angles ($\theta > \theta_m$) the gravity overcomes the frictional drag and triggers an avalanche down the surface. The flow behavior of the granular material in such an avalanche is strongly non-Newtonian (Kakalios, 2004), such that only a narrow region directly below the free surface is affected by avalanching. The angle of repose, θ_r, for a dry sandpile depends on the density and size of the grains, the coefficient of sliding and rolling friction and the surface roughness and shape (Kakalios, 2004). Avalanching of granular material may occur for angles:

$$\theta_r < \theta < \theta_m, \tag{1.1}$$

depending on stability and disturbances (Tischer *et al.*, 2001). Tischer *et al.* (2001) found for well sorted playground sand with $D_p = 0.3 - 0.5$ mm and $\rho = 2.6 - 2.8$ kg/m^3 an angle of repose $\theta_r \approx 31°$ and a maximum angle of angle of stability $\theta_m \approx 34°$. Only in a cohesionless material is the angle of repose θ_r equal to the internal angle of friction ϕ relating the shear

and normal stress: $\tau = tan(\phi)\sigma$.

The deposition of windblown sand may occur due to tractional or gravitational processes ((Greeley and Iversen, 1985), figure 1.2). Tractional deposition occurs when the sand comes to rest in a sheltered position, for example in a wind ripple on a climbing surface or on flat planes. Hunter (1977) recognized four different types of strata resulting from tractional deposition: planebed laminae, rippleform laminae, ripple-foreset crosslaminae and climbing translatent strata. Gravitation-driven deposition mechanisms lead to strata due to grainfall and grainflow. Grainfall occurs in zones on the leeward face where the flow separates from the surface, decelerates and comes to rest without forward motion. Grainflow involves the avalanching of noncohesive sand on slipfaces where the dune slope exceeds the angle of repose θ_r.

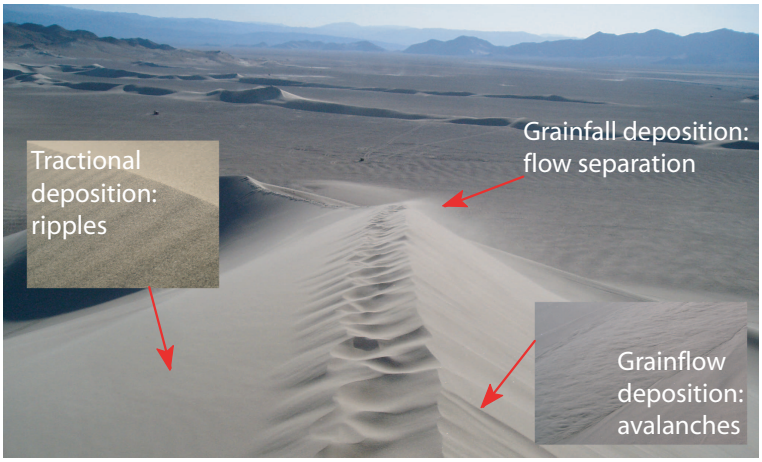

Figure 1.2: Deposition types on a sand dunes: tractional, grainfall and grainflow deposition.

The internal structure of dunes is a result from the different deposition processes and feature cross-strata enclosed by bounding surfaces. Cross-strata are layers or "sets" that are inclined with respect to the desert floor. Kocurek (1996) defines bounding surfaces as "*erosional surfaces within or between sets of cross-strata*" and subdivides them in interdune surfaces (including the desert floor and the free surface), superposition surfaces (on main structure due to the reversing of the dune), reactivation surfaces (within a set after the return to the normal wind regime) and super surfaces (between the parts of superimposed dunes). The unique stratification types found in sand deposits due to wind-ripple laminae, grainflow cross-strata and grainfall strata record the flow configurations (Kocurek, 1991)

and provide clues on the type of dune under investigation.

Types of dunes

Dune type depends on wind strength, sand supply and amount of vegetation. McKee (1977) defined several morphological dune types based on shape as opposed to Hunter *et al.* (1983), who adapted a classification scheme of morphodynamical dunes based on crestline orientation to the long-term wind direction. In the morphological system dune types are differentiated by the shape of the dune and crest:

- Crescentic or barchan dunes: fast moving, slipface is on the dune's concave side.
- Linear dunes: straight or slightly sinuous sand ridges; very long, parallel ridges separated by corridors.
- Star dunes: radially symmetrical with several arms and slipfaces; pyramidal sand mounds.
- Dome dunes: oval or circular mounds lacking a slipface, occur in the far upwind margins of sand seas.
- Parabolic dunes: U-shaped with arms pointing downwind and crest pointing upwind; trailing arms are covered in vegetation.

"Compound dunes" have several dunes of the same type superimposed on each other and "complex dunes" feature different basic dune types combined into one dune. The morphodynamical system analyzes the orientation of the dune crestline with respect to the long-term wind vector:

- Transverse dunes: crests oriented within -75° to -90° and 75° to 90° (perpendicular) to the prevailing wind direction.
- Longitudinal (or seif) dunes: crests oriented within -15° to 15° (parallel) to the prevailing wind direction.
- Oblique dunes: crests oriented within -15° to -75° and 15° to 75° (oblique) to the prevailing wind direction.

Crescentic dunes may appear in transverse and oblique wind regimes, while linear dunes appear for oblique or longitudinal wind direction. Star dunes are the most diverse as their arms are observed to be of all three morphodynamical types and face all wind directions (Kocurek, 1991).

1.1.3 Sand

Aeolian processes may shape a variety of smaller material into larger structures. Longitudinal stationary snow (H_2O) dunes in the Arctic and Antarctic may only be a few meters high, but they are up to hunderds of kilometers long and are separated by 1-2 kilometers (Tomlin, 1999). Volcanic ash forms dunes from razor-sharp glass particles deposited by pyroclastic flows at for example Tenerife and in Hawai'i Volcanoes National Park. Backbeach or coastal dunes are often composed of shattered seashells resulting in a calcium carbonate ($CaCO_3$) material. Gypsum dunes, such as the dunes in the White Sands National Monument, are composed of gypsum ($CaSO_4 \cdot 2H_2O$) crystals that remain behind in dry lakebed deposits. The most common "sand dunes" known are the dunes composed of quartz (SiO_2) and feldspar (potassium $KAlSi_3O_8$, sodium $NaAlSi_3O_8$ or calcium $CaAl_2Si_2O_8$) particles found, for example, in the large Saharan desert. The erosion of granitic mountains creates small particles of silica that form the large dune expanses.

All these dunes are sand dunes, even when the composition of the building material is exotic. Sand actually refers to the particle size instead of the chemical composition. Rocks are broken down into smaller-sized particles by physical, chemical or biological processes; the so-called weathering of minerals that creates a distribution of particle sizes.

Size and sorting of sand

Sand ranges from very fine to very coarse and has diameters between $D = 0.0625$ mm and $D = 2$ mm (Wentworth, 1922). The combination of different sizes in a dune sand sample forms a particle-size distribution that may be quantified by a sieve analysis. The cumulative frequency distribution is represented by plotting the "percent by weight finer" versus "grain size." The arithmetical probability method gives a characteristic S-shape, while the logarithmic probability representation produces a straight line. Figure 1.3 shows the logarithmic probability representation covering size fractions of a surface sample from the crest of a sand dune.

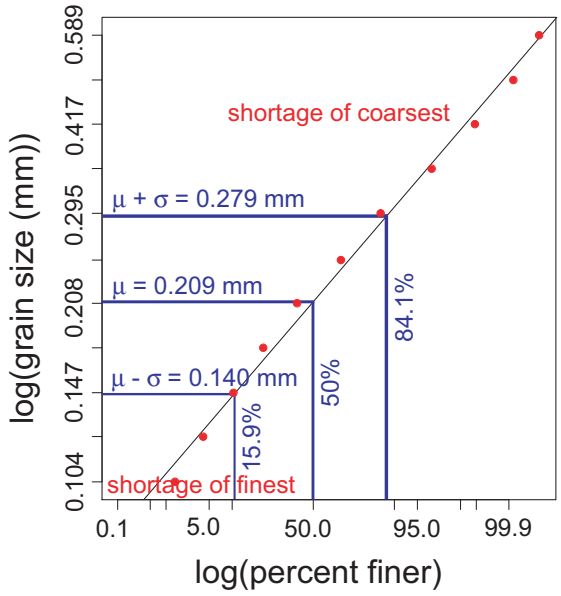

Figure 1.3: Size distribution of a surface sand sample from the crest of a dune at the Dumont dunes field in California, USA.

As a first approximation the distribution follows a straight line implying a log-normal distribution, but has deviations at the extreme ends of the spectrum. The deviations at the extreme ends of the distribution are due to the absence of the finest and coarsest sediments in the sample. The finest fraction is removed from the aeolian landscape as dust and coarse sediments are not transported by the wind. The graphical technique of drawing a straight line and assuming a log-normal distribution provides an average diameter and standard deviation of the sample, but does not include higher moments of the distribution. The log hyperbolic and log skew Laplace distribution may be better suited (Flenley *et al.*, 1987) for sediments as it includes the higher moments.

Folk and Ward (1957) developed four statistical parameters that describe the higher moments of frequency distribution of sieved samples. The central mean, μ, provides a measurement of the average particle diameter. The degree of sorting or standard deviation, σ, indicates the relative percentages of grain size fractions. Poorly sorted, or well graded, sand has a wide range of grain sizes and therefore a large standard deviation. The sorting of sand is directly dependent upon the uniformity and persistence of deposition with time. Higher moments of frequency distribution include the lopsidedness or skewness, γ, and the degree of peakedness or kurtosis, κ. Appendix A.2 includes additional information on the

statistical measurements of a granular material.

Shape of sand

Grain characteristics include angularity and sphericity. In some respects, these characteristics are counterintuitive, because a particle may be very round, but not spherical. The degree of angularity (roundness) reflects the duration of abrasion in the transport of sediments. In aeolian transport, sand undergoes high-energy collisions and abrasions such that the surface is frosted, not smooth and sharp edges and corners break off. Roundness may be hard to quantify objectively and is based on visual estimations of the convex versus the concave edges. Six classes of particle roundness are commonly presented; very angular, angular, sub-angular, sub-rounded, rounded and well rounded (appendix A.2).

The sphericity gives an indication of the history of the sedimentary environment and represents the variation of size in different directions. The longest, shortest and, by assuming orthogonality, the intermediate axis of the ellipse around a grain provide ratios of length. The resulting shape of the particle may vary from equidimensional to disk shaped and from rod shaped to elongated (appendix A.2).

1.2 Acoustic Emissions from a Granular Material

A granular material such as sand forms a distinct and fascinating phase in physics–imagine taking some sand in your hand on a beach. Sand can act like a fluid with viscosity if you pour the grains through your fingers. The falling sand grains form a heap with rigidity, a characteristic of a solid. On a very windy day, sand is temporarily suspended in the air like a gas and can travel long distances. The macroscopic properties of a granular material are clearly defined by its bulk properties such as density, sound speed, rigidity and concentration. From the microscopic perspective, however, the force chains are the "highways" along which individual grains distribute their forces and interact with each other (Jaeger *et al.*, 1996). This duality in scales between the particle-particle interactions and the general flow behavior characterize a granular flow.

Macroscopic process such as forced compression, forced shearing or natural slumping of a granular bed may generate acoustic activity in both nature and industrial application. The general consensus is that acoustic emission from sand occurs if the sand grains have a

very smooth and polished surface texture (Lindsay *et al.*, 1976), while grain shape, sorting, roundedness and sphericity play a lesser role (Sholtz *et al.*, 1997).

1.2.1 Sound from Forced Compression

Singing beaches emit sounds when walked upon. These acoustical seashore locations have been found on a variety of beaches including Japan (Kotobikihama beach, (Miwa and Okazaki, 1995)), Great Britain (the Isle of Eigg, (Ridgway and Scotton, 1973)), Canada (Basin Head, Prince Edward Island) and the United States (Barking sands of Kaua'i, Hawai, (Bolton, 1889)). The sand is displaced quickly underfoot and emits a high frequency squeak or whistle of short duration. Reports (Miwa *et al.*, 1995) note that whistling beaches have drastically been reduced in recent years due to sea water pollution. Takahara (1973) measured a harmonic signal with a frequency of 525 Hz by walking over the beach and concluded that the acoustic emission depends on the friction properties of particles of uniform size and smooth surface. Ridgway and Scotton (1973) performed a statistical analysis on sand from 33 whistling sand beaches of the British Isles. The sand was classified as good, medium or poor whistlers by hand scuffing the surface. The authors analyzed the particle size distribution by sieving and the particle shape with a vibratory shape-sorting table. They concluded that a narrow size distribution and spherical grain shapes are required to produce the whistling. The whistling properties are destroyed by abrasion producing fine particles and are restored by rain or tide removing the fine particles. The location of whistling sand correlates with the landward end of bed-load partings–locations in the sea bed where sand transportation originates.

Haff (1979) performed a series of experimental studies on sand from seven different dunes, two beaches and sand next to a road to investigate sound resulting from forced compression. The "*compression test*" in the laboratory investigated the high pitched squeaking sound generated by compressing sand with a pestle at velocities of $V_p \approx 1$ m/s. All dunes sands and the roadsand had at least one active size fraction (usually D = 0.104-0.175 mm or D = 0.175-0.246 mm) while the beach sands emitted no sound under any circumstance. The Kelso dune sand sample ($D = 0.211 \pm 0.069$ mm) produced a squeak of $f_{sq} = 1224$ Hz, while the Saline valley sample (D = 0.230 ± 0.149 mm) had a major peak at $f_{sq} = 964$ Hz. From the compression test Haff deduced that "*it seems likely that the differences in velocity are responsible for the change of frequency, with a change in mass (or area) merely affecting*

the efficiency of the coupling of the sand vibration to the air vibration." Hidaka *et al.* (1988) investigated sound generated by compressing sand grains by a pestle with x-ray photography. The shearing creates discrete slip bands due to the frictional properties of the sand. The width of the shear band δh depends on the diameter of the pestle and the static and dynamic friction angles. The frequency of the whistling,

$$f_{sq} = N\frac{V_p}{\delta h}, \tag{1.2}$$

is a direct function of the penetration speed of the pestle V_p, the width of the shear band δh and the total number of shear bands $N = 1, 2...$ The author measured squeaking frequencies from $f_{sq} = 250$ to 355 Hz depending on the penetration speed V_p. Miwa *et al.* (1995) also excited whistling sand with a pestle in a glass pot in the laboratory and recorded frequencies varying from 340 to 700 Hz with at least one overtone. Patitsas (2003) reiterated the earlier approach and proposed a fluid mechanical theory based on the existence of slip channels. The finite width of these channels and the number of sand layers slipping over each other would correspond to a specific frequency, similar to the mechanism proposed by Hidaka *et al.* (1988). In a follow-up paper, Patitsas (2008) posed that "*the frequencies of the vibrations, generated by the pestle-grain interaction, cannot be specified in terms of propagating waves, but rather in terms of standing wave patterns, or standing modes of vibration.*" He measured squeaking frequencies between $f_{sq} = 235$ and 750 Hz depending on the degree of compaction. He argued that the excitation frequency described by equation (1.2) needs to be provided by an outside source, the pestle, but that "*the spread in the frequency content [...] cannot be due to changes in the velocity of descent of the pestle, and therefore cannot be due to a propagating wave, but rather due to standing wave patterns,*" even with an estimated shear wave velocity $\beta \approx 5$ m/s instead of a pestle velocity V_p. A standing wave pattern appears between the pestle and the bottom and produce a transcedental equation expressing the excitation frequency in terms of the shear β and compressional α wave speed, the mass and dimensions of the pestle, the dimension of the shear bands and the wave number of the shear wave.

1.2.2 Sound from Forced Shearing

Granular flow-induced vibration due to shear occurs in a variety of industrial applications. Dr. Paul Mort from Proctor and Gamble, in a personal communication, noted that polymer beads used in the production of diapers produce a squeaking sound when sheared. Polystyrene beads at mesh size 70 (D = 0.210 mm) from Supelco produce high-pitched sound when shaken back and forth in a container. The phenomenon of silo honking occurs when a cylindrical silo filled with a confined granular material discharges. The silo emits a loud (up to 100-110 dB) "*honk*" similar to a truck horn (Buick *et al.*, 2005) and has a dominant frequency of several hunderd Hertz with higher harmonics. The silo needs to be filled up beyond a certain fill height to get honking, but neither the fill height nor the discharge rate influences the frequency directly. Honking silos can cause large problems in the bulk handling industry–large vibrations influence the strength and integrity of the holding system while the sound could cause problems with noise protection regulations.

Muite *et al.* (2004) investigated the vibrations of the "*silo quake*" with an unidirectional shear accelerometer on the silo and in the granular material and measured the noise of the "*silo music*" with microphones. The accelerations in the granular material are synchronized with the accelerations of the silo wall but are much larger in magnitude. The authors show that the silo music is due to stick-slip friction between the granular material and the silo walls and that the sound resonance occurs in the air column above the bed. The sound represents odd harmonics (n = 1, 3, 5...) of the fundamental resonance frequency with the node on the granular surface and the antinode at the open end of the silo. Muite *et al.* (2004) showed that the pulsation frequency of the silo music may differ from the dominant natural frequency of the silo structure and indicate that the silo quake is not due to resonance between the granular material and the silo wall. In a study performed at the same time, Buick *et al.* (2005) investigated silo music with triaxial accelerometer measurements on the silo wall and microphone measurements of the acoustic pressure. The authors notice a fundamental acoustic frequency at f_{si} = 333 Hz with a harmonic series of integer multiples (n = 1,2,3...) of the fundamental frequency. The frequency structure of the wall vibration is equal to the honking sound. The authors propose that the sound is not generated by resonance inside the silo but by horizontal oscillations of the silo wall acting as a large loudspeaker. The frequency does not change with varying fill height and therefore the air layer or column of

pellets do not generate a resonant frequency.

Shearing of sand may also create an emission at certain dunes and in the laboratory. Lewis (1936) noticed that "*pushing the sands forward in a heaped-up manner*" at Witsands, Kalahari in South Africa creates an irregular roar. Criswell *et al.* (1975) generated "*short-duration (< 2 s) forced seismic and acoustic emissions*" (f_{bp} = 69 Hz with a 137 Hz overtone) by "*extended digging*" with a flat-bladed shovel. Lewis (1936) noticed that roaring disappeared quickly due to humidity and was restored by heating the sample in an oven. The author also made the observation that laboratory roaring could be produced from natural sands from other, silent, dunes and from common salt (D = 0.206 ± 0.168 mm). Haff (1979) placed sand in a container in the "*beaker test.*" Shaking sand from Kelso and Eureka dunes, USA back and forth resulted in an emission at a lower frequency ("*several hundred Hertz*") than his compression test. The role of pressure and interstitial air in the generation of this acoustic emission has been eliminated in Haff (1979) based on experiments of sand in a evacuated steel chamber; the vibrations of the sheared sand were observed despite the presence of a vacuum. Williams (2004) attributed this "*burping*" sound to the interaction of shear layers moving as solid bodies passed each other. Douady *et al.* (2006) constructed a laboratory experiment where a blade rotates in a channel of singing sand. The authors control the shearing velocity and mass of sheared sand during the rotation. The experiment shows that the mean shear determines the frequency (25-250 Hz) and that neither the velocity, nor the mass influences the sound frequency.

1.2.3 Sound from Natural Slumping

A granular material may start to slump naturally under the influence of gravity when the slope exceeds the angle of repose as defined in equation (1.1). Thermal moonquakes are slumping events on the edges of craters on the moon that create significant microseismicity (Criswell and Lindsay, 1974) and only limited erosion. These moonquakes are the lunar equivalents of the terrestrial avalanche events leading to the phenomenon of "booming sand dunes." For centuries booming sand dunes have intrigued travelers and scientists alike. These dunes emit a persistent, low-frequency sound during a slumping event or natural avalanche on the leeward face of the dune. This sound can last for several minutes and be audible for miles. The acoustic emission is characterized by a dominant audible frequency (f = 70-105 Hz) and several higher harmonics.

1.2.4 Booming Dune Locations

In 1923, the Marquess Curzon of Kedleston published Tales of Travel (Curzon of Kedleston, 1923) documenting his own and other reports of booming dunes from earlier world travelers. Other explorers or researchers confirmed and expanded on the known locations documented by Curzon of Kedleston (1923) and Lindsay *et al.* (1976) provided an extensive summary of booming locations. Carus-Wilson wrote in an 1890 letter to Nature (Carus-Wilson, 1890): "*only observers are rare–not the sands,*" and nowadays up to 40 locations with booming sand dunes are identified in table 1.1. "Google Earth" aided in the identification of the latitude and longitude coordinates of different booming dunes to enable booming dune chasing with a personal handheld GPS device. The dune type are based on the morphological system and the size of the dune or dune field and the elevation loss across the top of the highest dune and the desert floor are enabling the creation of scale.

Table 1.1: Collection of the known booming sand dunes in the world, subdivided into the regions "Asia," "Middle-Eastern peninsula," "Africa," and "North and South America".

Name and location booming dunes [1]	**Latitude, longitude** [2]	**Type: size field, elevation loss** [3]	**Source** [4] [5]
Asia			
Ming Sha San, near Dunhuang, Gansu Province, China	40° 05′ 00″ N, 94° 40′ 29″ E	Star dune field: 20 × 20 km, 300 m drop	A, B, K, internet
Golden Bell of Resonant Sand, near Shapotou, Ningxia Province, China	37° 28′ 10″ N, 105° 01′ 23″ E	Isolated dune: 0.5 × 0.5 km, 100 m drop	internet
continued on next page –			

[1] Certain locations previously mentioned in other overviews have been omitted (table 1.2).

[2] Latitudes and longitudes with degrees and minutes indicate a general area, while locations with degrees, minutes and seconds pinpoint to the highest crest of a given booming dune.

[3] The elevation loss is calculated from the highest peak in the dune system to the desert floor.

– continued from previous page

Name and location booming dunes [1]	**Latitude, Longitude** [2]	**Type: size field, elevation loss** [3]	**Source** [4] [5]
Xiangshawan (Resonant Sand Gorge), near Baotou, Inner Mongolia, China	40° 14′ 39″ N, 109° 56′ 23″ E	Sand drift: 500 m wide, 50 m drop	internet
Southeast edge of the Badain-Jaran desert, China	39° 37′ N, 102° 29′ E	Extended megadune field: 50 × 50 km, up to 200 m drop	G
Echoing Sand dune of Hami, near Balikun, Xinjiang Province, China	43° 24′ 59″ N, 93° 42′ 06″ E	Linear ridge in a dune field: 3 × 5 km, 100 m drop	internet
Ming Sha near Mori, Xinjiang Province, China	44° 36′ 17″ N, 91° 38′ 19″ E	Star dune field: 5 × 10 km, 80 m drop	G
Jeminay sand desert, Xinjiang Mongolia, China	47° 47′ N, 86° 23′ E	Barchan dune field: 3 × 1 km, 100 m drop	G
Khongor sand dune, near Khongoryn Els, Mongolia	43° 49′ 13″ N, 102° 07′ 24″ E	Star dune field: 25 × 5 km, 200 m drop	internet
Akkum-Kalkan, Altyn-Emel national park, Kazakhstan	43° 51′ 43″ N, 78° 34′ 12″ E	Barchan dune field: 3 × 1 km, 100 m drop	A, internet
Reg-I-Ruwan, near Kabul, Afghanistan	35° 03′ 47″ N, 69° 22′ 07″ E	Mountain with sand drift: 100 m wide, 100 m drop	A
Rig-I-Riwan, near the Kalah-I-Kah mountain range, Afghanistan	32° 11′ 20″ N, 61° 20′ 54″ E	Mountain with sand drift: 600 m wide, 200 m drop	A, R
Middle-eastern peninsula			
Singing dunes, near Umm Said, Qatar	25° 02′ 19″ N, 51° 24′ 25″ E	Barchan dune field: 15 × 30 km, 20 m drop	B, internet

continued on next page –

– continued from previous page

Name and location booming dunes [1]	**Latitude, Longitude** [2]	**Type: size field, elevation loss** [3]	**Source** [4] [5]
Dunes south of the Liwa Oasis, Rub' Al Khali desert, United Arab Emirates	23° 08′ N, 53° 46′ E	Complex dune field: 1200 × 650 km, up to 120 m drop	U, internet
Sharqiya (Wahiba) sands, near Al Ashharah, Oman	22° 21′ N, 58° 49′ E	Linear dune field: 70 × 100 km, up to 70 m drop	internet
Sand of Yadila, Uruq Adh Dhahiya region, Oman	18° 47′ N, 52° 15′ E	Extended complex dune field: 300 × 150 km, up to 100 m drop	M
Uruq Subay (Arq-al-Subai), Saudi Arabia	22° 14′ N, 43° 04′ E	Linear dune field: 30 × 80 km, up to 100 m drop	A
Sand near Khanug, Saudi Arabia	24° 22′ 33″ N, 43° 42′ 33″ E	Mountain with sand drift: 100 m wide, 60 m drop	A
Jabal-al-Thabul (Mount of Drums), near Badr, Saudi Arabia	23° 48′ 25″ N, 38° 45′ 57″ E	Star dune field: 1.5 × 6 km, 180 m drop	A, W
El-Howayia, near Madain Saleh, Saudi Arabia	26° 46′ N, 37° 51′ E	Mountain with sand drift: 100 m wide, 60 m drop	A, L, X
Goz Et-Hannan (Moaning sand heap), near Wadi Ratiyah, Saudi Arabia	28° 04′ 27″ N, 35° 25′ 45″ E	Sand drift shaped as a pyramid: 0.3 × 0.4 km, 15 m drop	A, S
Africa			
Jebel Nakus, near Tor, Egypt	28° 21′ 14″ N, 33° 30′ 57″ E	Mountain with sand drift: 500 m wide, 70 m drop	A
Umm Shumar, Sinai Desert, Egypt	28° 17′ 28″ N, 33° 51′ 03″ E	Mountain with sand drift: 400 m wide, 50 m drop	A

continued on next page –

– continued from previous page

Name and location booming dunes [1]	**Latitude, Longitude** [2]	**Type: size field, elevation loss** [3]	**Source** [4 5]
Dunes near the Dakhla Oasis, Egypt	25° 12′ 42″ N, 28° 47′ 03″ E	Barchan dune field in two belts: 5 km × 0.4 km, 15 m drop	A, N
Gilf Kebir desert, near the Nubian Sandstone platform, Egypt	23° N, 26° 30′ E (C), 26° 30′ N, 27° 10′ E (O)	Linear dune field: 350 × 250 km, up to 50 m drop	C, O
Gege Kourini, near the Korizo pass, Chad	22° 33′ 08″ N, 15° 23′ 37″ E	Linear dune in barchan dune field: 1.2 km long, 90 m drop	I
Elb Ben Abbas, Igidi desert, Algeria	26° 05′ 10″ N, 6° 17′ 46″ W	Linear dune field: 300 × 30 km long, 50 m drop	A, P
Ghourd el Hamra, near Tarfaya, Morocco	28° 01′ 29″ N, 12° 10′ 40″ W	Barchan dune: 0.5 × 0.5 km long, 25 m drop	E, F
Dunes near Azoueiga, Erg Amatlich, Mauritania	19° 52′ N, 13° 33′ W	Large sand sea: 75 × 10 km	internet
Dunes near Shingati, Mauritania	20° 27′ N, 12° 22′ W	Large sand sea: 40 × 15 km	internet
Skeleton Coast park, Namibia	19° 07′ S, 12° 36′ E	Large sand sea: 120 × 20 km	internet
Sossusvlei, Namib-Naukluft park, Namibia	24° 40′ 19″ S, 15° 31′ 13″ E	Star dune field in a linear desert: 275 × 100 km, 340 m drop	A
Witsands, Kalahari desert, South Africa	28° 34′ 31″ S, 22° 27′ 39″ E	Star dune field: 5.5 × 1.5 km, 40 m drop	H

continued on next page –

– continued from previous page

Name and location booming dunes [1]	**Latitude, Longitude** [2]	**Type: size field, elevation loss** [3]	**Source** [4] [5]
North and South America			
Great Sand Dunes National Park, Colorado, USA	37° 44′ 54″ N, 105° 31′ 59″ E	Star dune field: 12 × 9 km, 200 m drop	D
Sand Mountain, Nevada, California, USA	39° 18′ 59″ N, 118° 23′ 59″ W	Linear ridge: 1 × 2.5 km, 110 m drop	B, T, AA
Crescent dunes, Nevada, California, USA	38° 13′ 47″ N, 117° 19′ 45″ W	Star dune field: 3 × 1.5 km, 70 m drop	AA
Eureka dunes, Death Valley National Park, California, USA	37° 06′ 04″ N, 117° 40′ 16″ W	Linear ridge with star dunes superimposed: 1.5 × 5 km, 200 m drop	D, Y
Panamint dunes, Death Valley National Park, California, USA	36° 27′ 38″ N, 117° 27′ 21″ W	Star dune: 1 × 1 km, 70 m drop	Y, Z, AA
Big dune, Nevada, USA	36° 38′ 52″ N, 116° 34′ 48″ W	Star dune field: 1.5 × 2.5 km, 80 m drop	D, Y, AA
Dumont dunes, Mojave desert, California, USA	35° 40′ 43″ N, 116° 13′ 54″ W	Star dune field: 2 × 4 km, 120 m drop	D
Kelso dunes, Mojave National Preserve, California, USA	34° 53′ 54″ N, 115° 44′ 00″ W	Linear ridge with star dunes superimposed: 4 × 8 km, 150 m drop	B, D, Y
Cerro Unitas (El Bramador [6]) in the Tarapaca desert, Chile	19° 57′ 04″ S, 69° 37′ 58″ W	Mountain with sand drift: 100 m wide, 15 m drop	A, B, Q
El Medanoso, Mar de Dunas, Chile	27° 07′ 11″ S, 70° 07′ 56″ W	Star dune field: 4 × 6 km, 450 m drop	E, internet
El Punto de Diabolo (El Bramador), near Copiapo, Chile	27° 18′ 58″ S, 70° 25′ 06″ W	Mountain with sand drift: 100 m wide, 70 m drop	A, B, E

continued on next page –

– continued from previous page

Name and location booming dunes [1]	**Latitude, Longitude** [2]	**Type: size field, elevation loss** [3]	**Source** [4] [5]

Earlier descriptions and overviews included several locations summarized in table 1.2 that are omitted in table 1.1 for various reasons.

Table 1.2: Omitted locations of booming sand dunes in the world.

Name and location omitted dunes [1]	**Latitude, longitude** [2]	**Reason for omission** [7]	**Source** [4] [5]
Wadi Hamadi dunes, Saudi Arabia	north of Medina	Unable to trace exact location	A
Dunes near the dead city of Jahura, Saudi Arabia	near 22° N, 51° E	Unable to trace exact location	A
Dunes in the An Nafud desert near El-Hyza, Saudi Arabia	north of 27° 31′ N, 41° 42′ E	Unable to trace exact location	A, L
Ojrat Ramadan, Wadi Werdan, Egypt	near 29° 30′ N, 32° 43′ E	Unable to trace exact location	A

continued on next page –

[4]Several references to booming dunes have been found on the internet (i.e., on travel webpages) without a proper scientific reference.

[5]The sources are: A: Curzon of Kedleston (1923), B: Lindsay *et al.* (1976), C: Bagnold (1941), D: Vriend *et al.* (2007), E: Douady *et al.* (2006), F: Andreotti (2004), G: Miwa and Okazaki (1995), H: Lewis (1936), I: Humphries (1966), J: Bolton (1889), K: Polo (1295), L: Doughty (1888), M: Thomas (1932), N: Harding King (1912), O: Shaw (1936), P: Lenz (1912), Q: Bollaert (1851), R: Yate (1897), S: Burton (1879), T: Holliday (1976), U: Hagey and Hope (2008), V: Clark (1990), W: Peters (1996), X: Hoye (1965), Y: Haff (1979), Z: personal communication with E. C. Koos, AA: Trexler and Melhorn (1986).

[6]Bollaert (1851) described that the Cerrito de Huara is situated 6 miles WNW from Pozo de Ramirez on the road from Tarapaca to Guantajaya in a desert plain. The Cerro Guara (20° 02′ 13″ S, 69° 46′ 32″ W) is actually 4 miles WNW from Pozo de Ramirez, but is completely devoid of sand and borders a mountain chain. The Cerro Unita is situated 8.5 miles NNE from Pozo de Ramirez, is a lone hill in the desert plain and has sand gullies. It is possible that Bollaert misplaced the "Bramador."

[7]Some locations referenced once in older travel literature cannot be located, disappeared or are back beach dunes where only short "barking" sound can be generated.

– continued from previous page

Name and location omitted dunes [1]	**Latitude, longitude** [2]	**Reason for omission** [7]	**Source** [4 5]
Mountain of the Bell, Baja California, Mexico	near 24° 03′ N, 110° 59′ W	Back beach dune: barking sounds	B, J
Ke one kani o (the sounding sands), Kaua'i, Hawaii, USA	22° 03′ 53″ N, 159° 46′ 56″ W	Back beach dune: barking sounds	A, B, J, V
Ke one kani o (the sounding sands), Ni'ihau, Hawaii, USA	21° 56′ 09″ N, 160° 09′ 26″ W	Back beach dune: barking sounds	A, J, V

Descriptive references to the booming phenomenon are found in folklore and historical literature. A mystical description was written by the Chinese writer Tun Huang Lu (Giles, 1915) around 800 A.D.: "*The Hill of Sounding Sand [...] is made up entirely of pure sand. This hill has strange supernatural qualities. Its peaks taper up to a point, and between them there is a mysterious hole which the sand has not been able to cover up. In the height of summer the sand gives out sounds of itself, and if trodden by men or horses the noise is heard many tens of li (1 li = 0.5 km) away. It is customary on the tuan-wu day (the Dragon festival on the fifth of the fifth moon) for men and women from the city to clamber up to some of the highest points and rush down again in a body, which causes the sand to give forth a loud rumbling sound like thunder. Yet when you come to look at it the next morning the hill is found to be just as steep as before. The ancients called this hill the Sounding Sand; they defied the sand and worshipped it there.*" Around the same time, the Chinese historiographer Ma Tuan-lin (Polo, 1295) described the sounds in his encyclopedia. "*During the passage of this wilderness you hear sounds, sometimes of singing, sometimes of wailing; and it has often happened that travelers going aside to see what these sounds might be have strayed from their course and been entirely lost; for they were voices of spirits and goblins.*" In the thirteenth century, Venetian explorer Marco Polo (Polo, 1295) described a "*strange thing*" occurring in the Gobi desert: "*The desert spirits can do amazing and incredible things. Even in the daytime their voices can sometimes be heard, or there is a clash of arms, a roll*

of drums or the sound of different musical instruments. For these reasons, travelers go in large numbers and stay close to one another." The Ming Sha Shan dunes near Dunhuang, China that Marco Polo passed were created according to local legend by a gust of wind forming the sand dune and burying warriors fighting in a fierce battle. As the battle was at its height, the roaring soldiers continue to fight beneath the sand.

Similar legends and mystical explanations exist for other booming dunes in the world. A visitor disregarded a sacred oath he made to the monks with regards to the location of the monastery at the Jebel Nakus, near Tor, Egypt (Curzon of Kedleston, 1923). After his return he identified the mountain, "*but the monastery, gardens, and monks had all disappeared, and nothing remained to show that they had ever existed save the sound of the nagus calling them to prayers within their mysterious retreat in the very heart of the mountain.*" Local culture and history are sometimes interwoven with the natural environment: near Badr, Saudi Arabia is "*the Mount of the Drums, which looks like an elongated sand dune, and it is so called because of a widely held tradition that there is heard there every Friday the sound of drums as a perpetual reminder of the Prophet's victory there*" (Peters, 1996). Local animals are also a favorite subject to explain the supernatural sounds. Hoye (1965) describes the account of a local Bedouin of the El-Howayia valley, near Madain Saleh, Saudi Arabia: "*On certain moonlit nights, when the cool winds blow across the sand,*" he said, "*the Bedouins of the valley have heard a strange sound in the distance, from high up and far away. The sound, they say, is of a frightened baby camel crying for its mother.*" Holliday (1976) describes the local story in Nevada, California, USA that "*a large sea dinosaur or plesiosaur once lived and frolicked with its mate in ancient Lake Lahontan. Strong winds piled the lakebed sediments into what is now called Sand Mountain, completely burying the dinosaur under hundreds of feet of sand. Today the dinosaur moans for its mate and the deep blue waters of Lake Lahontan.*"

These stories, references and explanations are mystical and not based on scientific facts, but they illustrate that the phenomenon of booming sand dunes occurs on sand dunes across the globe. Booming has been reported on latitudes on both the northern (47° N and 19° N) and southern the hemisphere (19° S and 29° S) covering desert climates in the subtropics (BWh) and the mid-latitudes (BWk). Another important observation from data in table 1.1 is that booming occurs on a variety of different morphological dune types with elevation losses of 20 meters or more. Star dunes are the most common dune type for booming, but

booming has also been found on smaller barchans, on long linear dunes and on mountains with extended sand drifts.

In this world without boundaries there are many sandy deserts that have been visited by travelers and scientists. These deserts have dunes covering a variety of types with large slip faces, but still booming is rarely observed and scarcely recognized. The central question remains why do not all dunes boom?

1.3 Previous Scientific Work

Scientists started to explore possible causes of the sound generation by the end of the 19th century. Carus-Wilson (1888) provided a first scientific explanation and attributed the sound to friction between grains. Bolton and Julien (1888) rejected this explanation and proposed the generation of sound in terms of an air film acting as a cushion capable of vibration. Poynting and Thompson (1909) stated that the bed of sand will have a minimum volume, such that the frequency is inversely proportional to the time required to pass between minimum volumes. This approach indicates that sound is produced by the relative motion between grains and that the frequency f scales with the shear velocity U and the characteristic length scale D, the particle diameter, as $f \approx \frac{U}{D}$.

In the middle of the 20th century estimations of the booming frequency and measurements of sand samples provided more information on quantifiable properties. Lewis (1936) measured the grain size characteristics of acoustic sand at Witsands in the Kalahari desert, South Africa. He noted that the acoustic sand has a narrower size distribution (D = 0.226 $\pm$ 0.069 mm) than the silent sand from all Kalahari dunes (D = 0.177 $\pm$ 0.120 mm). He also noted that the acoustic sands are characterized by a purely quartz, less angular, more rounded and well sorted sand. Lewis noticed a distinct difference between the short-duration roar (burp due to forced shearing) and sustained hum (boom due to natural slumping) as he mentioned "*the roar is caused by pushing the sands forward in a heaped-up manner and the hum is obtained by keeping the sand moving down the slope in slow motion*". He used pitch pipes to estimate the constant frequency of the hum (~264 Hz) and the frequency of the roar that increased with shearing velocity from ~132 Hz to a "*swish*". Humphries (1966) did not visit the Gege Kourini dunes near the Korizo pass, Chad himself but depended on accounts of collaborators that reported that the sound was between f = 50 and 100 Hz with

a beating frequency of approximately $f_{bt} = 1$ Hz. Humphries analyzed the sand samples in the laboratory ($D = 0.26 \pm 0.066$ mm) and discussed that "the enormous volume of sound produced suggests that in some way a natural resonator must be involved in magnifying the sound". He continued by implying that "*the stationary sand beneath may act as a sounding board*". Bagnold (1941) visited booming dunes in the Gilf Kebir desert between Libya and Egypt and he: "*put the note heard as somewhere around 132 cycles/sec, and [...] the mean size of the grains was larger, being about 0.35 mm.*" In a later paper Bagnold (1966) developed a theory of the sound generation based on the shearing and dilatation of grains in a slip plane and derived a relation between the booming frequency f and the particle diameter D.

In the course of the 20th century, the development of digital equipment enabled researchers to measure the frequency of the burp/roar and the boom/hum precisely by using post processing. Criswell *et al.* (1975) and Lindsay *et al.* (1976) performed field experiments with forced shearing on Sand Mountain, Nevada, but did not publish frequencies for sustained slumping. Haff conducted field experiments involving in situ sustained booming at Kelso dunes ($D = 0.211 \pm 0.069$ mm), Big dune ($D = 0.265 \pm 0.090$ mm) and Eureka dunes ($D = 0.222 \pm 0.046$ mm) and published in Haff (1979) that the booming frequency at Kelso dunes increased from $f = 92.8$ Hz to $f = 96.8$ Hz within a few seconds during the slide. From these results he derived that there is "*no common feature of the grain size distribution which is critical for in situ booming.*" Haff concluded "*that the occurrence of booming in a particular dune field or other sand formation depends upon the simultaneous presence of a number of environmental factors.*" Nori *et al.* (1997) and Sholtz *et al.* (1997) published overview articles on booming sands but did not conduct new field measurements on booming. Sholtz *et al.* commented on the large amplitude of oscillation involved with the grains in the shear plane and concluded that "*any realistic model of booming must be based on nonlinear pressure vibrations.*" (Criswell *et al.*, 1975), Nori *et al.* (1997) and Sholtz *et al.* (1997) all questioned the scaling based on particle diameter because of the large variation in average diameter of the sand grains and the inconsistency of the predictions of frequencies with experiments and observations.

The turn of the 21st century revived interest on the booming phenomenon and increased the amount of field data on booming emissions. Patitsas (2003) contributed a new quantitative explanation of the booming frequency in terms of fluidized granular beds, similar

to the shear band argument presented in Hidaka *et al.* (1988), to explain sound generated by a compressed granular material. Andreotti (2004) measured the booming frequency (f = 100 ± 5 Hz) at a barchan sand (D = 0.180 mm) dune near Tarfaya in Morocco and suggested that the sound frequency is controlled by the shear rate inside of the avalanche and the average grain size of sand. Andreotti presented a new theoretical model based on elastic waves generated by the avalanche that synchronizes the avalanching sand grains and proposed a wave-particle mode locking mechanism. Douady *et al.* (2006) performed field experiments at Ghord Lahmar near Tarfaya, Morocco (f = 105 ± 5 Hz, D = 0.160 mm), Mar de Dunas near Copiapo, Chile (f = 90 ± 10 Hz, D = 0.210 mm) and El Punto de Diabolo near Copiapo, Chile (f = 75 ± 10 Hz, D = 0.270 mm) and agreed with Andreotti (2004) about the scaling between frequency and diameter. Douady *et al.* proposed an alternative theory for the generation of the booming sound where grains synchronize their motion through a slow-propagating coupling wave in the sheared layer. Each layer of grains moves simultaneously under the influence of this coupling wave and therefore neither the velocity, nor the pushed mass, but the mean applied shear controls the sound frequency. Bonneau *et al.* (2007) introduced a theory involving totally refracted surface elastic waves due to stratified layers in a booming dune. A waveguide effect due to nonlinear Hertzian contacts between grains results in a discrete number of modes and a waveguide cutoff frequency. More recently Patitsas (2008) posed that his developed theory for sound from forced compression generated by a pestle creating standing waves can be applied to the slumping events on a dune as well such that "*the boundary layer plays the role of the violin string and the dry sand band below, reported to be about 1.5 m thick, plays the role of the sound box.*" Mills and Chevoir (2009) introduced a recent new theory of sound emission due to avalanching based on an intermittent regime near the jamming transition. The slope of the avalanches changes during the alternation between the jammed system with force chains in the compression direction and the flowing system with stick-slip motion along the surface.

1.4 Thesis Outline

This thesis focusses on two different but interrelated topics; booming sand dunes and dune stratigraphy and migration. Recent developments and new explanations for the phenomenon of booming sand dunes have produced heated discussions and strong scientific discords.

The amount of verifiable data for true sustained booming avalanches is very limited when brief forced shearing or compression events are excluded. The correct mechanism for the generation of the booming sound should explain all characteristics and be consistent with the field observations. The existing theoretical models for the generation of booming sound are presented in the first part of chapter 2 and shortcomings of each approach are clarified. The later part of chapter 2 proposes an alternative waveguide theory for the booming mechanism that explains all the characteristics of field observations and measurements.

Extensive field work complements and confirms the new waveguide model of booming sand dunes. Chapter 3 presents the short letter "Solving the mystery of booming sand dunes" published in Geophysical Review Letters in 2007 introducing the new model and presents preliminary data. Andreotti *et al.* (2008) argues in a comment submitted to Geophysical Review Letters in 2008 that for the non-dispersive model "*no plane wave Fourier mode can exist in such a medium; only an infinite number of surface modes guided by the sound speed gradient may propagate.*" Chapter 3 reproduces the rebutal "Reply to comment by B. Andreotti et al. on *"Solving the mystery of booming sand dunes"*" published in Geophysical Review Letters in 2008. The rebuttal explains and clarifies that body wave may exist in a medium where the speed increases with depth and that constructive interference and resonance are still possible, even when curved ray paths are included in the analysis.

There are several longer papers in preparation that are currently still unpublished. Chapter 5 describes the differences in wave characteristics between avalanching booming events and forced shear burping events based on extensive field experiments. This paper extends the waveguide theory for a varying subsurface structure and investigates the type and properties of waves associated with the booming and burping phenomena. Chapter 6 focusses on the internal stratigraphy of dunes, where observations from geophysical field experiments at two different dune locations provide important insights into the formation and migration of different dune types.

Chapter 7 summarizes the observations made in the course of this study. This chapter connects the measurements of the dune structure with calculations of the booming frequency for multiple observation dates, comments on the variability of booming and shows a positive quantitative and qualitative correlation between the subsurface layer, the velocity structure and the incidence of booming. The latter part of this chapter presents a perspective on open questions that still remain.

Chapter 2

Theoretical Models for Booming Sand Dunes

2.1 Existing Theories

2.1.1 Shearing and Dilatation of Dry Sand

Ralph Alger Bagnold was schooled as a engineer and served as a soldier in both world wars. Bagnold traveled extensively through the Libyan and other deserts and developed research on sand transport by wind which he published in Bagnold (1941). He extended his research on the dilatation of solids under uniform shear for a gravity-free environment (Bagnold, 1954) to an environment under influence of gravity in Bagnold (1966). The latter paper presents results in the context of shearing and dilatation of dry sand in booming sand dunes and claims that the data obtained by shearing wax spheres predicts the frequency of the booming sound.

The dilatation of an array of solids is defined as the mean free separation distance between solids divided by the mean diameter of these solids. Bagnold defined three different regimes of the dilatation in terms of the linear concentration λ:

$$\frac{1}{\lambda} = \left(\frac{C^\star}{C}\right)^{1/3} - 1, \tag{2.1}$$

with $C^\star$ the maximum volume concentration at closest packing for the granular material.

This relation is valid for both spherical and non-spherical particles. For natural angular

beach sand of diameter $D = 0.318 - 0.414mm$, Bagnold found:

$$\begin{cases} \lambda_0 = \infty & C = C^\star \approx 0.644, \\ \lambda_1 = 48 & C \approx 0.604, \\ \lambda_2 = 19 & C \approx 0.555, \\ \lambda_3 = 12.4 & C \approx 0.510, \end{cases} \tag{2.2}$$

with the fluidic Newtonian region for $\lambda < \lambda_3$, the fluidic non-Newtonian region for $\lambda_3 < \lambda < \lambda_2$, the static region for $\lambda_2 < \lambda < \lambda_0$, with $\lambda = \lambda_1$ forming a critical concentration related to the angle of repose. Bagnold furthermore defined two different shear regimes based on a ratio of inertial and viscous forces: the solid-inertial and the fluid-viscous phase with an transition region between the two regions. Bagnold deduced based on the properties of sand that shearing conditions in booming sand dunes are entirely inertial; grain inertia dominates and viscous effects become irrelevant. Hunt *et al.* (2002) questioned the exact definition of grain inertia regime as numerical calculations indicated that this regime was a result of experimental errors. An alternative measure for the importance of viscous damping and elastic collisions is the Stokes number $St = \frac{1}{9} Re \frac{\rho_p}{\rho_a}$, with particle density ρ_p and density of the air ρ_a. A Reynolds number of $Re = 13$ for flow of grains in air leads to a Stokes number above $St > 1000$, indicating that elastic collisions are indeed dominant (Joseph and Hunt, 2004).

The stress $\sigma = mg - P$ on a sand grain is a superposition of the weight, or overburden, of the sand grains above it and normal dispersive stress. The critical displacement velocity U_c shears the sand resulting in a small upward displacement and consequent jump forward of the entire overburden. The dilatation is $\frac{1}{\lambda_3}$ if the contact surface clears after each collision. This overburden rises and falls each time a distance of $s = \frac{D}{\lambda_3}$ in free fall and only experiences applied stress near the minimum dilatation. The overburden is subject to oscillations due to upward acceleration by dilatation and downward fall by gravity. Synchronization occurs if the entire overburden saltates on top of the sheared surface.

Simple mechanics is able to find an expression for the frequency of these oscillations.

The position of a mass in free fall is given by:

$$s = \frac{1}{2}gt^2, \tag{2.3}$$

with the travel distance of a particle during free fall s, the gravitational acceleration g and the time t. The particle velocity $u = gt$ is

$$u = (2gs)^{1/2}. \tag{2.4}$$

The frequency of the oscillations of dilatation and free fall is the critical velocity U_c divided by the distance traveled during one oscillation:

$$f_{osc} = \frac{U_c}{2s} = \frac{U_c\lambda_3}{2D} = \sqrt{\frac{g\lambda_3}{2D}}. \tag{2.5}$$

This expression differs by a factor two with the one presented in Bagnold (1966):

$$f_{osc} = \sqrt{\frac{g\lambda_3}{8D}}. \tag{2.6}$$

Using the average diameter $D = 0.20mm$ and $\lambda_3 = 12.4$ for beach sand results in an oscillation frequency of 275 Hz, equation (2.6), or 551 Hz, equation (2.5), which is almost an order of magnitude higher than the booming frequency measured in the field. An average diameter does not uniquely define a sample as a sand sample consists of a distribution in sizes of sand grains. No rationale is provided by the author for the existence of higher harmonics occurring in the acoustic emission of a booming dune. Last, not all dunes boom all year long and therefore the existence of the booming emission cannot solely depend on particle characteristics.

2.1.2 Fluidized Granular Beds

Patitsas contributed a new quantitative explanation of the booming frequency in (Patitsas, 2003) in terms of fluidized granular beds. He assumes that the sand under shear is fluidized with an average random fluctuation velocity $\bar{v}$ dependent on the relative flow velocity δu between adjacent shear layers. Because of this fluidization, the equations of fluid mechanics are applicable.

The viscosity of the bed is proportional to the non-constant collision rate. The measure for the inelastic grain–grain collisions, Γ, is expressed in terms of the coefficient of kinetic friction μ and the coefficient of restitution e:

$$\Gamma = \frac{1+e}{4}\left[\frac{1-e}{4} + \frac{\mu}{\pi} - \frac{1+e}{4}\mu^2\right]. \tag{2.7}$$

Patitsas introduces $q_1\dfrac{\Delta u}{\bar{v}} - \Gamma$ as the parameter that determines if forced sand sings or avalanching sand booms. The parameter q_1 is a dimensionless factor in the expression for the shear stress. If $q_1\dfrac{\Delta u}{\bar{v}} - \Gamma < 0$ there are no stick-slip effects in the bed and no dilatation occurs in the shear zone. This prevents the sand from singing and booming. For sand sheared with $q_1\dfrac{\Delta u}{\bar{v}} - \Gamma > 0$, stick-slip and dilatation occurs and the fluctuation velocity displays a harmonic behavior for forced sand and a Bessel function behavior for avalanching sand.

Failure occurs in regions with high fluctuation velocities. Regions of failure in granular beds transform into slip channels where grain layers slip over each other. These weak regions form the energy source of the acoustic emission. The acoustic phase velocity within the slip channels needs to be at a low value of 1 m/s. The vibration frequency of the acoustic emission depends directly on the width of the slip channel. The first overtone enhances the energy transfer from gravitational potential energy to vibrational energy resulting in a self-generating resonance process. Patitsas suggests that an increase in air humidity causes a thicker water coating on the sand grains. This water coating influences the friction and restitution coefficient and thus could switch the sign resulting in nonboomable conditions.

Patitsas establishes a quantitative measure of the ability of sand to produce acoustic emissions. A strong part of his analysis is the explanation of a condition that would prevent booming from occurring based on a quantitative argument. The overtones of the emission are related to a resonance process within the slip channel. The exact calculation of the vibration frequency is unclear, the only guideline is that the frequency depends directly on the width of the slip channel. The validity of the use of the equations of fluid mechanics and the existence of modes of vibration are put in question by Patitsas (2003, p. 302) himself. The author also does not back the claim by measurements or references of an acoustic phase velocity of 1 m/s within the slip channels.

2.1.3 Synchronization due to Phase Locking

Andreotti proposed that a sand avalanche excites elastic waves at the surface of the dunes. These elastic waves exert feedback on the particle motion providing partial synchronization by a wave-particle mode locking. Andreotti (2004) measured the booming frequency ($f = 100 \pm 5$ Hz) on a barchan dune in the Sahara desert in Morocco. He argued that the frequency is only dependent on the properties of the grain dynamics inside the avalanche, such as particle diameter ($D = 0.18$ mm) and shear velocity. The elastic waves are located close to the surface as the vibration quickly attenuates at a depth of 10 cm. The measured phase speed (40 m/s) is two orders of magnitude lower than the body wave velocity in quartz. Andreotti denotes the elastic waves as Rayleigh-Hertz waves and establishes a dispersion relation:

$$f = c^{2/3} g^{1/6} \lambda^{-5/6}, \tag{2.8}$$

with wavelength λ and speed of sound $c = 230$m/s obtained by fitting the dispersion relation.

Andreotti introduces the velocity gradient Γ as "the typical rate at which grains jump over their neighbors and make collisions" and notes that it "is independent of the flowing depth h." The balance between potential and kinetic energy results in a limiting velocity between two adjacent grain layers equal to $\sqrt{gD}$. Laboratory experiments showed that the velocity gradient has exactly the same value as the booming frequency on sand dunes and therefore Andreotti proposed that the booming frequency f is equal to the velocity gradient Γ such that:

$$\Gamma \simeq 0.4 \sqrt{\frac{g}{D}} = f. \tag{2.9}$$

No rational for the factor 0.4 is given other than that it fits the data of frequency and diameter measured in the current study and the data point provided by Criswell *et al.* (1975) and Lindsay *et al.* (1976) for shoveling sand ($D = 0.380$ mm and $f_{bp} = 66$ Hz). Andreotti argues that the collisions of grains excite larger-scale elastic waves that are synchronized by wave-particle mode locking. Andreotti also notes that for inhomogeneous flow, inertial effects have to be added to the gravity and hence the velocity gradient should be modified.

In a follow-up paper (Bonneau *et al.*, 2007), Andreotti and co-workers extended the Rayleigh-Hertz wave theory. They argued that the sand grains are stratified in layers due to gravity, resulting in refraction of waves to the surface. The sound wave speed, varying as

$c \propto P^{1/4}$ for large confining pressures and $c \propto P^{1/6}$ for small confining pressures, increases with depth and creates bending of rays toward the surface. The influence of the vanishing confining pressure near the surface on sound wave propagation remains unaddressed. The authors do not provide exact velocity profiles with depth or specify an exact length scale or velocity increase at which this process of bending of waves occurs.

Bonneau *et al.* argue that coherent elastic modes are excited as a result of nonlinear Hertzian contact and dispersion. The elastic waves synchronize the collisions which excite the elastic wave resulting in an amplitude increase. A waveguide cutoff exists due to the finite depth of the layers, resulting in the inability to propagate sound. A coupling between the avalanching grains and surface elastic waves results in the song of the dunes.

The authors state that the non-propagative resonant mode is around 73 Hz, which corresponds to a waveguide depth of 47 cm, "which is indeed the typical depth at which the first wet layer may be found on dry days." This claim is unfounded as neither the velocity in the dune, nor the depth of the wet layer is measured in the current study and no references are made toward other studies in literature.

The authors identify two different length scales that are important in booming: the shearing of the particles on the grain-scale and a waveguide effect within the scale of the dune. The frequency of booming is determined solely from particle characteristics $f = 0.4\sqrt{g/D}$ while the internal waveguide cutoff frequency influences the ability of the dune to boom due to the finite width of subsurface layers. In private communication, Andreotti acknowledged that field experiments showed that the booming frequency changes from day to day based on environmental parameters. Bonneau *et al.* (2007) did not conduct measurements of wave propagation of booming in situ and no rationale is provided as to whether the waveguide influences the booming frequency directly.

Andreotti and Bonneau (2009) shared recently a currently unpublished manuscript in personal communication. The authors classify three contradictory dynamical mechanisms for the booming emission: (i) quasi-periodic stick-slip motion (Bagnold, 1966; Patitsas, 2008), (ii) incoherent source selected by resonance over the thickness of the avalanche (Douady *et al.*, 2006) or the thickness of a dry layer (Vriend *et al.*, 2007) and (iii) selective acoustic amplifier emitting coherent elastic modes that synchronize grain motion (Andreotti, 2004; Bonneau *et al.*, 2007). The authors propose yet another mechanism based on a "linear stability analysis of the homogeneous avalanche." The amplification of the sound is due to

exponential growth of elastic waves within the flowing layer that is bordered by a thin shear band on the bottom of the avalanche. The authors assume in the theoretical derivation of the dispersion relation that the system homogeneous in time and lateral direction and changes properties with depth. The local maximum of the growth rate creates a mode that propagates and grows in one direction (either downslope or upslope). The manuscripts states that "guided modes are selected by the condition of constructive interference between plane waves as they bounce back and forth." The shear band that separates the flowing and the static part of the avalanche induces a "coherent amplification of guided elastic waves."

2.1.4 Self-synchronization in a Resonance Cavity

Douady and co-workers proposed that the frequency of the sound is related to the relative motion of the sand grains (Douady *et al.*, 2006). The team performed field experiments at Ghord Lahmar in Morocco ($f = 100 \pm 5$ Hz, $D = 0.16$ mm), Mar de Dunas in Chile ($f = 90 \pm 10$ Hz, $D = 0.21$ mm) and Cerro Bramador ($f = 75 \pm 10$ Hz, $D = 0.27$ mm) and claimed that the frequency-diameter relation proposed by Bagnold (1966) and Andreotti (2004) holds well. A laboratory experiment consists of a blade rotated in a channel of singing sand by controlling the shearing velocity and mass of sheared sand. The experiment shows that the mean shear determines the frequency (25-250 Hz) and that neither the velocity, nor the mass influences the sound frequency. This results according to the authors in the confirmation of the hypothesis of Poynting and Thompson (1909) that the relative motion of the sand grains is the sound producing mechanism.

Douady *et al.* poses that the avalanche synchronizes because of a coupling between the different layers of flowing grains. The characteristic velocity c_c of this coupling wave and the height of the sheared layer h are related by the dispersion relation of linear waves:

$$f = \frac{c_c}{h}. \tag{2.10}$$

A threshold velocity of $c_{cl} = 0.47$ m/s in the laboratory experiment forms the minimum velocity below which no sound is produced. In booming avalanches, this threshold surface velocity reduces to $c_{cd} = 0.23$ m/s because of different boundary conditions. The authors suggest that these coupling waves might be shear waves and recommend that additional research should be done to study the existence and the origin of the coupling waves.

Douady *et al.* focuss solely on the grain perspective and the dimensions of the avalanching layer. The authors argue that when the surface velocity of the avalanche is too low, the sand is not able to produce booming. The laboratory experiment in Douady *et al.* (2006) exerts a continuous shear on a sand bed, but this produces sound in a granular material from forced shearing (subsection 1.2.2) and not sound due to slumping. The authors do not comment or provides measurements on the relation between the speed of the "coupling wave" and regular acoustic or elastic wave speeds in a granular bed.

2.1.5 Jamming Transition

Mills and Chevoir (2009) introduces an instable regime for avalanching particles close to the jamming transition. The jammed state freezes the grains, force chains form a rigid network and the surface slope increases beyond the internal friction angle such that grains start to avalanche. The flowing grains dilate and undergo a stick-slip behavior in which the slope decreases to a stopping angle and the flow freezes again. The flow switches between the frozen state and the dilated flowing state and creates an oscillation between the two instabilities with a well-defined frequency:

$$f_{osc} = \frac{1}{2\pi}\left(\frac{g}{\alpha d}\right)^{1/2}, \tag{2.11}$$

with the factor α depending on the velocity profile. The authors argue that the functional dependence of the frequency is equal to the oscillation frequency, equation (2.6), found by Bagnold. The current approach defines the booming frequency in terms of particle characteristics and arrives at similar expressions as found in other studies (Andreotti, 2004; Douady *et al.*, 2006). Mills and Chevoir (2009) acknowledge the necessary condition of monodispersed grains for a well-defined frequency and identify that a silica layer on the grains (Goldsack *et al.*, 1997) may increase the difference in friction coefficient between the frozen and flowing state. The theoretical study lacks any new data from field or laboratory experiments for validation.

2.2 Constructive Interference in a Waveguide

2.2.1 Reflection and Transmission at an Interface

The source of the booming is positioned at a certain location on the surface of the dune. Plane waves exist at some distance from the source in radial direction. The waves also travel in the third direction and are reflected at different angles from subsurface layers. Assume a uniform layer of sand with thickness H, propagation velocity c_1 and density ρ_1. The overlying atmosphere has a velocity c_0 and density ρ_0 and the subsurface half space beneath has velocity c_2 and density ρ_2, as shown in figure 2.1. A velocity sandwich structure is

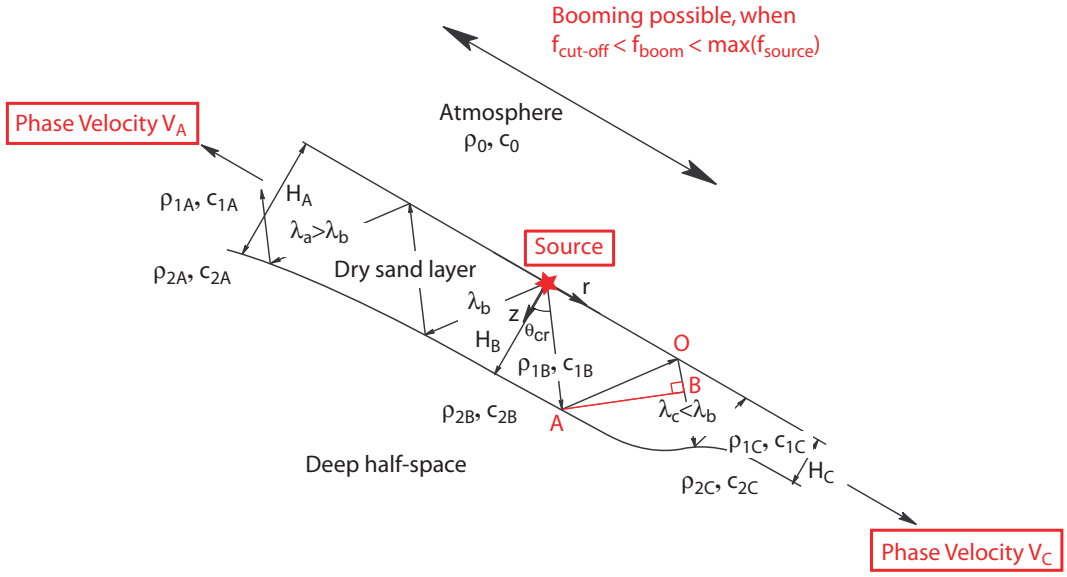

Figure 2.1: The interaction between booming frequency and phase velocity in the waveguide model.

formed as the dry sand layer has a lower velocity than the surrounding layers: $c_1 < c_0$ and $c_1 < c_2$. The boundary conditions are expressed in terms of the vertical particle velocity and the pressure for acoustic vibrations.

In the case of no partitioning at the boundary, the angle of incidence is equal to the angle of reflection and Snell's law applies for the refracted wave. When the angle of incidence ϕ_1 is equal to the critical angle $\sin(\phi_{cr}) = \frac{c_1}{c_2}$, the wave is internally refracted ($\phi_1 = \phi_{cr}, \phi_2 = 90°$). For incidence angles equal or larger than the critical angle, no energy propagates into the

substrate half space and the phase speed along the interface V_{int} reduces to:

$$V_{\text{int}} = \frac{c_1}{\sin(\phi_{cr})} = c_2. \tag{2.12}$$

For an incidence angle $\phi_1 < \phi_{cr}$, the reflection R and transmission T coefficients have a value between zero and one. For the critical angle and beyond, no energy leaks outside of the waveguide, $T = 0$ and $R = 1$, and the amplitude is preserved for all distances $A = A_0$. Attenuation with distance is expected because of the cylindrical spreading of the waves in the natural waveguide at the desert dunes.

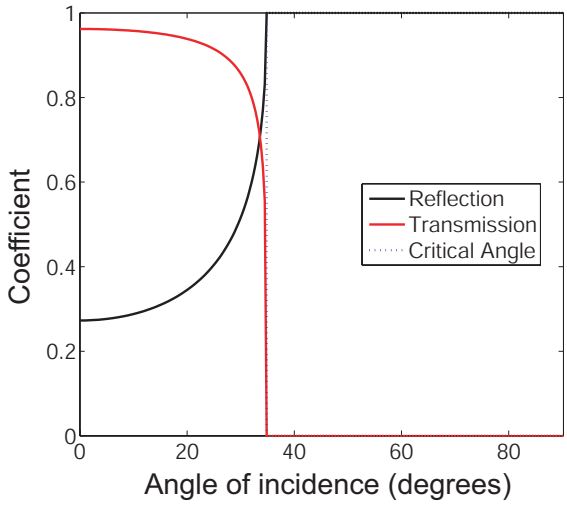

Figure 2.2: Reflection and transmission coefficient (Lay and Wallace, 1995) as a function of angle. Parameters used are $\rho_1 = \rho_2 = 1500$ kg/m^3, $c_1 = 200$ m/s, $c_2 = 350$ m/s and H = 2.0 m.

2.2.2 Wave Propagation in a Waveguide

Ray tracing

For constructive interference the analysis of the waveguide in terms of ray tracing follows the derivations presented in Ewing *et al.* (1957) and Officer (1958). Assume that the waveguide depth H is constant across a certain length and that the velocities c_0, c_1, c_2 are constant in each layer. The seismic velocity usually increases with depth in a granular material, but Vriend *et al.* (2008) showed that this increase is smaller than the large velocity jump across the interface between medium 1 and 2. The propagating waves are traveling in phase within

the waveguide in the case of constructive interference. For a given wave at incident angle ϕ_1, the extra distance traveled by a wave $\bar{AB}$ in figure 2.1 is:

$$\bar{AB} = \bar{AO} + \bar{OB} = H\left[\frac{1}{\cos(\phi_1)} + \frac{\cos(2\phi_1)}{\cos(\phi_1)}\right] = 2H\cos(\phi_1). \tag{2.13}$$

Officer (1958) defines the condition for constructive interference as the total phase change equal to a factor depending on the mode number n:

$$k_n\bar{AB} - \epsilon_{10} - \epsilon_{12} = 2n\pi. \tag{2.14}$$

The phase change involved with the ray path from A to B depends on the wave number $k_n = 2\pi/\lambda_n$, the wavelength $\lambda_n = c_1/f_n$ and the distance traveled by the wave AB.

Substituting the wave number and wavelength and taking the tangent on both sides of equation (2.14):

$$\tan\left(\frac{2\pi H\cos(\phi_1)f_n}{c_1}\right) = \tan\left(\frac{(\epsilon_{10}+\epsilon_{12})}{2} + n\pi\right). \tag{2.15}$$

The phase lag at the surface ϵ_{10} and the bottom ϵ_{12} are derived from the reflection coefficient R (Officer, 1958, p. 79) as:

$$\frac{\epsilon_{12}}{2} = \tan^{-1}\left[\frac{\rho_1\sqrt{\left(\frac{c_1}{V_{\text{int}}}\right)^2 - \left(\frac{c_1}{c_2}\right)^2}}{\rho_2\sqrt{1-\left(\frac{c_1}{V_{\text{int}}}\right)^2}}\right]. \tag{2.16}$$

and

$$\frac{\epsilon_{10}}{2} = \tan^{-1}\left[\frac{\rho_1\sqrt{\left(\frac{c_1}{V_{\text{sur}}}\right)^2 - \left(\frac{c_1}{c_0}\right)^2}}{\rho_0\sqrt{1-\left(\frac{c_1}{V_{\text{sur}}}\right)^2}}\right]. \tag{2.17}$$

The current analysis deviates from the treatment by Officer (1958), where $\epsilon_{10} = \pi$ and $\epsilon_{12} = 0$, as the waveguide in a sand dune has a mirrored velocity structure for which $c_0 = c_2$. In the case of critical refraction, the coupling provides the feedback to the waveguide and the phase speed along the surface interface reduces to $V_{\text{sur}} = c_0$, producing zero phase lag $\epsilon_{10} = 0$ at the top surface (Officer, 1958, p. 228). Similarly, critical refraction ensures a phase speed of $V_{\text{int}} = c_2$ along the interface between medium 1 and 2 and zero phase

lag at the bottom surface as well. As a consequence of critical refraction, the phase lag is independent of the density and/or the impedance differences across interfaces. Therefore, equation (2.15) reduces to:

$$\tan\left(\frac{2\pi f_n H\cos(\phi_{cr})}{c_1}\right) = 0. \tag{2.18}$$

Solutions are given in terms of the mode number n with n = 1, 2, 3,...

$$\frac{2\pi f_n H\cos(\phi_{cr})}{c_1} = n\pi, \tag{2.19}$$

and

$$f_n = \frac{n}{2}\frac{c_1}{H\sqrt{1-\left(\frac{c_1}{c_2}\right)^2}}, \tag{2.20}$$

The resonant mode $n = 0$ is the non-propagating, standing, mode in the waveguide that does not travel in r-direction and has zero phase speed and zero frequency. The n-th overtone exists for frequencies equal or greater than the cutoff frequency as prescribed by equation (2.20).

Continuous guided wave

An alternative approach to derive this formula is to analyze the waveguide in the continuous sense following Sleep and Fujita (1997). For wave propagation at long ranges and at moderate to low frequencies, the normal-mode solution combines interference effects from all ray paths. The trial function ϕ of a planar geometry with a standing wave in z-direction and a propagating wave in r-direction with rigid boundaries is:

$$\phi = \cos(k_z z)\exp\left(i\left[k_r r - \omega t\right]\right). \tag{2.21}$$

The wave propagates within the waveguide in horizontal direction with a constant phase velocity $V_1 = \omega_1/k_1$, with $k_1 = \sqrt{k_r^2 + k_z^2}$ and $\omega_1 = 2\pi f_1$. At the upper boundary $z = 0$, the boundary condition of zero displacement $\partial\phi/\partial z = 0$ is satisfied. At the bottom the boundary condition at $z = H$ is satisfied if $k_z H = n\pi$, with integer n. The trial function ϕ

including all modes n is:

$$\phi = \sum_{-\infty}^{\infty} \phi_n \cos\left(\frac{n\pi z}{z_0}\right) \exp\left(i\left[k_r r - \omega t\right]\right). \tag{2.22}$$

The wave equation is:

$$\frac{\partial^2 \phi}{\partial t^2} = c_1^2 \left[\frac{\partial^2 \phi}{\partial r^2} + \frac{\partial^2 \phi}{\partial z^2}\right], \tag{2.23}$$

with the p-wave velocity $c_1 = \sqrt{\lambda_1/\rho_1}$.

Substituting the trial function from equation (2.22(into the wave equation (2.23) gives:

$$-\omega_n^2 = c_1^2\left[-k_r^2 - k_z^2\right] = c_1^2\left[-k_r^2 - \left(\frac{n\pi}{H}\right)^2\right]. \tag{2.24}$$

The incident angle ϕ_1 is orientated as:

$$\tan(\phi_1) = \left(\frac{k_r}{n\pi/H}\right), \tag{2.25}$$

such that:

$$\omega_n = c_1\left(\frac{n\pi}{H}\right)\sqrt{\tan(\phi_1)^2 + 1} = c_1\left(\frac{n\pi}{H}\right)\sqrt{\frac{1}{\cos(\phi_1)^2}} = c_1\left(\frac{n\pi}{H}\right)\frac{1}{\cos(\phi_1)}. \tag{2.26}$$

Restructuring this equation in terms of the frequency and substituting incidence at the critical angle $\phi_1 = \phi_{cr}$ gives:

$$f_n = \frac{\omega_n}{2\pi} = \frac{n}{2}\frac{c_1}{H\sqrt{1 - \left(\frac{c_1}{c_2}\right)^2}}, \tag{2.27}$$

which is the same resonance relation as equation (2.20) found via ray tracing.

2.2.3 Phase Velocity

The booming waves travel at a phase speed V situated between the seismic speed of the dry layer of sand c_1 and the seismic speed of the denser, deeper layer of sand c_2. As the subsurface structure of the dune changes in the uphill or downhill direction (illustrated in figure 2.1), the phase velocity also changes independent of the frequency of the source. At a given moment in time a seismic sensor measures the global booming frequency and the

local phase velocity. The phase velocity adapts as the waves move into a different velocity or layering structure. A sensor on the desert floor, located roughly 500 meters from the booming dune slope, measured the same booming frequency (82 Hz) as the local recording, as shown in figure 2.3, but a much higher phase velocity (∼500 m/s).

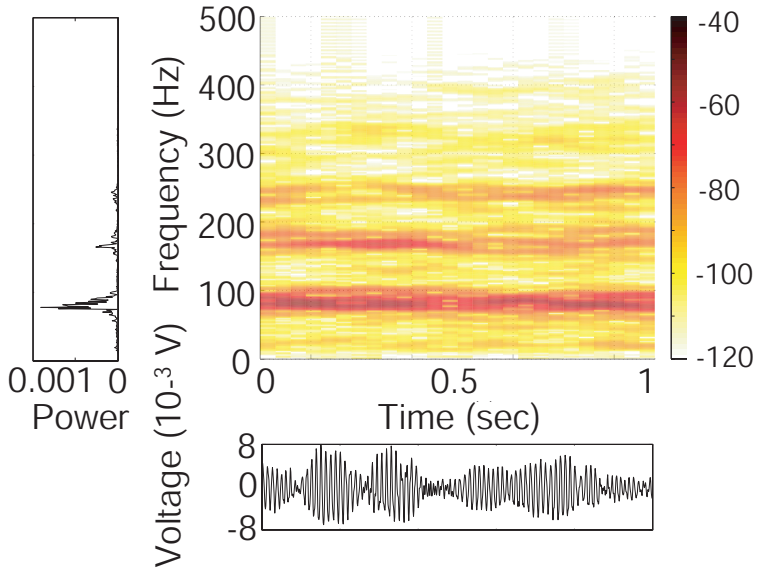

Figure 2.3: Seismic response of a booming emission at a distance of approximately 0.5 km.

The local phase velocity depends on the local depth of the layering H_A, the local velocities c_{1A} and c_{2A} and the global booming frequency $f = f_{\text{cutoff}}$ obtained from equation (2.27). For known dimensions, velocities and booming frequency, the local phase velocity V_A is obtained by solving the transcendental equation:

$$\tan\left(f_{\text{cutoff}}\frac{2\pi H_A}{c_1}\sqrt{1-\left(\frac{c_{1A}}{V_A}\right)^2}\right) = \frac{\rho_1}{\rho_2}\frac{\sqrt{\left(\frac{c_{1A}}{V_A}\right)^2-\left(\frac{c_{1A}}{c_{2A}}\right)^2}}{\sqrt{1-\left(\frac{c_{1A}}{V_A}\right)^2}}. \tag{2.28}$$

In the example of figure 2.1, the depth of the layering increases uphill from the source creating a longer wavelength $\lambda_a > \lambda_b$ and physically signifies the approach of the dune crest (Vriend *et al.*, 2010a). As the subsurface velocity commonly is smaller close to the crest (Vriend *et al.*, 2007), the phase velocity decreases significantly uphill from the source $V_a < V_b$. The example also shows a thinning in downhill direction, where the subsurface velocity increases, occurring in grainfall areas (Vriend *et al.*, 2010a). The local wavelength decreases $\lambda_c < \lambda_b$ and the phase speed increases $V_c > V_b$. An alternative waveguide structure

of thickening in downhill direction occurs at the transition of grainfall and grainflow regions. The increase in subsurface velocity and the increase in depth are two competing factors that have an opposite effect on the phase speed. Usually the increase in downhill velocity dominates the increase in depth such that the effective phase speed increases.

2.3 The Interaction between the Waveguide and Booming

A functioning waveguide prohibits energy loss and promotes amplification of the source. There are several consequences for the waveguide theory for booming sand dunes:

1. The source frequency excites the natural resonance frequency of the waveguide and the avalanching of grains provide the energy necessary for the emission.

2. The layering in the region of the source sets the global booming frequency; away from the source the phase speed may change and the amplitude may decrease due to leakage.

3. The dimensions of the waveguide may prevent the excitation to be constructive and limit amplification of the source.

2.3.1 Excitation by a Source

Direct shearing of sand at the surface generates short pulses, defined as the burping emission by Vriend *et al.* (2010b). The burping source provides a continuous energy input to excite a selection of modes in the waveguide and is necessary to initiate the booming emission. The source spectrum of the burp presented in figure 2.4 involves frequencies in a wide range (50-100 Hz, varies slightly depending on shear rate) at low amplitude.

The total acoustical amplitude of the booming emission is more than an order of magnitude higher than that of a burping emission. The excess energy needs to be supplied by another mechanism as the total energy of the acoustic emission cannot be increased. The release of gravitational energy into kinetic energy due to the avalanching sand provides this additional source of energy. As described in section 2.2, the narrow booming frequency is set by external factors such as the waveguide dimensions and the speed of sound. The avalanching of grains supply energy for amplification while the burping emission provides the broad frequency content to excite the booming frequency. When the avalanching of sand stops, the amplitude of the booming stops growing and diminishes slowly with time. However,

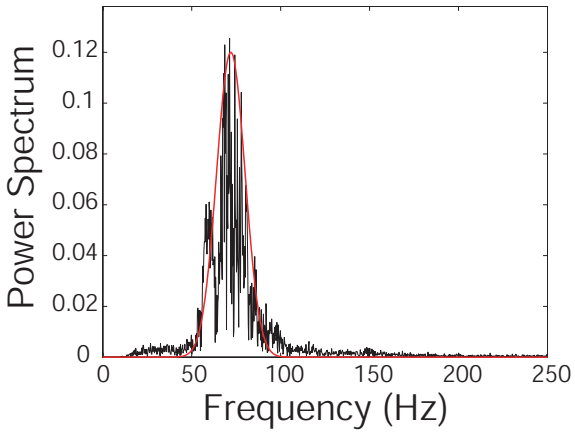

Figure 2.4: Source spectrum of a shearing event on the slip face at Eureka dunes on 07/18/2008. The burping source is fitted with a Gaussian-shaped function with constant $C = 0.12$, center frequency $f_{\text{cent}} = 72$ Hz and width of the pulse $\sigma = 8$.

the sound may continue for up to a minute as the energy continuous to reverberate in the waveguide.

2.3.2 Relation between Frequency and Phase Speed

The dispersion relation given in equation (2.28) provides a relation between the phase velocity V and the frequency f of a mode. A graphical technique finds the solutions of the transcendental equation for each mode $n = 1, 2, ..$ in figure 2.5. The intersection of the

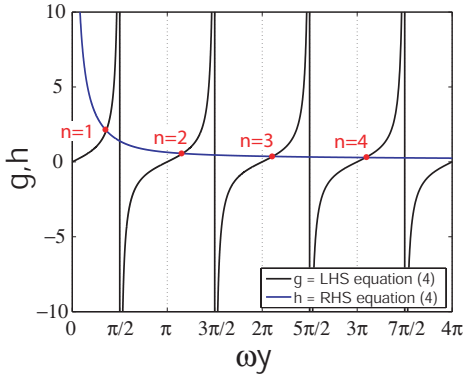

(a)

Figure 2.5: Graphical representation of finding the roots of the dispersion relation. Parameters used are $\rho_1 = \rho_2 = 1500$ kg/m^3, $c_1 = 200$ m/s and $c_2 = 350$ m/s.

two functions $g(\omega y)$ and $h(\omega y)$, representing the left- and right-hand side of equation (2.28)

respectively, are solutions to the dispersion relation. The phase velocity along the interface has a value between c_1 and c_2 and is maximum at the cutoff frequency $\omega_{\text{cutoff,n}}$, calculated by equation (2.20) of a specific mode number. The booming emission propagation speed is between V = 200 m/s and V = 250 m/s (Vriend *et al.*, 2010b). The mode $n = 1$ needs to be excited by the burping source in order to generate a propagative wave.

2.3.3 Changing Dimensions of the Waveguide

The cutoff frequency determined by the waveguide dimensions needs to overlap with part of the source spectrum of the burping emission. Figure 2.6 shows the waveguide modes for common parameters found in field experiments. Mode $n = 1$ overlaps slightly with the source spectrum such that energy may be transferred. Figure 2.6 presents the modes for a smaller, nonbooming dune. Mode $n = 1$ overlaps significantly with the source spectrum, but no sustained booming can be generated. The subsurface velocity $c_2 = 600m/s$ is very high and the symmetry between the atmosphere and the subsurface deeper layer breaks down as $c_0 \neq c_2$. Furthermore, the length of the waveguide channel in the smaller dune is of the same order of magnitude as the wavelength of booming $\approx$ 2.5m and its length is insufficient to create an amplification of the sound. A similar situation occurs for a very deep waveguide where the wavelength for constructive interference exceeds the size of the avalanche. The situation for a nonbooming dune in the wintertime is presented in figure 2.6c. The hard substrate layer is preserved, but the upper layer velocity c_1 increases significantly due to a larger moisture content. The first mode cannot be excited as its cutoff frequency is higher than the source spectrum. A similar mode spectrum occurs if the waveguide depth is very shallow (figure 2.6d) and the cutoff frequency is beyond the maximum frequency of the source.

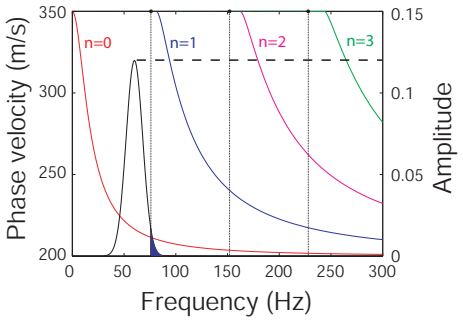

(a) Booming dune ($c_1 = 200$ m/s, $c_2 = 350$ m/s and H = 1.5 m)

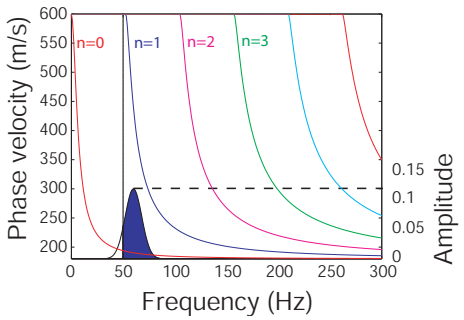

(b) Nonbooming small dune ($c_1 = 180$ m/s, $c_2 = 600$ m/s and H = 1.8 m)

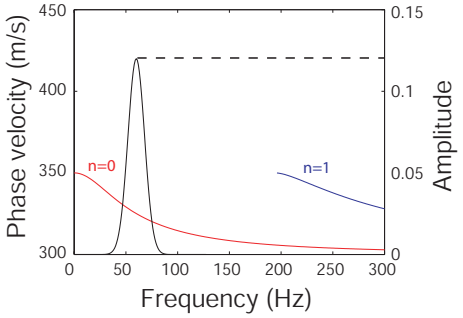

(c) Nonbooming winter dune ($c_1 = 300$ m/s, $c_2 = 350$ m/s and H = 1.5 m)

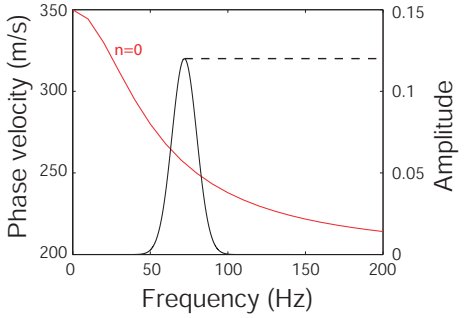

(d) Nonbooming dune with a shallow waveguide ($c_1 = 200$ m/s, $c_2 = 350$ m/s and H = 0.5 m)

Figure 2.6: Waveguide modes. The mode $n = 0$ is non-propagative and cannot be responsible for the booming emission. Booming exist if the excitation frequency is equal or larger than the cutoff frequency.

Chapter 3

Solving the Mystery of Booming Sand Dunes

Desert booming can be heard after a natural slumping event or during a sand avalanche generated by humans sliding down the slip face of a large dune. The sound is remarkable because it is composed of one dominant audible frequency (70 to 105 Hz) plus several higher harmonics. This study challenges earlier reports that the dunes' frequency is a function of average grain size by demonstrating through extensive field measurements that the booming frequency results from a natural waveguide associated with the dune. The booming frequency is fixed by the depth of the surficial layer of dry, loose sand that is sandwiched between two regions of higher compressional body wave velocity. This letter presents measurements of the booming frequencies, compressional wave velocities, depth of surficial layer, along with an analytical prediction of the frequency based on constructive interference of propagating waves generated by avalanching along the dune surface.

3.1 Introduction

Explorers including Marco Polo (Polo, 1295) in the Gobi Desert, the Emperor Baber (Curzon of Kedleston, 1923) in Afghanistan and Charles Darwin (Darwin, 1835) in Chile have been mystified by the booming sounds of the desert. Sustained booming is defined as the continuous, loud droning sound emitted from a large sand dune after inducing a sand avalanche on its leeward face (Criswell *et al.*, 1975; Lindsay *et al.*, 1976). An avalanche of sand can be initiated naturally when sand exceeds its angle of repose or can be induced by a manmade slide. Booming is a seasonal phenomenon and investigators (Haff, 1986; Lewis,

1936) have noted that moisture in the sand can eliminate the booming sound completely. The booming sound differs fundamentally from the "squeaking" sound on sand beaches at frequencies around 1000 Hz (Humphries, 1966; Nori *et al.*, 1997; Sholtz *et al.*, 1997) and from "burping" sounds when sand is shaken back and forth in a jar (Goldsack *et al.*, 1998; Haff, 1979). These burping sounds consist of short ($t < 0.25$ s) bursts at frequencies (150-300 Hz) higher than booming sounds and with different spectral characteristics.

An explanation for the booming sound is found in Poynting and Thompson (1909) classic 1909 physics textbook, proposing that the frequency is related inversely to the time required to pass between successive collisions of individual grains. Bagnold (1954) provides a similar argument based on shearing and dilation, and finds that the frequency should vary as $(g/D)^{1/2}$, where g is the acceleration due to gravity and D is the average particle diameter. More recently, Andreotti (2004); Bonneau *et al.* (2007); Douady *et al.* (2006) support the $(g/D)^{1/2}$ scaling and argue that the frequency is controlled by the shear rate inside the avalanche. The dependence on granular properties alone suggests that booming should occur on all dunes, in contradiction to observations. The current work presents new experimental evidence that support an alternative interpretation of the booming based on a resonating waveguide. This waveguide model explains why the booming phenomena only occur in certain locations and at certain times of the year. It also provides an explanation for the continuation of booming for up to a minute when all visible shearing has ceased (auxiliary material Animation S1).

3.2 Method

At Dumont Dunes, just south of Death Valley National Park, California, USA, measurements of the booming frequencies were made at two dunes on 11 and 12 September 2006. The elevation above the desert floor was approximately 45 m and 11 m for the large and small dune respectively. Both dunes had a slip face near the crest at an inclination of 30°. To initiate the booming sounds, human sliders descended the steep face at a constant speed of 1.1 m/s, creating a slide in the surrounding sand. Figure 3.1 shows the free-surface profiles of the large and small Dumont dune.

Figure 3.2 presents recordings of the sustained booming frequency created during the slide, measured with a microphone at location B (auxiliary material Audio S3) and with an

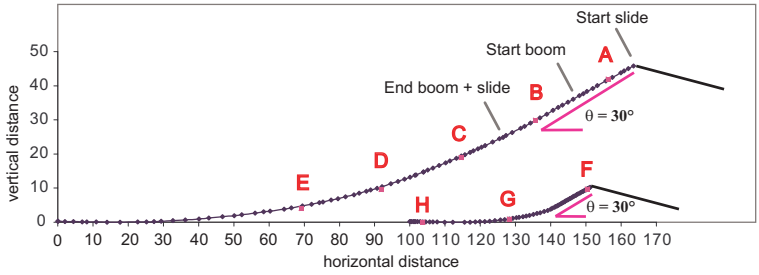

Figure 3.1: Free-surface profiles and seismic set up on the large and small Dumont dune. The geophones are separated 1 meter apart and positioned on the large dune (h = 45 m, 96 geophones) in two deployments from A to E and on the small dune (h = 11 m, 48 geophones) in one deployment from F to H. The pressure impulses are provided by striking a plate with a sledgehammer at locations A-H. Both dunes have a slipface near the crest at an angle of repose of 30 degrees.

array of seismic geophones positioned downhill from location A. The sound did not start immediately, varied somewhat during the slide and showed one dominant frequency with several higher harmonics (figure 3.2a). The largest amplitude measured by the geophone signal was obtained around location B (figure 3.2c). The booming sound diminished and disappeared as the sliders descended farther down the dune where the surface slope lessened. Visible surface avalanching occurred during the slide on the smaller dune (figure 3.2f), but booming could not be initiated resulting in a broadband emission at low magnitude. When the experiment was repeated on the larger Dumont Dune in the winter on 5 December 2006 (not shown here), no sustained booming could be initiated, although faint, short squeaks were audible during the slide. These squeaks had a lower frequency (∼65 Hz), a shorter duration (∼0.2 seconds) and lower amplitude than the booming emission. The definition of sustained booming sound does not apply here as the acoustic emission is short and not sustained.

Over the course of 5 summers, visits were made to Dumont Dunes and to 3 other booming locations: Big Dune near Beatty, NV; Eureka Dunes in Death Valley National Park, CA; and Kelso Dunes in Mojave National Preserve, CA. At each location the dune had a clear slip face below the crest at the angle of repose of the sand. The sustained booming frequency was measured with either a microphone or with a single geophone during an induced avalanche of sand. Booming could never be initiated on faces that were below the angle of repose.

Sand obtained at each location was sieved in the laboratory to determine the average grain diameter and its standard deviation. The average grain diameter ranges from 0.18

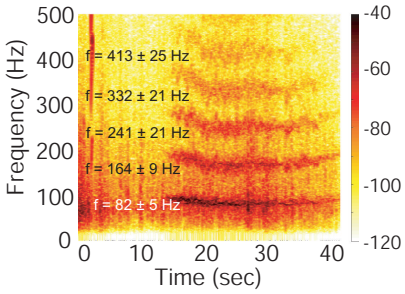

(a) Microphone at station B, 33 meters from the crest of the large dune.

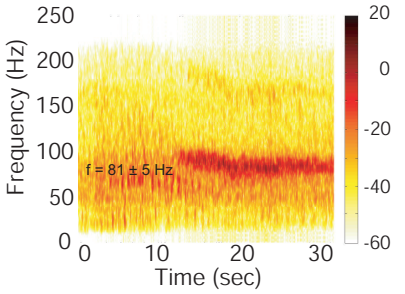

(b) Geophone at station A, 8 meters from the crest of the large dune.

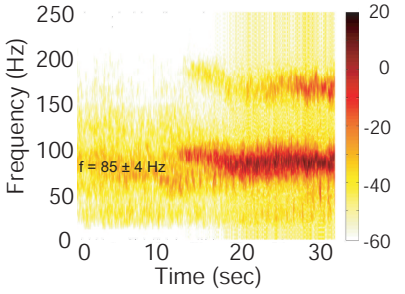

(c) Geophone at station B, 32 meters from the crest of the large dune.

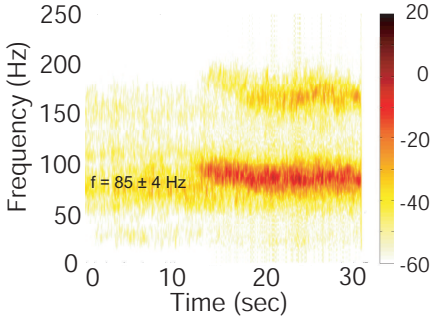

(d) Geophone at station C, 56 meters from the crest of the large dune.

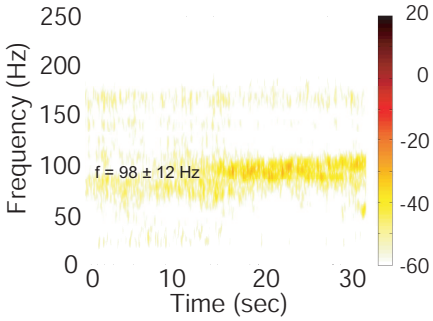

(e) Geophone at station E, 104 meters from the crest of the large dune.

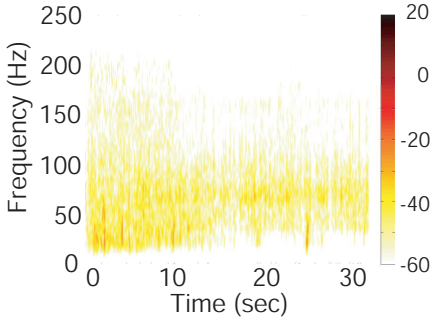

(f) Geophone at station F, 0 meters from the crest of the small dune.

Figure 3.2: The booming sound. Spectrograms of microphone and geophone recordings of a booming avalanche–the change in amplitude and sustained dominant frequency down the dune has been illustrated from figure 2b near the top to figure 2e near the bottom. The slide on the small dune produces broadband noise and a three orders of magnitude lower magnitude of the recording–no audible squeaks or sustained booming sound were heard.

to 0.31 mm. Compared with other sands, dune sand is well sorted with a relatively small standard deviation because of its aeolian history (Humphries, 1966; Lindsay *et al.*, 1976). The sustained booming frequency is presented in figure 3.3 as a function of the average grain

size and does not correlate with the particle diameter.

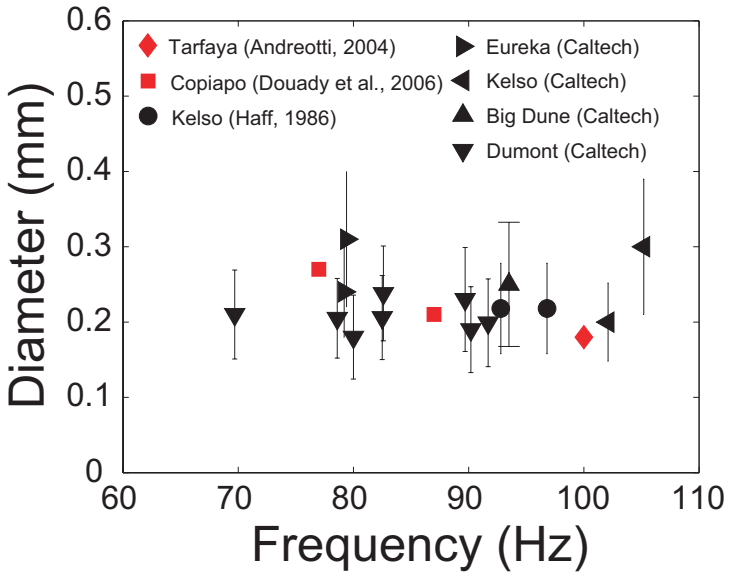

Figure 3.3: Sustained booming frequency f as a function of average grain size diameter D. Data is derived from the work of previous investigators (Andreotti, 2004; Douady *et al.*, 2006; Haff, 1986) and from four different locations visited during the current research. Sustained booming frequency does not correlate with particle diameter. The bar on the diameter represents the standard deviation.

In addition to the booming frequencies, the geophones were used to determine the body wave velocities within the dune using a seismic refraction survey technique. An array of 96 geophones was positioned, beginning 8 m from the crest (location A), with a spacing of 1 meter. The geophones recorded the wave propagation initiated by the striking of a plate with a sledgehammer, as exemplified in figure 3.4 for an impulse at A.

3.3 Results

The seismic records are particularly clean as the surface waves, which propagate at a speed of approximately 50 m/s, are strongly attenuated. By analyzing the slopes in figure 3.4, discrete velocity layering is apparent in this summer recording, while the velocity gradually increases without distinct layers for the same dune in winter. The first arriving body waves for the large (shots A-E) and the small (shots F-H) dune at Dumont are used to determine the subsurface velocity distribution. The large dune (figure 3.5a) has a large lateral velocity gradient and contains a low velocity layer to a depth of 1.5 meters that acts as a waveguide

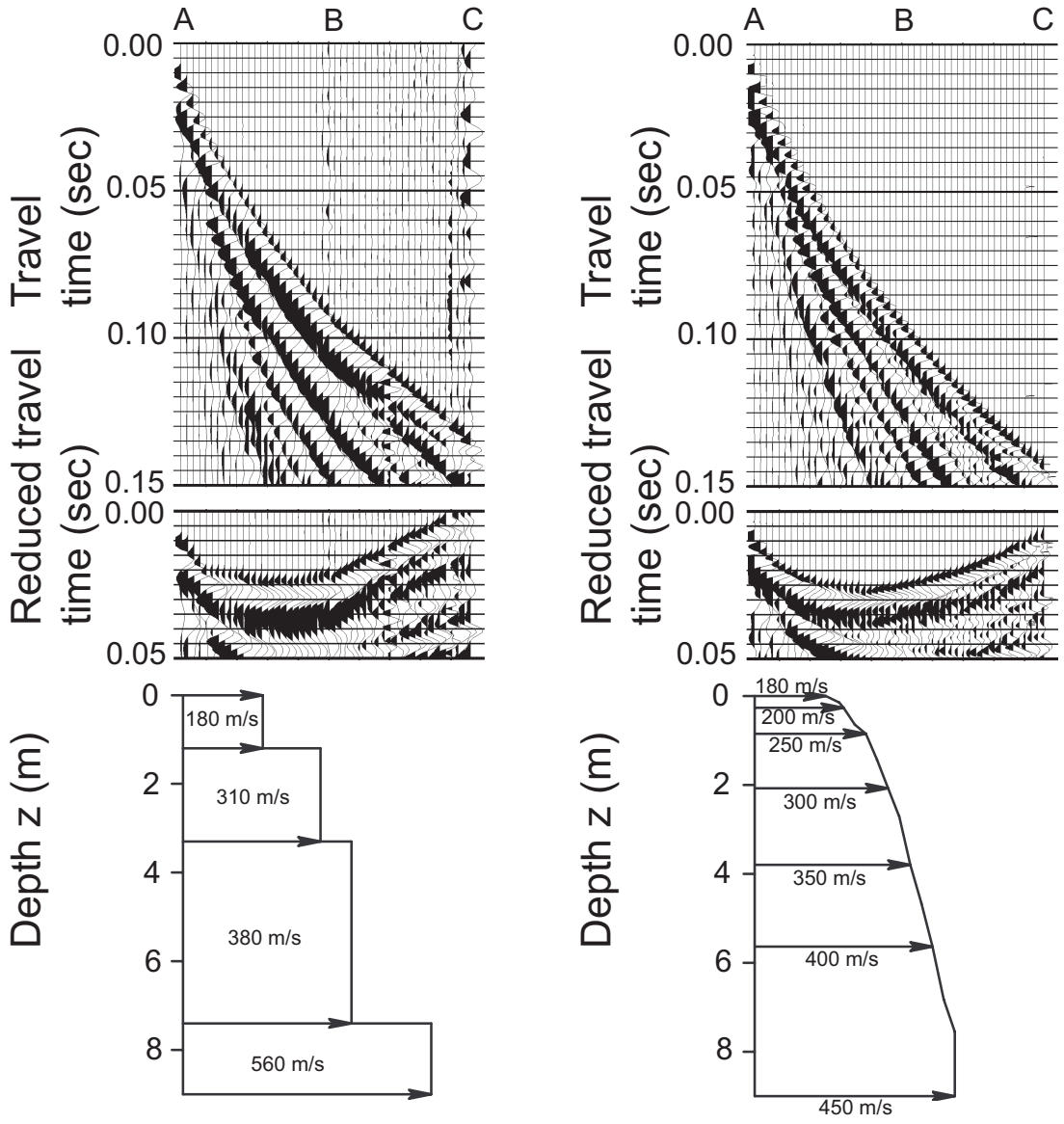

(a) Seismic survey on 12 September 2006

(b) Seismic survey on 5 December 2006

Figure 3.4: Evidence for the change of a dune structure with seasons. The top panel shows the seismograph resulting from a pressure impulse, the seismograph in the middle panel is reduced by a velocity of 350 m/s and the bottom panel shows the resultant velocity structure. The September data points out a discrete velocity layering whereas the December data indicates a continuous velocity variation.

for acoustic energy. On the small dune (figure 3.5b) the surficial velocities are similar in magnitude; however, the layering is less apparent and the first refraction velocity, 600 m/s, is higher, presumably because of the limited height of the dune and the relative proximity

of the desert floor.

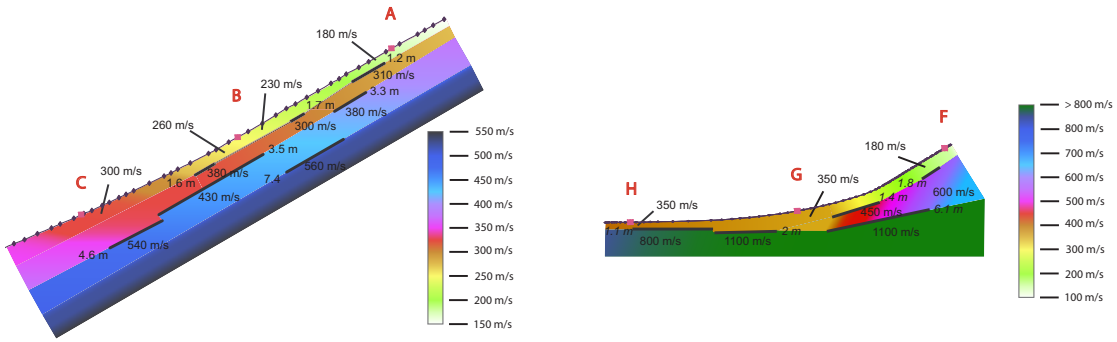

(a) Velocity structure of large dune on 12 September 2006

(b) Velocity structure of small dune on 11 September 2006

Figure 3.5: Structure of the large and small Dumont dune. (a) The large Dumont Dune (45 m high) shows a distinct low velocity layer between point A and B where the booming is clearly evident. The velocity increases strongly downhill (from 180 to 300 m/s). Around point C, the shallow layering disappears completely. (b) The small Dumont Dune (11 m high) has a much shorter channel in longitudinal direction with a high deeper velocity influenced by the desert floor. The figures are to scale and plotted on topographic profiles with measured velocities and depths of interfaces, while the colors are added for interpretation.

As suggested by Andreotti (2004), the wave velocities can also increase due to hydrostatic pressure within the dune. The standard scaling between velocity and pressure in granular materials states that $c \sim P^{1/6}$. This relation predicts a 16% increase in velocity at a depth of 10 m for sand with a density of 1500 kg/m^3, compared to a 250% increase observed in the data. Hence, the velocity increase is not explained by a simple increase due to hydrostatic pressure. The jumps in velocity cannot be explained by pressure increases and are instead a result of structural differences. These structural changes are due to a local high water content or chemically altered sand. Andreotti only considers low speed surface waves of around 50 m/s as the speed of the booming sound. By cross-correlating the geophone signals, the phase speed of booming is measured at 200 m/s near the crest of the dune and increasing to 350 m/s further downhill. Hence, booming results from the propagation of body waves not surface waves.

The dune can act as a seismic waveguide (Ewing *et al.*, 1957; Officer, 1958) because of the subsurface layering. The avalanching of the surface layer acts as its moving source of energy. Waves propagating at c1 in the surficial layer are reflected at the atmospheric

boundary and the substrate half space. The surficial layer of thickness H is sandwiched between the higher velocity atmosphere (c_0) and substrate half space (c_2). For the frequency f_n associated with mode n (where n=1, 2, 3,...) for which the phase difference between two subsequent descending waves is an integral number of 2π, wavefronts interfere constructively when:

$$4\pi H cos(\phi)\frac{f_n}{c_1} - \epsilon_{10} - \epsilon_{12} = 2(n-1)\pi. \tag{3.1}$$

For the special case of incidence at the critical angle $\phi = \phi_{cr}$ the phase changes ϵ_{10} and ϵ_{12}, as defined by Officer (1958), are zero. No attenuation occurs in either the atmosphere, or the substrate half space, resulting in the maximum excitation of the waveguide. For the condition where the velocities c_0 and c_2 are equal, the amplitude of the booming is at its maximum magnitude as experimentally observed in figures 3.2b-e and figure 3.5a. The frequency is computed as:

$$f_n = \frac{nc_1}{2H\left[1 - (\frac{c_1}{c_2})^2\right]^{1/2}}. \tag{3.2}$$

Since the velocity c_0 is larger than the surficial velocity c_1, successive wave trains will reinforce each other resulting in a coupling for the horizontal transmission between the waveguide and the upper medium. In practice, not all waves travel at the critical angle and some loss of energy will occur at the interface. The frequency predicted by equation (3.2) is compared with experimental results from the July, August and September 2006 data at Dumont Dunes (table 3.1). For the 3 different dates, the agreement between the measurement and the calculated frequency is closest in the upper region of the dune where the maximum amplitude of the booming sound occurs and where the air velocity matches the substrate half space as assumed by equation (3.2). The booming sound cannot be generated where the velocity of the surficial layer of the dune approaches or exceeds the velocity of the air. The observed harmonics are explained by analyzing higher modes of the resonance at n = 2, 3,...

The effect of the avalanche speed was investigated by comparing two slides produced at different sliding speeds of $V_s \approx 1$ m/s (auxiliary material Animation S3) and $V_s \approx 2$ m/s (auxiliary material Animation S4) in August 2006. The slides occurred on two neighboring sections of the dune approximately 15 meters apart laterally. The frequency of the sustained sound was essentially the same: 83 $\pm$ 8 Hz for the slow slide (auxiliary material Audio S1)

Table 3.1: Comparison of the calculated and the measured frequencies on the large Dumont dune on 14 July, 22 August and 12 September 2006.

Date and location	c_0	$c_1 \pm$ δc (m/s)	$c_2 \pm$ δc (m/s)	$H \pm$ δH (m)	$f_1 \pm$ δf_1 (Hz)	$f_m \pm$ δf_m (Hz)	A/A_0
07/14/2006							
shot A	356	260 ± 20	340 ± 30	2.2 ± 0.6	90 ± 30	92 ± 5	–
shot B, up	356	270 ± 20	340 ± 30	2.4 ± 0.6	93 ± 34	92 ± 5	–
shot B, down	356	260 ± 20	380 ± 30	2.5 ± 0.5	71 ± 18	92 ± 5	–
shot C	356	310 ± 30	420 ± 40	3.8 ± 0.9	60 ± 21	92 ± 5	–
08/22/2006							
shot A	355	180 ± 20	300 ± 30	1.2 ± 0.3	94 ± 26	86 ± 5	0.16
shot B, up	355	220 ± 20	300 ± 30	1.6 ± 0.4	101 ± 36	84 ± 8	1
shot B, down	355	250 ± 20	370 ± 30	1.3 ± 0.3	136 ± 41	84 ± 10	0.6
shot C	355	340 ± 30	450 ± 40	3.7 ± 0.9	70 ± 24	82 ± 6	0.14
09/12/2006							
shot A	351	180 ± 20	310 ± 30	1.2 ± 0.3	92 ± 25	81 ± 5	0.30
shot B, up	351	230 ± 20	300 ± 30	1.7 ± 0.5	105 ± 42	83 ± 6	1
shot B, down	351	260 ± 20	380 ± 30	1.6 ± 0.4	111 ± 31	84 ± 4	0.49
shot C	351	300 ± 30	430 ± 40	3.5 ± 0.8	60 ± 18	85 ± 4	0.13

and 87 ± 5 Hz for the fast slide (auxiliary material Audio S2). The sustained tone and its harmonics are not influenced by the speed of the avalanche. However, the slower slide incorporated a greater surface area involved in the avalanche and the amplitude of the acoustic emission was a factor two higher. Hence, the amplitude of the booming increases with the amount of avalanching sand, as displayed for the large slide in auxiliary material Animation S2.

3.4 Conclusion

The avalanching sand acts as a source for the acoustic emission, and the waveguide sets the frequency. Waves interfere constructively and reinforce each other resulting in a loud audible emission. The sand surface interacts with the atmosphere and acts as a loudspeaker by propagating disturbances into the atmosphere. For slopes shallower than 30°, such as on the lower foothill or the windward face, booming could not be initiated. The December experiment on the larger dune demonstrates that a continuous velocity distribution, without apparent layering, does not provide the conditions for sustained booming. Seasonal changes in environmental parameters like temperature, precipitation, irradiation and wind direction

contribute to the variations in subsurface velocities and dune features. Moisture that is not evaporated seeps down into the dune, increasing the velocity and eliminating the layering structure. Smaller dunes lack the required subsurface structure and sufficient length to create the waveguide.

3.5 Acknowledgments

The authors would like to thank the late Ron Scott, Norman Brooks, George Rossman and Tom Heaton for their scientific suggestions and Steve Hostler and Gustavo Joseph for their guidance and help. The help of the undergraduate students Natalie Becerra, Patricio Romano-Pringles, Ransom Williams, Nora DeDontney and the late Steve Gao and many others, was essential during the field experiments at various locations. Travel and equipment support for N. M. V. was provided through funding from the Pieter Langerhuizen Lambertuszoon Fonds.

3.6 Auxiliary Material

Auxiliary material for this article contain the frequency with errors in a table and audio and movie files of several booming events.

Table 3.2: Error on the frequencies determined from the half width used in the comparison between the frequency and average diameter in figure 3.3.

Location	Date	f_{peak} (Hz)	$f_{\text{half,min}}$ (Hz)	$f_{\text{half,max}}$ (Hz)
Eureka	07/18/2002	79.4	74	84
	07/18/2002	79.2	76	82
Kelso	07/30/2002	102.1	92	106.5
	07/30/2002	105.2	102.5	109.5
Big Dune	08/21/2002	93.5	87	96.5
Dumont	08/21/2002	89.7	82	94
	09/19/2003	77.1	74	82
	07/23/2004	90.2	83.5	93
	07/12/2005	69.7	56.5	84.5
	09/08/2005	78.6	75	84.5
	07/14/2006	91.7	87	94
	08/22/2006	83.3	80	88.5
	09/12/2006	84.8	81	86.5

The auxiliary material included sound and movie files:

- Movie S1. Movie of Kelso Dunes for the July 2002 sliding event. This movie shows sustained booming after the sliding itself stops.
- Movie S2. Movie of Dumont Dunes for the May 2006 sliding event. This movie shows a massive booming slide by 12 people at the same time.
- Movie S3. Movie of Dumont Dunes for the August 2006 sliding event. This movie shows a slow booming slide with a sliding speed at approximately V = 1 m/s.
- Movie S4. Movie of Dumont Dunes for the August 2006 sliding event. This movie shows a fast booming slide with a sliding speed at approximately V = 2 m/s.
- Audio S1. Audio of Dumont Dunes for the August 2006 sliding event. This high quality audio recording captured the emission of a slow booming slide with a sliding speed at approximately V = 1 m/s.
- Audio S2. Audio of Dumont Dunes for the August 2006 sliding event. This high quality audio recording captured the emission of a fast booming slide with a sliding speed at approximately V = 2 m/s.
- Audio S3. Audio of Dumont Dunes for the September 2006 sliding event. This high quality audio recording captured the emission of a booming slide.

Chapter 4

Reply to Comment by B. Andreotti et al. on "Solving the Mystery of Booming Sand Dunes"

This reply addresses three main issues raised in the comment of Andreotti *et al.* (2008). First, the turning of ray paths in a granular material does not preclude the propagation of body waves and the resonance condition described in Vriend *et al.* (2007). The waveguide model still holds in the dune for the observed velocities, even with a velocity increase with depth as implied by Andreotti *et al.* (2008). Second, the method of initiation of spontaneous avalanching does not influence the booming frequency. The frequency is independent of the source once sustained booming starts; it depends on the subsurface structure of the dune. Third, if all data points from Vriend *et al.* (2007) are included in the analysis (and not an average or selection), no correlation is observed between the sustained booming frequency and average particle diameter.

4.1 Curved Ray Paths and the Existence of a Resonance Condition

Andreotti *et al.* (2008) claim that for granular media, the body waves are non-existent near the surface. The basis of this claim is that the velocity increases with depth in a granular material. The ray paths of acoustic waves will bend toward the surface and the bending depends on the velocity gradient and the angle of incidence.

The velocity increase with depth in a granular material is often modeled (Jia *et al.*, 1999) as $c \sim Az^{\alpha}$, with $\alpha = 1/4$ for low confining pressure and $\alpha = 1/6$ for high confining

pressure. The proportionality constant A determines the magnitude of the velocity increase and hence the turning of the ray paths. Andreotti *et al.* (2008) state that the velocity in sand typically increases between $\alpha = 1/3$ and $\alpha = 1/4$, but do not give any numerical value of A.

The near-surface structure of Dumont Dunes for the seismograph of 09/12/2006 displayed a constant velocity with a sharp jump in seismic velocity at a subsurface interface, as presented in figure 4a in Vriend *et al.* (2007). This detail is reiterated in figure 4.1a with the first arrival picks highlighted in red. For the resonance condition it is not essential that the velocity is constant with depth. A gradual gradient with depth will produce essentially the same result. To illustrate, a small linear gradient is added to the top layer for which an analytic solution exists (Slotnick, 1959). The resonance ray path is shown in figure 4.1b.

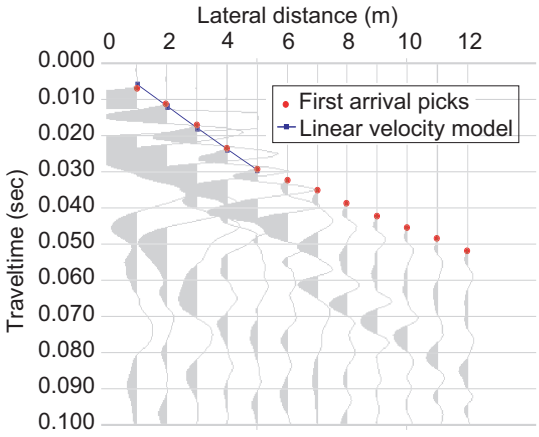

(a) Detail of the seismograph of the seismic refraction experiment.

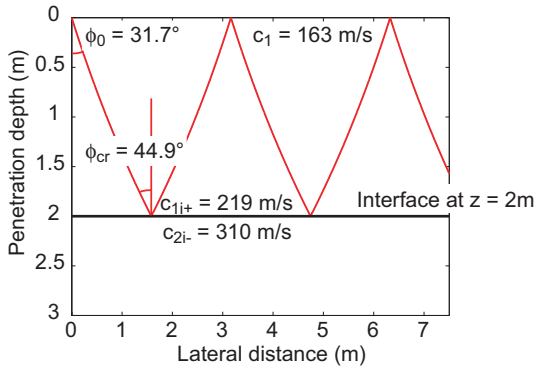

(b) Ray path for a linear velocity increase with angle of emergence $\phi_0 = 31.7°$ and critical angle $\phi_{cr} = 44.9°$.

Figure 4.1: Effect of linear increase in velocity in the upper layer on the waveguide model. The picks of the first arrivals are indicated in red points and show a constant velocity in the surficial layer. The blue line shows the velocity picks if the velocity would be modeled as a linear velocity increase $c(z) = c_0 + kz$, with $c_0 = 163$ m/s and $k = 28$ m/s/m as determined from the best fit of the travel time curve. Although the wave is slightly curved, resonance and constructive interference still occurs. Constructive interference is strongest for waves impacting on the interface at the critical angle (Vriend *et al.*, 2007).

Another point of clarification is our use of the seismic refraction survey, a standard procedure executed in geophysical research. The method determines the velocity from the travel time of the first arrival wave, but is not related to the resonant frequency of spontaneous booming. The hammer blow is simply the source for the refraction survey and is not in-

tended to (and does not) initiate booming. In a second set of measurements, the resonance frequency of the sustained booming after the creating of an avalanche was measured with an array of geophones. By applying cross-correlation on the array, the propagation velocity results to a speed close to the p-wave velocity in sand (~ 250 m/s) and not 50 m/s as given by Andreotti *et al.* (2008). More recent experiments with a 3-component geophone buried at a depth of ≈ 20 cm did not show a significant reduction in amplitude with depth, as described by Andreotti *et al.* (2008). Details of these experiments will be presented in an upcoming paper (Vriend *et al.*, 2010b).

4.2 Relation between the Resonance Frequency and the Method of Initiation

The creation of an avalanche on the leeward face of a dune creates the shearing motion to induce the so-called burping effect–pulselike, short bursts of sound. This sound is due to shearing of well-rounded and smooth sand grains (Haff, 1979) and can be reproduced in the lab by shaking a sand-filled jar. However, when this shaking motion ceases (and hence the shear), the sound stops abruptly as well. For a booming emission, the sound is amplified and sustained, up to a minute after the sliding stops and no shearing of sand is visible (Animation S1 in Vriend *et al.* (2007)). For this type of sound generation, the well-rounded and smooth sand may be necessary, but the required sub-surface structure is essential to the amplification and resonance of the booming sound. In the wintertime, the same sand is present and short bursts can be created, but the sustained booming sound is not present (figure 2f in Vriend *et al.* (2007)). This result is because of the change in sub-surface structure, possibly due to water saturation of the upper layer of the dune. Field measurements of the frequency and propagation velocity of the booming and burping emission indicate a fundamental difference between these two phenomenon (Vriend *et al.*, 2010b).

Direct measurements of the method of source initiation have been executed by inducing slides at two different speeds. Spectrograms of high quality audio recordings of the sustained booming in table S1 in the auxiliary material show the same frequency. Our experience from comparing natural to man-made avalanches is that the method of initiation does not influence the frequency, only the amplitude.

Andreotti *et al.* (2008) also state that the booming frequency is constant for different

flow thicknesses, at different places and different weather conditions. In the past summer, our group recorded natural (wind-induced) avalanches on 05/29/2007 and 09/17/2007 at the same location. The recordings of these natural avalanches showed a 20 Hertz difference in sustained booming frequency, while the subsurface structure showed a quantitative difference for these two cases from ground penetrating radar images (Vriend *et al.*, 2010a). This is a direct contradiction to observation of Andreotti *et al.* (2008) that the frequency is constant for one location.

4.3 Variation of Resonance Frequency with Grain Size

The data shown in figure 2c in Andreotti *et al.* (2008) is a subset of the many data points that were shown by Vriend *et al.* (2007), which were taken in different seasons spanning several years. A range of frequencies were measured and therefore these data points should not be averaged. The figure with all data points is redrawn in figure 4.2a. The size distributions were measured from samples taken on the leeward face where the avalanche was recorded. On a given field date, the sustained booming frequency remains constant on a given section of the dune, and is independent of the mechanism of initiation of the avalanche.

Andreotti *et al.* (2008) claim that the data points in table S1 were obtained in situations for which (i) avalanches where spontaneous or at least homogeneous and steady (ii) the grain diameter was determined from samples taken in the middle of the slip face. This statement is not consistent for the data obtained by Haff (1979) and Lindsay *et al.* (1976). Furthermore, the data in table S1 contains discrepancies with values found in the literature.

Haff (1979) measured at Kelso Dunes two different frequencies (f = 92.8 Hz and f = 96.8 Hz), which were obtained by "forcing oneself vigorously downhill by action of the hands and feet." Using Haff's fractional distribution of grain sizes, 0.22 ± 0.06 mm was obtained, not the 0.200 mm as quoted by Andreotti *et al.* (2008). The Sand Mountain data point (61 Hz for the microphone and 66 Hz for the geophone) collected by Lindsay *et al.* (1976), was obtained by "shoveling in the sand approximately three meters from the geophone that was buried just below the dune surface." Furthermore, "26 sand samples were collected at regular intervals of approximately 24 m." The mean grain size ranged from 0.256 mm to 0.384 mm. It is unclear why Andreotti *et al.* (2008) in table S1 selected 0.340 mm to report as the average grain diameter for these measurements.

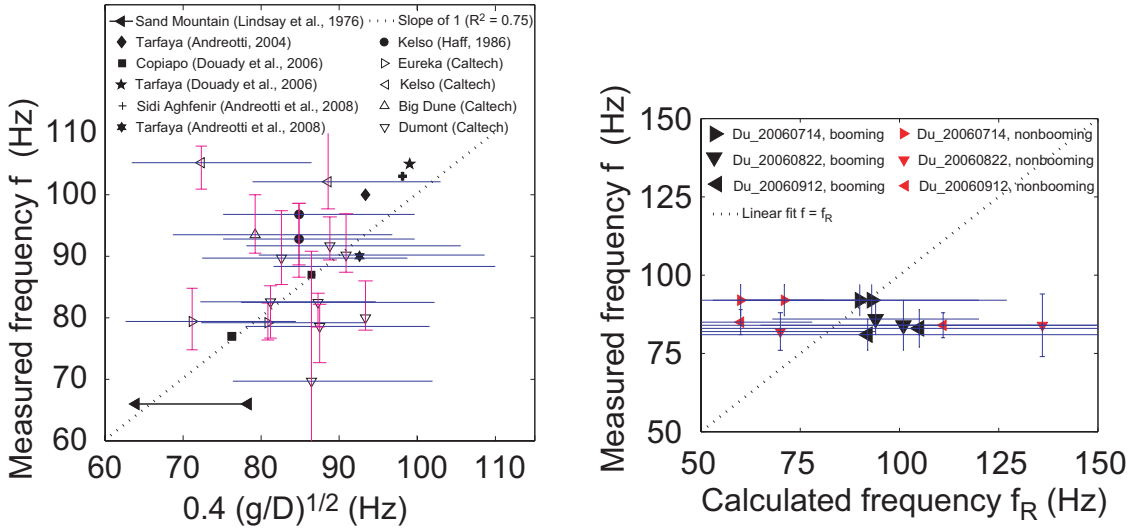

(a) Booming frequency as a function of $0.4\sqrt{g/D}$

(b) Booming frequency as a function of the resonance frequency

Figure 4.2: No correlation between booming frequency and average particle diameter can be established by analyzing the entire data set. The large uncertainty on the calculated frequency is due to a large uncertainty in depth of the waveguide channel. The data points published by Andreotti *et al.* (2008) and Douady *et al.* (2006) did not contain uncertainties on the diameter. For the booming locations, the resonance frequency f_R follows the calculated frequency reasonable well. The black symbols indicate a locally initiated booming emission, while booming could not be locally initiated for the red symbols. For these cases, the frequency was measured while the avalanche occurred higher up at the dune.

In table S1 Andreotti *et al.* (2008) report a frequency of 90 Hz and an average diameter of 183 mm for Tarfaya. This data differs from the frequency 105 ± 10 Hz and grain size 0.160 mm reported in Douady *et al.* (2006) and 100 ± 5 Hz and 0.180 mm as reported in Andreotti (2004). This indicates a significant change in frequency for the same location. Furthermore, the data point for "El Cerro Bramador" was reported to be at a frequency of 77 Hz in Douady *et al.* (2006), not 75 Hz.

The calculated resonance frequencies from table 1 in Vriend *et al.* (2007), were characterized by a large uncertainty in the frequency as a result of the uncertainty in the depth of the waveguide. In figure 4.2b, the error bars on the calculated resonant frequency are added and booming and nonbooming locations are distinguished in black and red symbols respectively. Ground penetrating radar surveys executed in the summer of 2007 give a better estimate of the waveguide depth which determines the bound on the resonance frequencies (Vriend *et al.*, 2010a).

4.4 Auxiliary Material

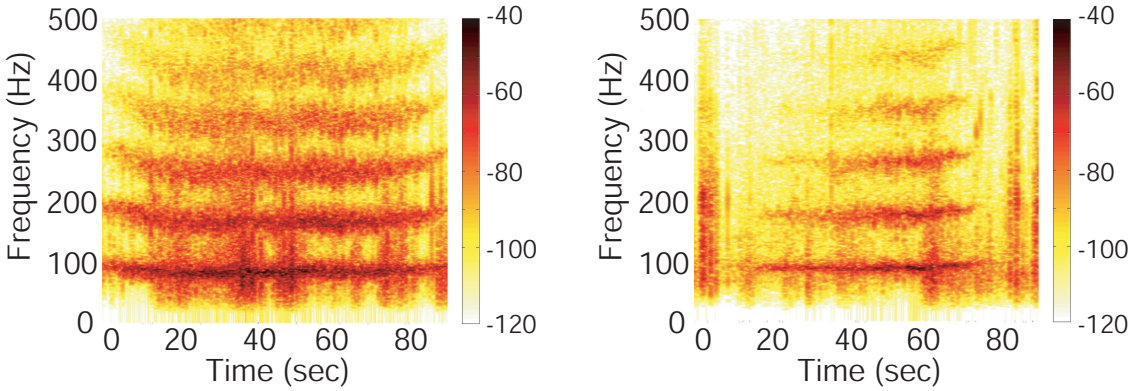

(a) slow slide ($V \approx 1$ m/s).

(b) fast slide ($V \approx 2$ m/s).

Figure 4.3: Spectrograms of the man-made avalanche on the leeward face of the tall Dumont Dune (45 m high). The method of exciting of an avalanche does not have an influence on the frequency of the emission once sustained booming starts. The magnitude of the booming is larger for the slow slide, as more sand is displaced and hence a larger source area is created.

Chapter 5

Linear and Nonlinear Wave Propagation in Booming Sand Dunes

The current study presents measurements of wave propagation in a booming sand dune. The booming is an audible loud rumbling sound that may occur after a sand avalanche initiates on a slip face of a large desert dune. The emission consists of one dominant frequency (70-105 Hz) with several higher harmonics. The source of the sound results from shearing of sand grains that produce short squeaks of sound known as burping. The sound waves are amplified by resonance in a near-surface layer. Geophone measurements of the wave propagation through the sand in the dune contain both surface and body waves. This paper demonstrates that booming is due to the trapping of the body waves in the surficial layer; the burping is associated with surface waves.

5.1 Introduction

Booming sand dunes (Hunt and Vriend, 2010; Lindsay *et al.*, 1976) generate a sustained rumbling emission (70-100 Hz) after the creation of a sand avalanche on a slope at the angle of repose. The booming sound may continue for up to several minutes and resembles a low-flying propeller airplane. This emission occurs most frequently in the hot and dry summer months. In the wetter season, the in situ sustained booming is difficult to create. The variability throughout seasons suggests that environmental factors independent of the sand properties determine whether booming can occur (Nori *et al.*, 1997).

The direct shearing of smooth and well-rounded sand in situ produces so-called burping sounds. These pulselike, short bursts of sound (Haff, 1979) are created when direct shearing

is applied on a sample of booming sand. This shearing may occur in situ by moving a hand or shovel (Criswell *et al.*, 1975) quickly along the dune surface, or in the laboratory by shearing sand in a confined geometry (Douady *et al.*, 2006). Douady *et al.* (2006) observed that the frequency of burping depends on the shear rate and the particle diameter of the sample. The pulses generated in situ are short (< 0.25 sec) and have a broad frequency content, usually between 50 and 70 Hz. However, short pulses have been recorded for frequencies as low as 30 Hz and as high as 130 Hz.

The type of waves responsible for the acoustic emission on dunes forms the subject of a lively debate in literature (Andreotti, 2004; Andreotti *et al.*, 2008; Bonneau *et al.*, 2007; Vriend *et al.*, 2007, 2008). Andreotti's theory is based on the propagation of the booming sound as a surface wave phenomenon in the upper centimeters of the sand dune. Using two sensors and an external excitation, the author measured the dispersive properties of a wave with phase speed of approximately 40 m/s. In an active avalanche experiment, these two sensors measured a near-surface, elliptical polarized vibration and a wavelength of 42 cm. Using an array of 48 sensors, Vriend *et al.* (2007) measured a non-dispersive wave with a speed of approximately 230 m/s. The analysis presented in Vriend *et al.* (2007) explained the sound amplification through constructive interference of a compressive P-wave within a natural waveguide within the upper 2 m of the dune.

The current paper presents additional measurements of wave propagation in a booming dune, which were not included in the papers by Vriend *et al.* (2007) and Vriend *et al.* (2008). In addition, it provides an explanation for the difference between the results described herein and the earlier work by Bonneau *et al.* (2007) and Andreotti (2004). Because these researchers measured the sound only with two sensors, they were not able to capture the complete wave propagation characteristics of both the booming and burping emission in situ. This paper explains the controversy on the origin of booming sound by demonstrating the distinction between the character of the booming and burping emissions.

In the present study, the wave propagation in the dune is initiated by three different methods–a pressure impulse, direct local shearing, and the creation of a regional sand avalanche. The difference in propagation speed and frequency content between booming and burping indicates that the wave characteristics of the two emissions are fundamentally different. Rayleigh surface waves and compressive P-waves are present during both the local shearing and the regional avalanche. However, the fast-traveling, higher frequency P-waves

are the dominant component for the booming sound, while the burping sound generates mainly slow-traveling, lower frequency Rayleigh surface waves.

5.2 Background

The waveguide analysis presented in Vriend *et al.* (2007) explains the sound amplification due to constructive interference of the source. The initial source is the local sound emission produced by shearing the sand grains against each other. The natural waveguide channel within the subsurface structure of the dune amplifies the sound and sets the booming frequency. A surficial layer of dry sand is sandwiched between the air layer and the denser substrate half space, as illustrated in figure 5.1. The waves travel in phase, reinforce each

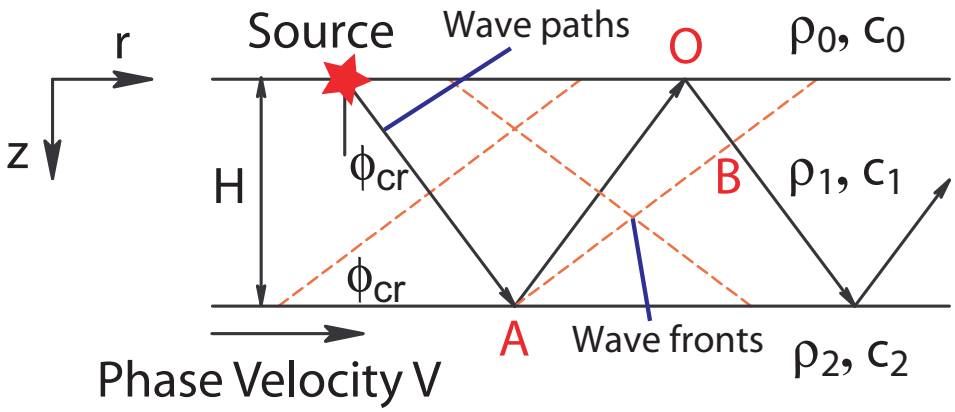

Figure 5.1: Schematic sketch of the natural waveguide inside a booming dune.

other, and produce the loud droning sound known as booming. A rounded and well sorted type of sand is necessary for the initiation of short bursts of sound (Haff, 1979), but the required sub-surface structure is essential for the amplification and resonance of the emission into the booming sound. The natural resonance frequency of the waveguide is given as (Vriend *et al.*, 2007):

$$f_n = \frac{n}{2} \frac{c_1}{H\sqrt{1 - \left(\frac{c_1}{c_2}\right)^2}}, \tag{5.1}$$

The dimension of the waveguide H and the speed of sound in the sand layers c_1 and c_2 prescribe the booming frequency and its higher harmonics $n = 1, 2, 3, ...$ directly. Therefore, the variation in booming frequency between seasons comes directly from these physical

parameters and does not depend on how the avalanche is initiated. Vriend *et al.* (2008) showed that the avalanche speed did not influence the sustained frequency and its harmonics, but only influenced the amplitude of the emission. Booming does not occur in the winter because the moisture in the top layer increases the speed of sound in the surface layer c_1 such that the cutoff frequency is above the excitation frequency and effectively eliminates the sandwich structure that keeps the energy within the waveguide.

5.3 Source Mechanism

To investigate the characteristics of booming dunes in greater detail, three methods are used to initiate the booming. The first method involves several individuals sliding in unison down the slip face of the dune as shown in figure 5.2a. The second method entails a local shearing of the upper layer of the sand with a hand (figure 5.2b). The third method involves a pressure impulse using a metal plate and mallet as shown in figure 5.2c; this method is also used in the seismic refraction experiments found in Vriend *et al.* (2007).

These source events produce elastic waves that are recorded by vertically oriented uniaxial geophones that measure the ground vibrations. In the first recording set up, illustrated in figure 5.3a, a finely spaced array of 12 vertical geophones, spaced either 0.25 or 1 meter apart, is placed parallel to the crest. This set up records the acoustic emissions as pseudo-plane waves perpendicular to the direction of the moving source. In the alternative set up, shown in figure 5.3b, 48 geophones spaced 1 meter apart are used to investigate the wave speed in downhill direction. The analysis of the geophone signals reveals information about the frequency characteristics of each of the source mechanisms and the wave velocities along the array.

Man-made or naturally induced sand avalanches on a dune slope at the angle of repose may produce the loud booming sounds. A natural avalanche appears if sand, blown over the crest by the wind, deposits beyond the critical angle of repose and starts to slump spontaneously. The booming sound, as shown in figure 5.2d, is sustained and continues for some time even after the motion ceases. The frequency of the sound is a narrow band centered at peak frequencies around 85 Hertz with higher harmonics. A beating pattern is often apparent in the booming signal because of a slight mismatch of resonant frequencies. Booming usually only occurs in the summertime when the sand is very dry.

(a) Creating a sand avalanche by sliding the sand regionally.

(b) Shearing motion of sand grains locally by the movement of a hand.

(c) Pressure impulse due to a hammer impact on an aluminium plate.

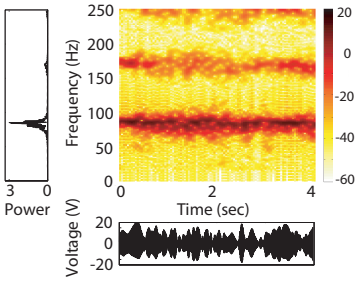

(d) The sustained sound has a narrow frequency banding at 85 Hertz with several higher harmonics.

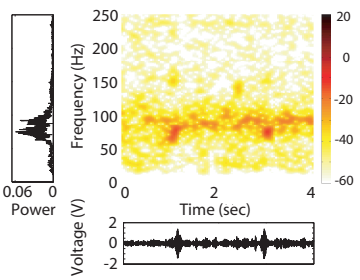

(e) The short bursts of sound have a broad center frequency of 50-60 Hertz.

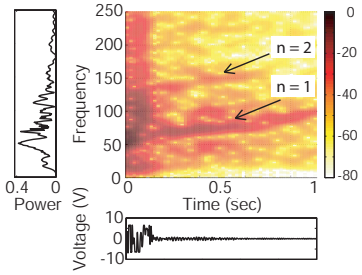

(f) The observed harmonics resulting from the impulse source are a rare occasion.

Figure 5.2: Initiation mechanisms resulting in wave propagation. Spectrogram, signal and power spectrum of the geophone recording created by the different initiation mechanisms at Eureka Dunes on 10/27/2007. The impulse was applied at a "sweet spot" such that the natural frequency of the dune was excited with a pressure impulse instead of a shearing motion.

The direct shearing of sand in figure 5.2e creates pulses in which the amplitude increases and then decreases. The sound stops abruptly when the applied shear ceases and is not sustained. The frequency content of the pulses is broadband and is centered around 60 Hertz. There is also a background signal present with a band around 85 Hertz, but its magnitude is

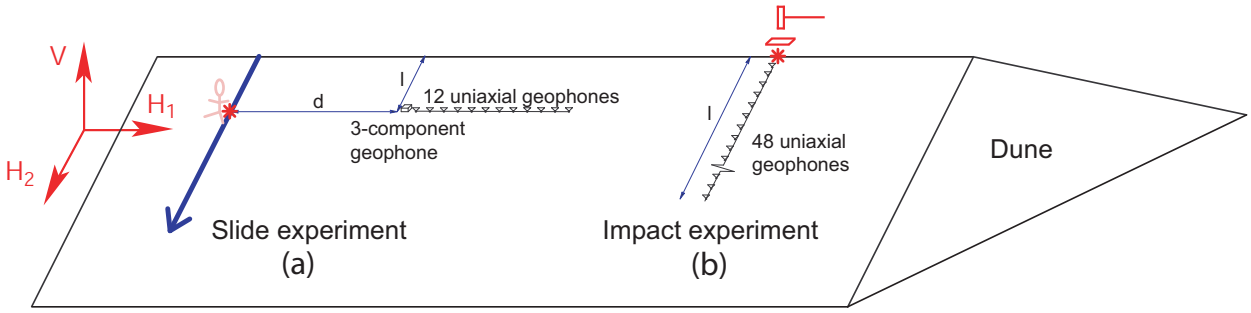

Figure 5.3: (a) Arrangement of geophones for the sliding experiment using 12 uniaxial geophones parallel to the crest with a spacing of 1 m and a three-component geophone at the position of the uniaxial geophone nearest to the source. The geophone array is located at a lateral distance d $\approx$ 5 meter from the source and at a distance l = 12 meters from the crest. (b) Arrangement of geophones for the sliding experiment using 48 uniaxial geophones perpendicular to the crest with a spacing of 1 m for a length of 48 meters.

one order of magnitude lower than the short bursts and two orders of magnitude lower than the loud booming emission observed in figure 5.2d. The frequency of the low magnitude background signal is similar to the frequency measured for the booming sound, indicating that a mechanism amplifies an existing natural dune frequency.

A hammer impact on an aluminium plate placed on the surface of the slip face produces a repeatable pressure impulse. This impulse creates broadband waves with a wide range of frequencies up to 200 Hz. The impulse method does not simulate booming; instead it is a reproducible way to investigate the wave propagation and to measure the wave speed through the sand. On rare occasions, the impact of the hammer, lasting only a tenth of a second, triggers an internal response that lasts up to a second, as shown in figure 5.2f. The frequency response appears as a low magnitude main harmonic with at least one overtone. Direct shearing of sand is not involved in the generation of this response, which increases from 70 to 95 Hertz within a second. This increase in frequency is likely a result of the wave propagation from the source into a region of changing subsurface structure.

5.4 Wave Propagation

5.4.1 Type of Waves

Vriend *et al.* (2007) investigated the compressional seismic velocities of the subsurface struc-

ture of a booming dune using refraction experiments. A standard refractive analysis using the first arrivals revealed a layered structure along the upper part of the dune with a near surface layer of ∼200 ± 20 m/s on top of a faster half space of ∼350 ± 30 m/s. The sharp jump in velocity is due to strong stratigraphical layering. A hydrostatic increase in pressure does not account for the sharp layering observed in the measurements (Vriend *et al.*, 2008). The strong lateral gradient of the seismic velocity in the downhill direction results from the down slope compaction of the sand. Although not discussed in the earlier Vriend *et al.* (2007) work, the shot record shows a refracted body S-wave and a dispersed Rayleigh wave in addition to the compressive P-wave.

Figure 5.4 illustrates the unscaled shot record of a seismic refraction experiment at Dumont Dunes on 05/29/2007. Waves are traveling from the impact source along an array of 48 geophones. The first arrival compressive P-wave has a speed that increases from the start to the end of the line because of the increase in velocity with depth–the waves penetrate deeper into the dune for the farthest sensors. A refractive analysis shows a near surface layer of ∼180 ± 20 m/s on top of a faster half space of ∼300 ± 30 m/s.

The volumetric P-wave travels in radial direction, as a propagating wave, and in depth as a standing wave captured in the waveguide. The trial function ϕ for the expanding wave sandwiched between top and bottom with rigid boundaries is:

$$\phi(r,z,t) = cos(k_z z)e^{i(k_r r-\omega t)}. \tag{5.2}$$

The wave propagates in the horizontal direction with phase velocity $\alpha = \omega/k_r = \sqrt{(\lambda+2\mu)/\rho}$. At the upper boundary, $z = 0$, the boundary condition of zero displacement, $\partial\phi/\partial z = 0$ is satisfied. At the bottom, the rigid boundary condition at $z = H$ with zero displacement is satisfied when $k_z H = n\pi$, with integer n. The equation for the displacement u_z is obtained by applying an energy dissipation term and summing all modes n such that:

$$u_z(r,z,t) = \frac{A}{r}\sum_{n=0}^{\infty} U_n(t)cos\left(\frac{n\pi z}{z_0}\right)e^{-\epsilon r}e^{[i(k_r r-\omega t)]}, \tag{5.3}$$

with forcing function $U_n(t)$, constant A and absorption coefficient ϵ. The energy of the first arrival P-wave spreads in a three-dimensional fashion in the neighborhood of the source.

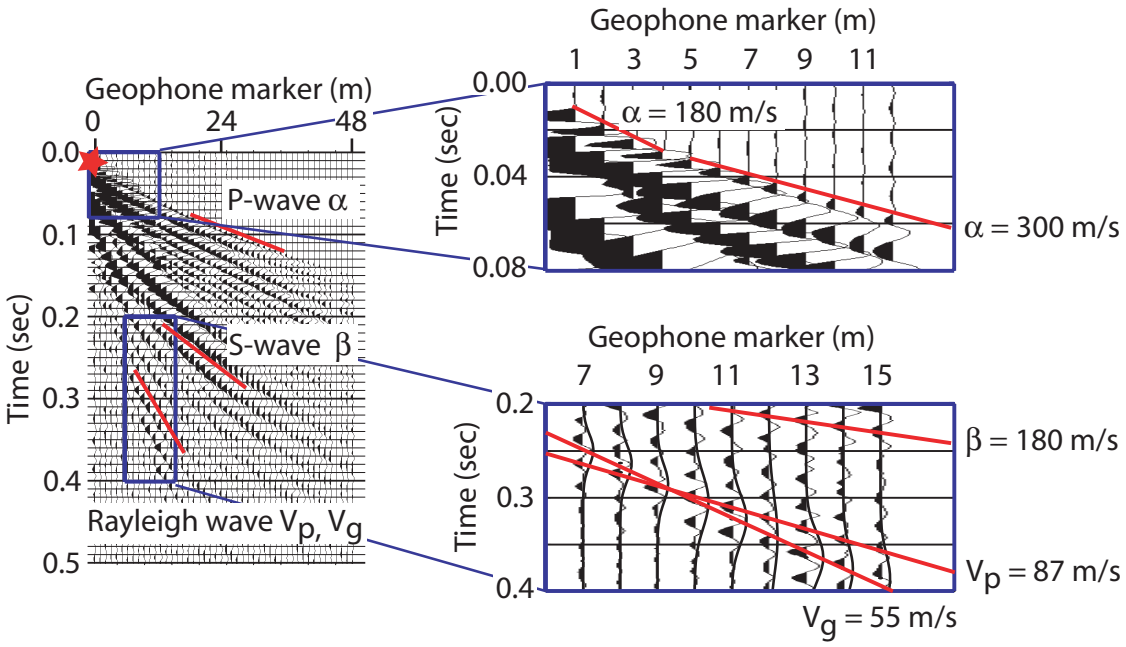

(a)

Figure 5.4: Shot record of the seismic refraction experiment of the Dumont Dune on 05/29/2007. The first insert shows the first arrival P-waves with internal refractions resulting in distinct breaks in the slope. The second insert illustrates the space-time diagram of the Rayleigh wave propagation. The Rayleigh wave is the latest arrival in time in the seismic refraction experiment.

The amplitude trend is inversely related to the distance to the source $\sim 1/r$ and measured in situ for an impulse source in figure 5.5. Because of this volumetric spreading, the first arrival waves are compressive P-waves.

The shear S-wave travels as a second fastest wave packet after the P-wave. The S-waves show internal refractions on the shot record due to distinct jumps in velocity with depth, similar to the refractions of the P-waves. The slowest direct S-wave travels at a speed of β = 130 m/s, resulting in a velocity ratio of $\beta/\alpha = 70\%$ in dune sand. This ratio of a granular material is higher than typical earth materials, modeled as a Poisson solid (Lay and Wallace, 1995), which have a ratio of $\beta/\alpha = 58\%$. The experiment uses vertical seismometers; thereby only records the vertical component of the SV wave and does not detect the horizontal SH waves.

The slowest wave is the dispersed Rayleigh surface wave, which has been identified by Bonneau *et al.* (2007) as the main wave propagating the booming emission. The Rayleigh

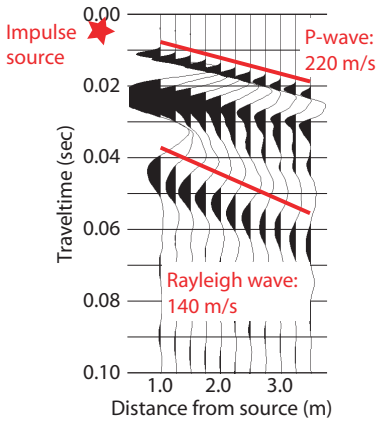

(a) The body P-wave travels at a propagation velocity of $\alpha = 220$ m/s, while the surface Rayleigh wave travels slower at $V_p = 140$ m/s.

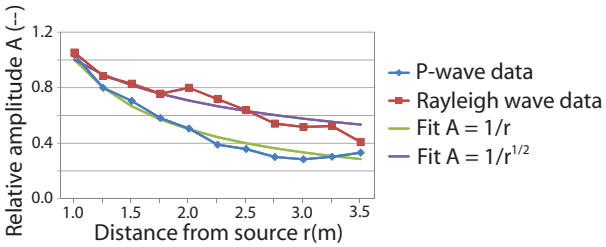

(b) Normalized P-wave and Rayleigh wave amplitude as a function of the distance to the source r.

Figure 5.5: Investigation of type of waves generated by a pressure impulse on 06/01/2008 at Dumont Dunes with a finely spaced (0.25 m) geophone array.

wave is most pronounced for geophones seven through sixteen within the time interval of 0.2-0.4 seconds in figure 5.4. The Rayleigh wave is a surface wave and is confined to the upper part of the dune with trial function $\phi(r, z, t)$:

$$\phi(r, z, t) = e^{-k_z z} e^{i(k_r r - \omega t)}. \tag{5.4}$$

The energy of a surface Rayleigh wave spreads in a two-dimensional fashion with an exponential decay with depth. The amplitude trend is inversely related to the square root of the distance to the source $1/\sqrt{r}$ and is measured in situ for an impulse source in figure 5.5. Because of the surface wave character in cylindrical coordinates, the displacement u_z has a $1/\sqrt{r}$-trend:

$$u_z(r, z, t) = \frac{B}{\sqrt{r}} U_n(t) e^{-\epsilon r} cos\left[k_r(r - ct)\right] e^{f(-k_z z)}, \tag{5.5}$$

with forcing function $U_n(t)$, constant B, absorption coefficient ϵ and mathematical function f to describe the particle orbits with depth.

Dispersion is observed for the Rayleigh wave measured in the dune sand in figure 5.4. The phase velocity is determined by tracing wave crests of the same phase. A Gaussian fit is superimposed on the signal of the Rayleigh wave, neglecting the influence of the earlier

SV-wave and the background noise. The group velocity of the wave packet is found by analyzing the propagation of the Gaussian wavelet. The group speed is $V_g = 55 \pm 5$ m/s while the phase speed propagates at $V_p = 87 \pm 6$ m/s.

The compressive wave speed for normal earth materials at the near surface is typically $\alpha = 1000$ m/s. However, prior studies of seismic velocities in a granular material shows that measured speeds in sand are much lower. Hardin and Richart (1963) measured compressional and shear wave speeds of $\alpha = 330$ m/s and $\beta = 135$ m/s respectively at a confining pressures of $\approx$ 50,000 Pa. Brownell (1977) and Bonneau *et al.* (2008) noted that the preparation of the sand in laboratory experiments strongly influenced the surface Rayleigh wave speed; both studies measured values from V_p = 40-60 m/s. The body and surface wave velocities measured in above mentioned laboratory studies compare well with the field results in this current study.

5.4.2 Frequency Content

Figure 5.2 showed that the frequency content of the burping and booming emission at Eureka dunes on 10/27/2007 differs significantly; the burping emission is broadband at a low frequency (around 60 Hz), while the booming emission is sharply defined in a narrow frequency band at 85 Hz. This section shows that these frequency differences are due to the different frequency content of the elastic body and surface wave.

Twelve geophones are arranged in plane wave orientation to record the wave propagation for three different situations: the refraction experiment in figures 5.6a through c; the burping emission in figures 5.6d through f; and the booming emission in figures 5.6g through i. The first row of panels illustrates the raw, unfiltered signal. The second row shows the signal with a band-pass filter between 25 and 60 Hz, and the third row displays the signal with a band-pass filter between 60 and 100 Hz.

The fast P-waves, the slower S-waves, and the slow Rayleigh waves are visible in the case of the impulse experiment in figure 5.6a-c. The P-waves travel in the 60-100 Hz range at a speed of $\alpha = 240 \pm 20$ m/s, but are absent in the low-pass filtered panel. The S-waves ($\alpha = 140 \pm 10$ m/s) and Rayleigh waves ($V_p = 87 \pm 6$ m/s) propagate in the 25-60 Hz frequency range and are almost not visible in the high-pass filtered panel. These characteristics show that there is a clear distinction in frequency and propagation characteristics for the different type of waves. The difference in frequency generation is due to a finite source and is observed

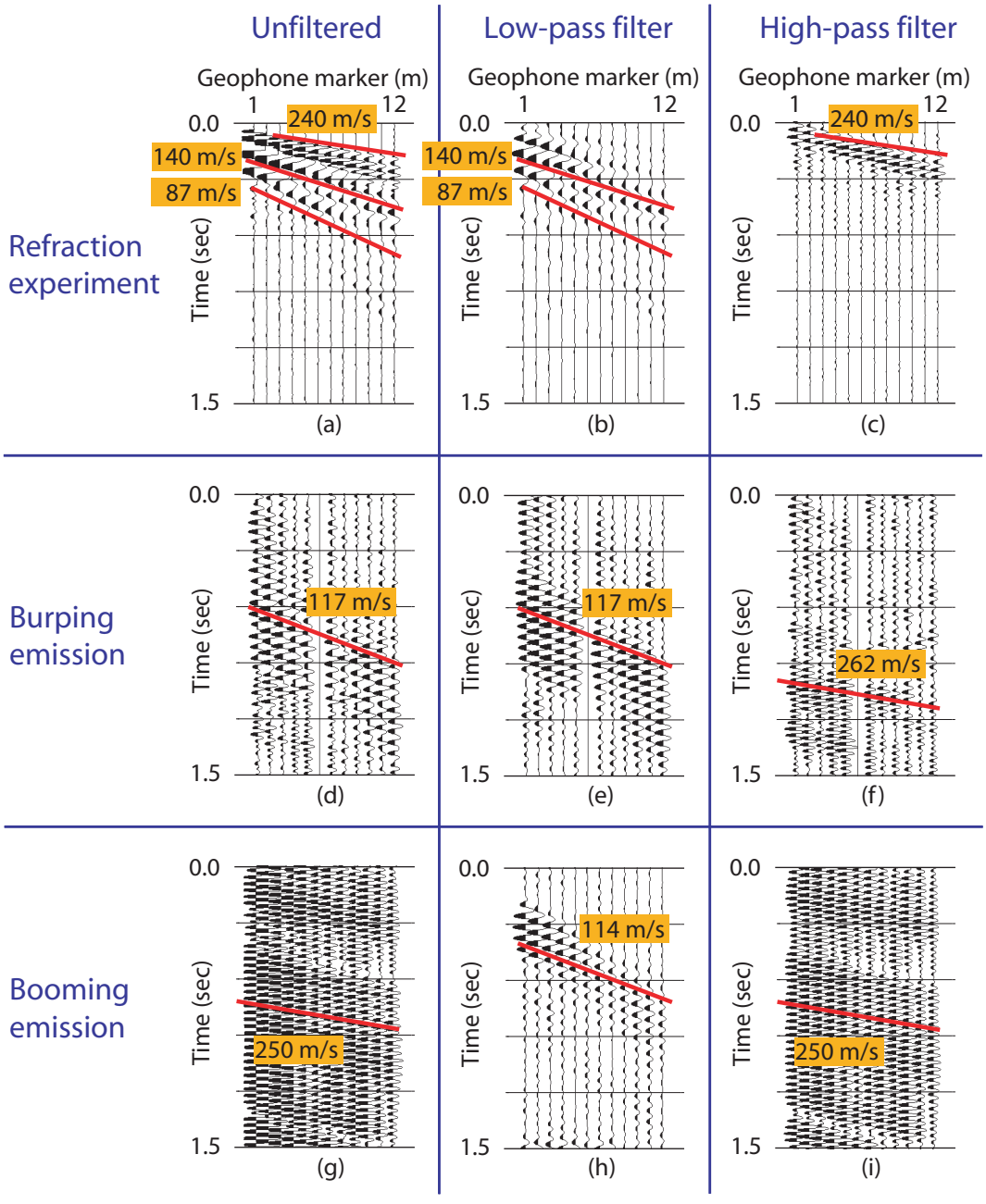

Figure 5.6: Refraction experiments showing (a) the raw signal; (b) after a 25-60 Hz band-pass filter is applied; (c) after a 60-100 Hz band-pass filter is applied. Burping experiments showing (d) the raw signal; (e) after a 25-60 Hz band-pass filter is applied; (f) after a 60-100 Hz band-pass filter is applied. Booming experiments showing (g) the raw signal; (h) after a 25-60 Hz band-pass filter is applied; (i) after a 60-100 Hz band-pass filter is applied. Experiments are from Dumont dunes on 05/29/2007. Channel six is malfunctioning in recording d through f.

for regular earth materials during earthquakes as well (Lay and Wallace, 1995).

Figure 5.6d-f show 0.5 seconds of the burping recording, similar to figure 5.2b,e. Both a fast-traveling high frequency (60-100 Hz) and a slow-traveling low-frequency component (25-60 Hz) are present in the raw signal. The slow wave travels at a velocity of V = 117 ± 3 m/s in the low-frequency range (figure 5.6e). The fast wave appears in the high frequency range in figure 5.6f and travels at a speed of V = 262 ± 8 m/s. Comparing the amplitude of the two individual components shows that the fast body wave has a smaller amplitude and does not appear in the combined unfiltered figure 5.6d. The main signal in the burping recording is therefore propagating at a low speed and at a low frequency and is a result of a pseudo-Rayleigh wave.

Figure 5.6g-i show 0.5 seconds of the booming recording, similar to figure 5.2c,f. Again, both a fast-traveling, high frequency (60-100 Hz) and a slow-traveling, low-frequency component (25-60 Hz) are present in the raw signal. The slow wave traveling at a velocity of V = 114 ± 2 m/s is faint but distinguishable and briefly appears in figure 5.6h as a low-frequency burst. The largest amplitude wave travels in the high frequency range at a velocity of V = 250 ± 5 m/s in figure 5.6i. The main signal in the booming recording is the fast-traveling, high frequency wave and is a direct result of P-wave propagation in the medium.

An analysis of frequency content and propagation speeds shows a clear distinction between burping and booming emission. The discrepancy between the speed of the burping emission ∼115 m/s and the Rayleigh wave velocity ∼85 m/s is due to a difference in amplitude and is analyzed in section 5.4.4. Andreotti (2004) measured a low phase speed V = 40 ± 10 m/s and a dispersed signal in his acoustic field experiments on a booming dune. Bonneau *et al.* (2007) concluded that a Rayleigh surface wave phenomenon is the main wavetype for the booming emission.

5.4.3 Polarization Characteristics

The analysis of behavior of particle orbits provides another method to distinguish between Rayleigh surface waves and P-waves (Vidale, 1986). Rayleigh surface waves have distinct polarization characteristics in which the particles describe a retrograde elliptical orbit (Lay and Wallace, 1995). The wave motion of a body P-wave is in the direction of the wave propagation. The adaptation of three-component geophones at the surface of the dune provides information about the type of waves involved in the burping and booming emission.

The three-component geophones, with one vertical and two horizontal sensors, are each oriented parallel to gravity in the field experiment. Post processing converts the components of the raw signal to a coordinate system (V, H_1, H_2) parallel to the dune surface, as illustrated in figure 5.3. Frequency analysis shows the signal in each of the three components has the same frequency content for all emissions.

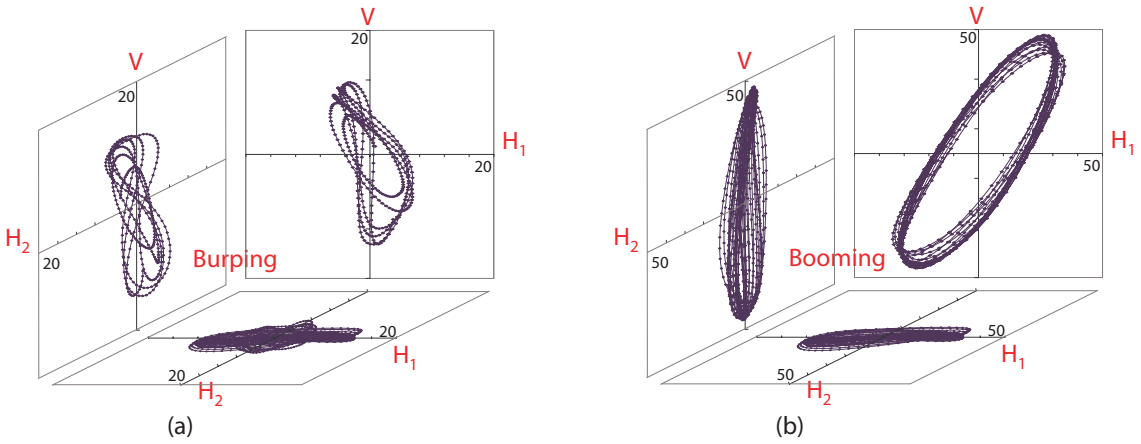

Figure 5.7: Polarization plot of 3 component geophone recordings with a vertical (V), lateral horizontal (H_1) and longitudinal horizontal (H_2) component for the (a) burping and (b) booming recording on Eureka dunes on 10/27/2007. The burping recording (axis scaling ± 20) has a lower amplitude than the booming recording (axis scaling ± 50), as is evident from figure 5.2.

Plotting two different components of the geophone output creates a particle orbit plot, which provides information about the character of waves. The particle orbits of the burping emission in figure 5.7a show a chaotic behavior without a repeatable pattern in either of the three combinations. In contrast, the particle orbits of the booming emission illustrated in figure 5.7b show repeatable ellipses in each of the three representations. The H_2 component perpendicular to the wave direction is small compared to the other two direction indicating that the out-of-plane motion associated with Love and/or SH-waves are not responsible for the emission. The major axis of the particle orbit for the V-H_1 combination is not perpendicular to the surface, but tilts strongly under an angle of 54°. Further analysis of the particle orbit for the booming emission shows that the elliptical particle orbit switches direction in the V-H_1 space after each instability as shown in figure 5.8. A chaotic transition regime occurs when the signal amplitude reduces–the sustained booming fades for a fraction of a second. The displacement of a particle during a seismic booming wave shows a regular

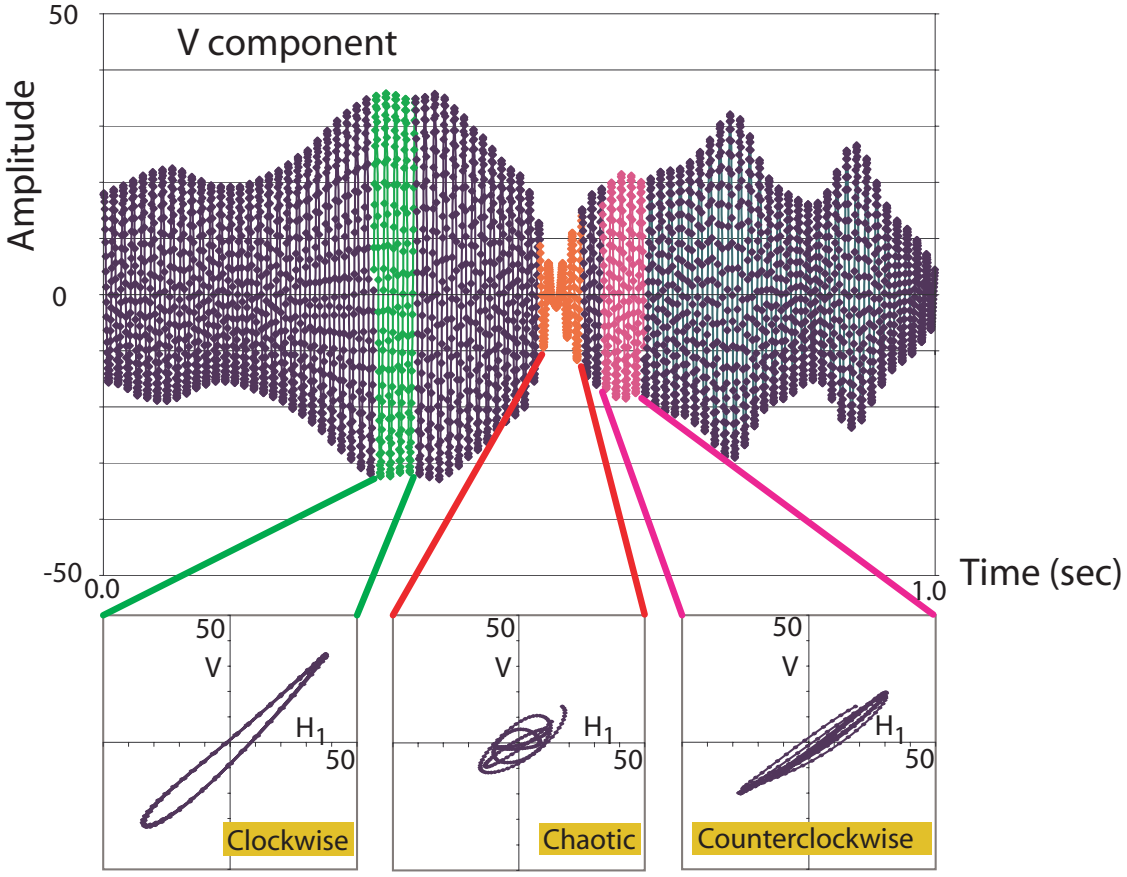

Figure 5.8: Polarization characteristics of 1 sec of the booming recording at Eureka Dunes on 10/27/2007. The original signal is the V-component, for which the beating of the signal is apparent. The orientation of the ellipse switches from clockwise to counterclockwise via a state in which chaotic movement is observed.

behavior in the V and H_1 directions. The repeatable particle path displays alternating prograde and retrograde ellipses tilted under an angle. The narrow ellipses have a maximum amplitude ratio of $V/H_1 = 42/30 = 1.4$. The ratio corresponds to an angle of 54° with the horizontal as illustrated in figure 5.9. The critical angle is $\theta_{cr} = 35°$ for a waveguide with characteristic velocities $c_1 = 200$ m/s and $c_2 = 350$ m/s and corresponds to an angle of 55° with the horizontal. Therefore, the V and H_1 components map out the displacement of a particle in the waveguide during the passing of a P-wave. A Rayleigh wave would display a retrograde elliptical orbit with an amplitude of the vertical component at the surface of about 1.5 times the amplitude of the horizontal component and does not switch orientation. These characteristics of a Rayleigh wave are not consistent with the observed behavior of

the wave responsible for the booming emission.

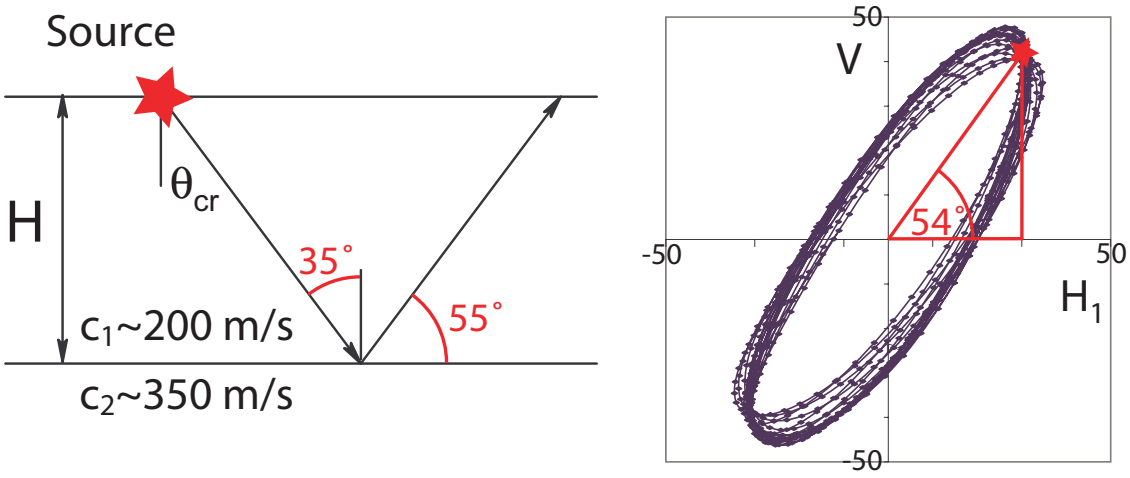

Figure 5.9: Comparison between the orientation of the P-waves in a waveguide and the orientation of the V and H_1 component of the geophone.

5.4.4 Dispersive and Nonlinear Behavior

Andreotti (2004) posed that the booming emission showed strong dispersive behavior. The author played a signal on a tape recorder during in situ experiments and derived the non-linear response through the sand bed by quantifying the dispersion relation. Bonneau *et al.* (2008) determined a distinct phase and group speed for the wave propagation in a laboratory experiment and predicted nonlinear behavior.

The impulse seismic refraction experiment presented in figure 5.4 shows that the Rayleigh wave displays dispersive behavior with a phase speed of $V_p = 87 \pm 6$ m/s and a group speed of $V_g = 55 \pm 5$ m/s. The burping emission displays dispersive behavior as well, as observed in figure 5.6e. A recording from Dumont dunes on 06/01/2008 (figure 5.10a) is used to characterize the dispersive behavior because the signal could be following in time without significant background noise. Fitting a Gaussian shape to the signal gives a group speed of $V_{gb} = 52 \pm 5$ m/s. The duration of the burping pulse is not a function of distance to the source, but remains constant. The phase speed for the wavelets in figure 5.10a is found by tracing the crest of a waveform in time and space. This phase speed decreases strongly from $V_{pb} = 148 \pm 14$ m/s at maximum amplitude to $V_{pb} = 110 \pm 6$ m/s toward the beginning and end of the pulse where the amplitude is lower. The discrepancy between the group and

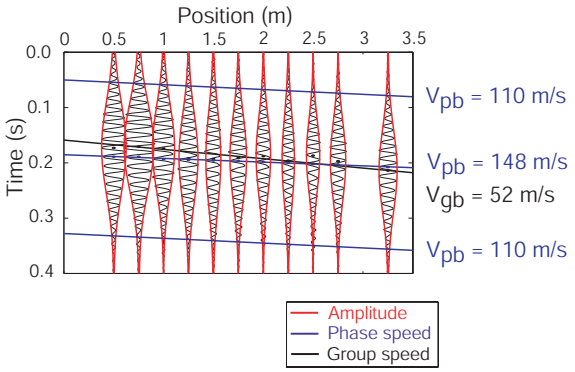

(a) Evolution of the burping pulse in space and time, indicating dispersive behavior.

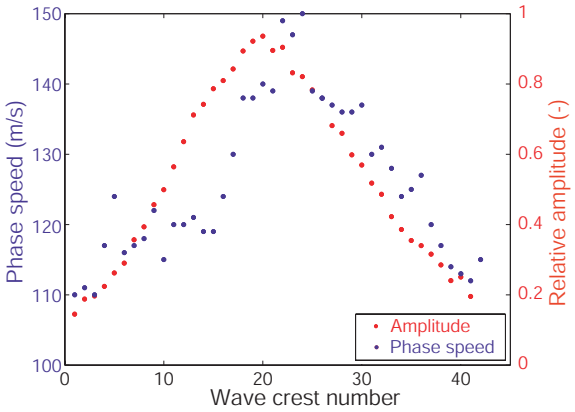

(b) Correlation between the amplitude and the phase speed of individual wave crests, indicating a nonlinear behavior.

Figure 5.10: Investigation of dispersive and nonlinear behavior. The recording of the burp was made at Dumont Dunes on 06/01/2008.

phase speed indicates strong dispersion of the burping emission. The discrepancy between the phase speed of the wave in the burping experiment (V_{pb} =110-148 m/s) and the Rayleigh wave in the refraction experiment (V_p = 87 m/s) is due to the nonlinear behavior of the wave propagation.

Figure 5.10b shows the changing phase speed of the burping waveform as a function of wave crest number. The phase speed correlates directly to the amplitude ratio of the crest, which is a strong indication of nonlinearity of the pulse. The phase speed is similar to a nonlinear Korteweg-de-Vries wave equation used for granular materials (Nesterenko, 2001) in which the phase speed depends directly on the amplitude. The higher velocity of the center part of the pulse due to nonlinearity should produce a shock wave unless dispersive

behavior counteracts the nonlinear effects. The exact interaction between nonlinearity and dispersive behavior for the burping emission remains an open question. Further work should include more extensive work on quantifying the exact nature of the nonlinear and dispersive effects.

5.5 Conclusion

This paper provides quantitative detail on the sound propagation in field studies to distinguish the type of waves that are responsible for the generation of the short burping and the sustained booming emission. Bonneau *et al.* (2007) posed that Rayleigh waves are crucial for the propagation of the booming emission. Vriend *et al.* (2007) proposed an alternative explanation in which P-waves propagate in a waveguide and produce the booming sound.

The impulse seismic refraction studies show the existence of body P- and S-waves and surface Rayleigh waves in a granular material. Although both Rayleigh waves and P-waves are present during an acoustic emission on a sand dune, sustained booming is a result of body wave propagation and short-pulsed burping is related to Rayleigh surface wave propagation. The burping emission has a lower broadband frequency ($\sim$ 60 Hertz) and travels at a slower velocity ($\sim$ 115 m/s). The prolonged booming emission propagates at a high frequency ($\sim$ 85 Hz) and at a higher velocity ($\sim$ 250 m/s).

Three component geophones show that for the booming emission the out-of-plane component is small and that the displacement of particles is in the same direction as the P-waves in the waveguide model. The particle paths are alternating prograde and retrograde, strongly tilting with the horizontal and not compatible with Rayleigh wave motion. The burping emission shows both dispersive and nonlinear characteristics, similar to Rayleigh surface wave behavior. Burping and booming emissions are different acoustic phenomena and are governed by different physical principles.

The low-speed (40 m/s), dispersive signal that was obtained by Andreotti (2004) is most likely a low amplitude direct measurement of Rayleigh wave behavior, and is not a measurement of the propagation speed of booming. The booming emission is due to a P-wave type of behavior and is explained by the waveguide model as presented in Vriend *et al.* (2007). The difference in wave propagation characteristics of the two acoustic emissions explains the controversy.

5.6 Acknowledgments

The authors would like to thank Chiara Daraio for the stimulating and fruitful discussions on wave propagation in a granular material. The help of Natalie Becerra, Angel Ruiz-Angulo, Erin Koos and many others, was essential during the field experiments at Dumont and Eureka dunes. Travel and equipment support for N. M. V. was provided through funding from the Pieter Langerhuizen Lambertuszoon Fonds.

Chapter 6

Stratigraphy of Dumont and Eureka Sand Dunes

The subsurface features of sand dune fields of the Mojave Desert show evidence of dune building, wind regime, and precipitation history. The current research presents ground penetrating radar images up to 40 m in depth of two large desert dunes in California, USA– a barchanoid ridge in the Dumont field and a linear dune in the Eureka expanse. The images show a complicated structure of internal layering with climbing cross-strata, cross-bedding and bounding surfaces cutting through layers. Additional research using seismic refraction surveys and sand sampling refine the image of the subsurface (< 5 m) structure. The stratigraphy of the dune shows a strong internal layering with a cemented structure that may immobilize and influence migration of dune expanses.

6.1 Introduction

The Mojave Desert features the highest temperatures in the United States. The desert area lies between 35-36°N latitude and 115-117°E longitude in South East California. The arid landscape features several dune systems (figure 6.1) that originated in the early and mid-Holocene period (Pavlik, 1989). Short-term climatic changes influence the wind strength, direction and precipitation in a region. The wind affects the appearance and shape of the dune, while precipitation has a direct impact on vegetation on the dune surface and on the internal structure beneath the surface (Lancaster, 1996). The moisture content within a dune in arid regions comes from atmospheric inputs such as rain and humidity and ground-water inputs due to capillary transport (Namikas and Sherman, 1995). Vegetation, moisture

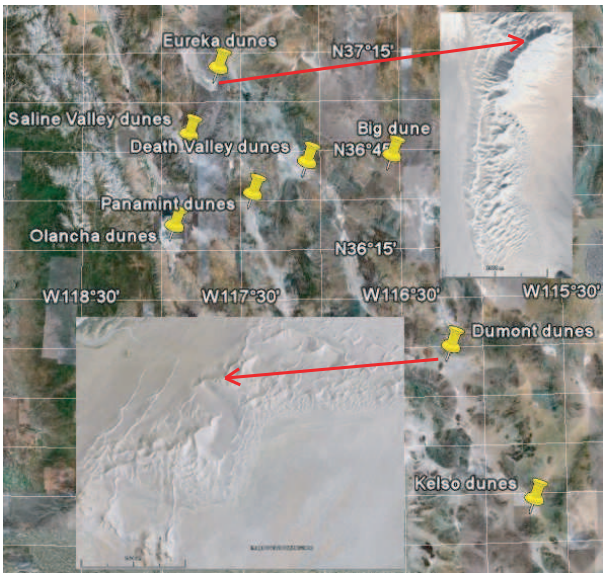

Figure 6.1: Locations of dune systems within the Mojave desert. The inserts show a satellite map of Eureka dunes and Dumont dunes

content and sand supply directly influence the mobility of a dune field and determine whether a system is dormant and stationary or strongly migrates across the desert plane (Greeley *et al.*, 1995).

Long-term climatic changes influence the sediment supply in a region, including particle size distribution and chemical content of the sand. Wind transports sand by saltation and prolonged exposed to aeolian environment changes the sorting and shape of the sand grains. The degree of angularity (roundness) reflects the duration of abrasion in the transport of sediments while the sphericity provides an indication of the history of the sedimentary environment (Thomas, 1987). The sorting of sediments in dunes follows as a first approximation a log-normal distribution (Flenley *et al.*, 1987). The fine sediments including colloids, clay and silt particles are too small to be carried by the wind and are removed from the landscape by suspension (Bagnold, 1941). Gravel-sized particles cannot be transport by saltation and move by impact creep along the surface (Bagnold, 1941). The changing topography of dunes limit the interaction of the gravel-sized sediment with the sediment involved with dune building and migration. As a result, the clay and gravel-sized particles are underrepresented in particle size distributions of sediments found near the crest on sand dunes (Livingstone, 1987).

Basic important parameters of sand dunes are their migration direction and speed and their internal structure. These parameters relate to the climatic and depositional environment that create and preserve the dunes and are consequently important indicators for classification of a dune system. The current paper presents geophysical observations and field measurements of the stratigraphy of two large desert dunes in the Dumont and Eureka dune field in the Mojave desert and connects the observations with the short and long-term climatic history. The internal stratigraphy shows a fascinating snap-shot of the dune building and migration characteristics and presents the observer a look back in time. The complex internal layering within the dunes is due to a geochemical interaction that cements the sand during major climatic events.

6.2 Regional Geologic and Climatic Setting

The field areas of the current study are two large desert dunes in the Dumont (figure 6.2a) and Eureka (figure 6.2b) dune field.

(a) North-facing (leeward) face of the Dumont Dune

(b) West-facing face of the Eureka Dune

Figure 6.2: Field locations

6.2.1 Dumont Dunes

The Dumont dune field (latitude 35°41′00″N, longitude 116°13′07″W) is situated in the northern part of the Mojave Desert in California, USA and has been visited on 29 different field days in the period 2003-2009. The Dumont dune field covers an area of approximately twenty square kilometers (MacDonald, 1966) near the southern tip of Death Valley. The

core of the dune field consist of star dunes with smaller barchan and longitudinal dunes surrounding on the flanks. The highest dune in the center of the dune field rises 120 meters (Nielson and Kocurek, 1987) above the desert floor. The dune selected for this research is easy to approach with support vehicles and is near to the north-western flank of the dune field. The 50-meter high dune, shown in figure 6.2a is a barchanoid ridge (McKee, 1977) with a distinct slip face. A laser rangefinder maps the topography of the dune shown in figure 6.3.

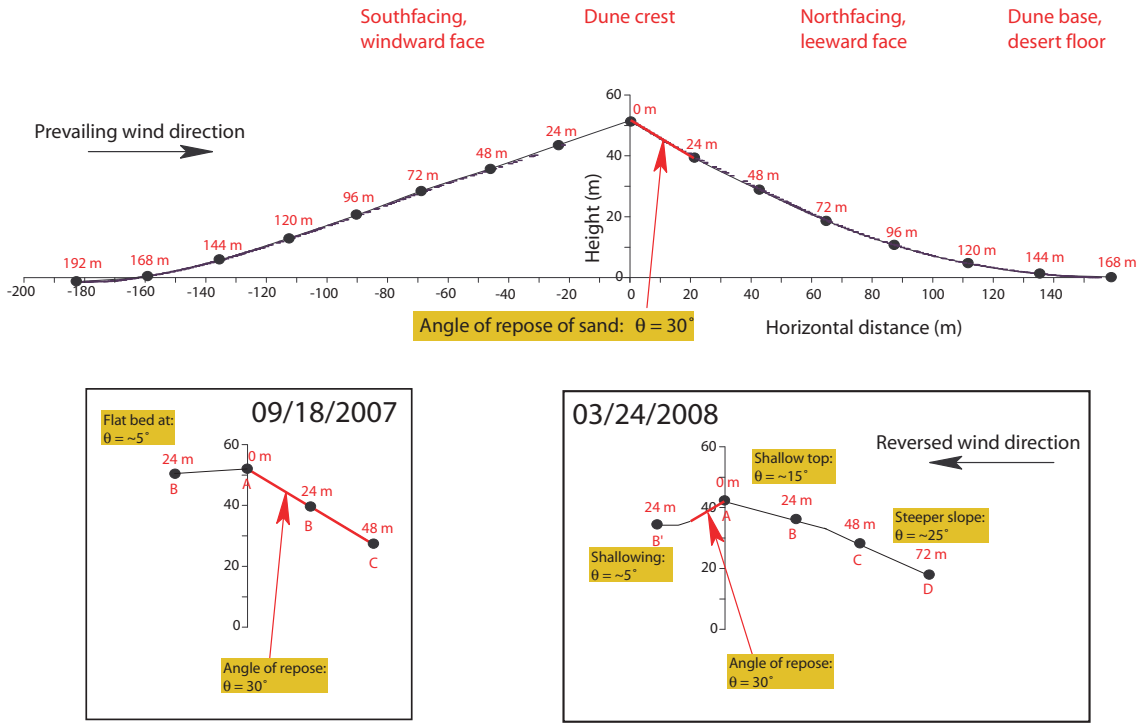

Figure 6.3: Topography of the Dumont dune on 06/02/2008 measured with a laser rangefinder. The inserts show the alternative topography near the crest of the dune on 09/18/2007 and 03/24/2008.

The north-facing leeward slope is formed when the sand grains blow over the crest and deposit by grainfall. The deposits of grainfall form as well-mixed lamination structures without segregation within an individual layer and thin downslope (McKee, 1977). When a sufficient amount of sand is deposited on the upper leeward face, the slope steepens beyond the natural angle of repose of sand ($\sim 30°$) and local failing of the slope results in grain-flow. Grainflow produces cross-strata and inverse sorting due to segregation and typically thickens downslope (Hunter, 1977). The slope on the leeward face breaks significantly at

approximately 48 meters from the crest forming the transition between grainfall/grainflow and solely grainfall regions. The south-facing windward slope is firmer and shallower with a constant slope angle (∼20°) for over 100m downslope. On most occasions, sand ripples form on the surface of the windward face whereas no ripples are observed on the leeward face.

Seasonal changes in wind direction also resulted in changes to the surface features of the dune. For example on 09/18/2007, the brink of the dune was elongated producing a flat region that extended for 30 meters to the windward side of the crest. During a visit six months later (03/24/2008), the dune crest had reversed. The lower north-facing slope was slightly shallower then normal at approximately 25°, but the upper north-facing slope was at a constant slope angle of 15° from the crest to 36 meters from the crest. Reversal of the crest was observed with a short (14 m) steep slipface on the south-facing slope.

The visual observations are in agreement with the governing wind regime. The shape of the dune and the migration characteristics are influenced by the strength of the wind and the variation in directionality. Whether aeolian sediment transport occurs for a given wind depends strongly on the size of the particles (Hunter, 1977). The fluid threshold (Bagnold, 1941) dictates the minimum wind speed required to initiate motion of a certain particle size and on Earth is equal to 0.2 m/s. Wind speeds higher than these values are winds of dune building strength. The variation in directionality of the wind influence the type of dune (Hunter, 1977). Barchanoid ridges, such as the Dumont dune in the current research, are formed when the wind is transverse to the crest with a medium to large sand supply (McKee, 1977). The reversed crest observed in the wintertime of 2008 is a manifestation of bimodal winds from the opposite direction and is known as a reversing dune. The primary slipface of the barchanoid dune due to the unidirectional wind may be briefly covered by a miniature dune due to the reversing wind. After the normal wind regime has reinstated, the small reversing dune disappears.

Nielson and Kocurek (1987) observed that the wind regime at Dumont dunes differs from season to season. MacDonald (1966) investigated the variation with season by evaluating statistics of dune building winds from the weather station at Silver Lake, California (latitude 35°20′N, longitude 116°05′W). Although the Silver Lake weather station is not operational anymore, similar wind regime data is obtained from Mojave River Sink (latitude 35°03′11″N, longitude 116°04′46″W), the closest active weather station to Dumont dunes. The wind rose graphs for the period July 2007–June 2008 (figure 6.4) show a strong seasonal variation in

wind strength and direction. Low strength northerly winds are recorded in the wintertime while stronger westerly and southerly winds dominate the dune building winds in the summer time. The slip-face on the north-faced slope is due to the strong unidirectional wind regime in the summertime. In the wintertime the winds are weaker and mainly come from the north. The temporarily reversed dune structure observed in March 2008 is in agreement with temporal calm winds from the north.

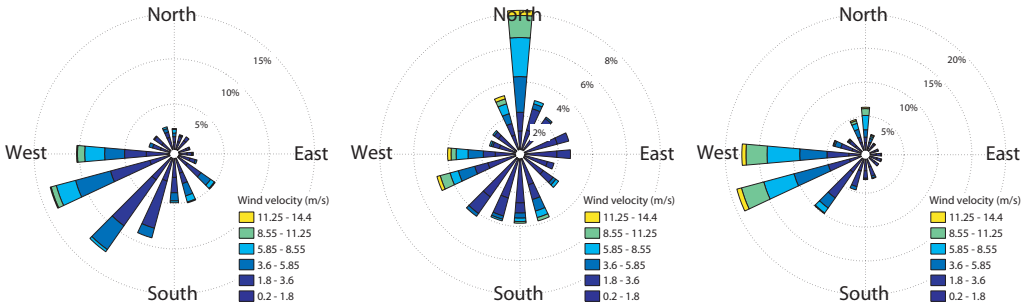

(a) July 2007–October 2008, with 20.8 % calm events

(b) November 2007–February 2008, with 45.2 % calm events

(c) March 2008–June 2008, with 14.9 % calm events

Figure 6.4: Wind rose graphs for Mojave River Sink (latitude 35°03′11″N, longitude 116°04′46″W), the closest weather station to Dumont Dunes. Calm events have wind speeds below the velocity threshold of 0.2 m/s.

The alternating seasonal wind directions indicate that the dune oscillates slightly during a full year and might not have a large migration rate. Optical imagery (Leprince *et al.*, 2007) uses satellite images to correlate relative horizontal ground deformation between images. Comparison of two images of the Dumont dune region from 2000 and 2005 in figure 6.5a shows that the barchanoid ridge migrates slowly. The dune crest only show a horizontal displacement of one to a few meters per year in the northernly direction.

The precipitation events in the desert are short with only a few (1-3) days per month recorded rainfall (figure 6.6a). The annual precipitation varies strongly from ∼30 mm in 2002 and 2006 to $\sim 150mm$ in 2003 and 2005 and most rain falls in February and August. In the summertime, the moisture of the precipitation is evaporated within a few days when the average temperature rises well above 35° C and average maximum daytime temperatures above 45° C (figure 6.6b). The average temperature drops to 10° C in the wintertime, which reduces the driving potential of moisture transport out of the dune.

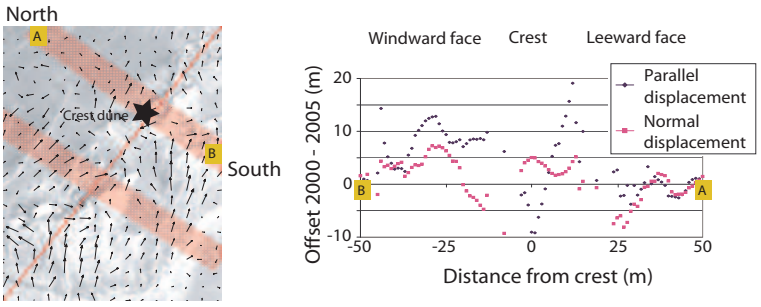

Figure 6.5: Vector graph of the dune migration over the period 2000-2005. Optical imagery of satellite images correlate relative horizontal ground deformation. The section A-B is drawn in north-south direction across the crest of the dune shown in figure 6.2a. The star indicates the position of the dune crest within the section.

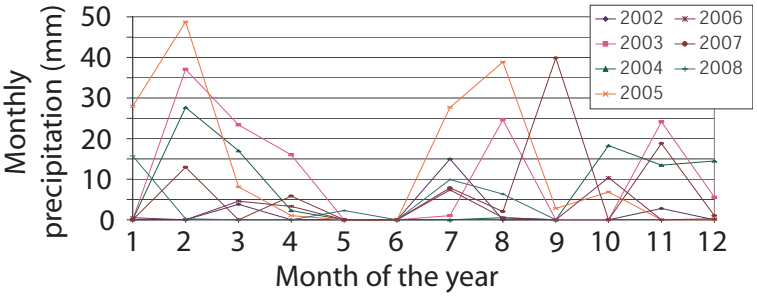

(a) Monthly precipitation for 2002-2008

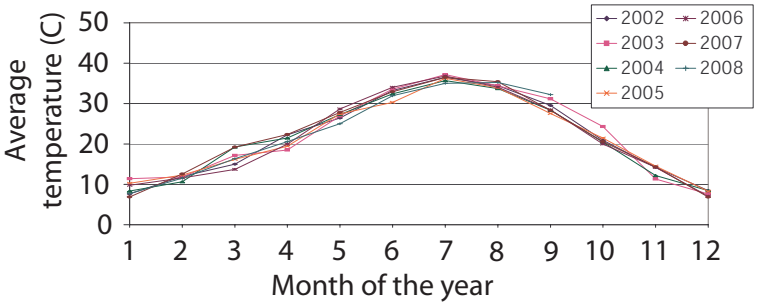

(b) Monthly average temperature for 2002-2008

Figure 6.6: Environmental data is collected from Mojave River Sink (latitude 35°03′11″N, longitude 116°04′46″W) which is the closest weather station to Dumont Dunes.

6.2.2 Eureka Dunes

The Eureka dunes (latitude 37°06′44″N, longitude 117°40′51″W) are situated in Eureka Valley in the northern part of Death Valley National Park in California, USA and has been visited on 6 different field days in 2002, 2007 and 2008. The highest peak of the Eureka

Dune system rises about 200 meters above the surrounding valley floor. Several type of dunes are superimposed on top of each other in the dune field. The dune selected for this research is a linear dune and rises 60 meters above the surrounding dunes (figure 6.2b). A laser rangefinder is used to record the topography of the dune as recorded in figure 6.7.

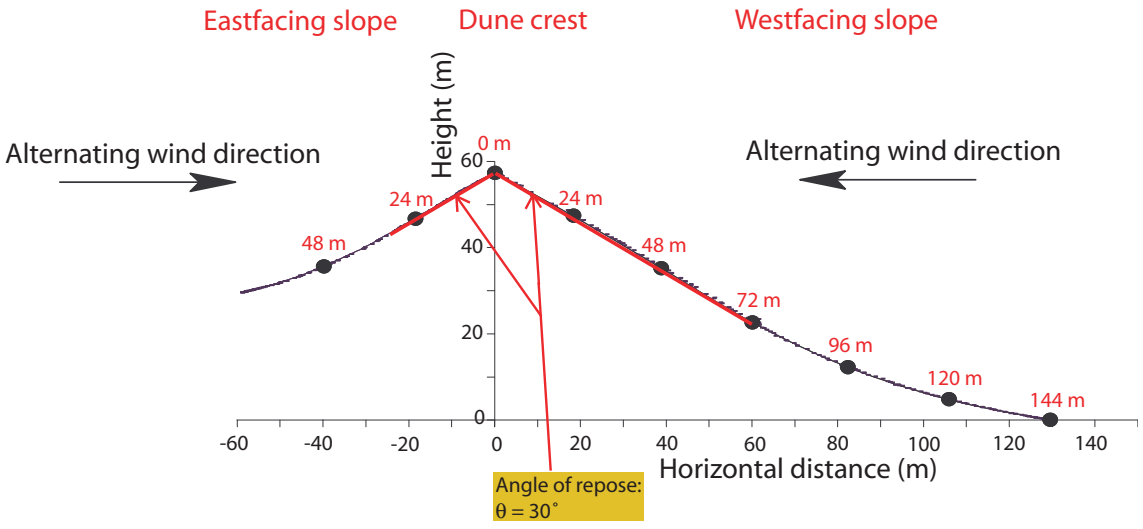

(a)

Figure 6.7: Topography of the Eureka dune on 07/17/2008 measured with a laser rangefinder.

The east-facing and west-facing surface are both at the angle of repose for 30 meters on the east-facing slope and for 72 meters on the west-facing slope. The characteristic dual slip face structure of linear dunes, such as the Eureka dune in the current study, is a result of winds from two directions (McKee, 1977). This bimodal structure indicate a complicated wind regime with common reversals of prevailing dune building winds. Recent research suggests that large linear dunes do migrate laterally (Livingstone, 1987). Research by Livingstone (1987) demonstrates that a large (∼70 m) linear dune in the Namib Desert shifts back and forth by ∼15 m due to short-term climatic seasonal wind changes. (Bristow *et al.*, 2007) showed that a net migration of ∼300 m laterally occurred on a longer time-scale (∼2500 years) and posed that large migrations may be temporarily activated or deactivated by long-term climatic changes in rainfall and vegetation.

The average precipitation from long-term climate data is 115 mm per year with most of the rain falling between November and March; similar to Dumont Dunes, there may also be thunderstorms in July and August (Pavlik, 1980). The summer daily temperatures exceed

40 °C between June and August and the minimum temperature between November and March may drop below freezing point. Because there are no active weather stations in the nearby region, information could not be obtained on the prevailing wind directions.

6.3 Layering Structure of a Dune

The stratigraphy of sediments in a sand dune are commonly exposed by digging trenches and examining the deposits (McKee, 1977; Nielson and Kocurek, 1987). Trenching involves a physical and time-consuming process and is impractical: a collapse of the trench and the continuous avalanching of dry loose sand may complicate the interpretation of layers and only one discrete location along the slope of the dune is examined. Ground penetrating radar (GPR) experiments provide a continuous measurement of discrete layers within a dune.

Although GPR is a well-known method to investigate aquifers and faults (Reynolds, 1997), the technique has only been sparsely employed to investigate the stratigraphy of sand dunes (Bristow *et al.*, 2000; Grandjean *et al.*, 2001; Schenk *et al.*, 1993). In radar surveys a comprehensive image of the subsurface structure supplements observations of surface features. In the current research two techniques are used to investigate the stratigraphy of the subsurface–ground penetrating radar investigates the subsurface of the dune and sand sampling provides a direct measurement of the local composition and water content.

Vriend *et al.* (2007) investigated the subsurface structure of a dune with seismic refraction experiments. The seismic surveys provide point measurements of the internal layering and do not provide a continuous profile of the layering within a dune. The seismic refraction experiments are valuable to obtain seismic speeds within the dune sand, but provide only approximate correct depths because of the large uncertainty in travel times.

6.3.1 Ground Penetrating Radar

Ground Penetrating Radar (GPR) is based on the propagation of electromagnetic waves (Baker *et al.*, 2007). The survey is conducted with a PulseEkko 100 system with two different antennas. The 100 MHz antennae has a larger penetration depth and a low resolution and the 200 MHz antennae images the near-surface structure at a higher resolution. The contrast in a radargram is due to the reflection of waves off interfaces with large changes in radar velocity. The radar velocity depends on the dielectric material properties and may change

slightly between different field dates.

The radar velocity is obtained from a common-midpoint (CMP) survey centered around a point 24 meters on the leeward face of the dune. Only reflections and no refractions are expected because of the decrease in radar velocity with depth (Reynolds, 1997). The radar velocity and the position of each layer are found by tracing the individual hyperbolas in the shot record of the CMP survey as illustrated in figure 6.8. The radar velocity in sand decreases from 181.10^6 m/s at the surface to 142.10^6 m/s at a depth of 8.0 meters. The position of a layer $H = \frac{1}{2}V_r t_0$ depends on the two-way travel time t_0 to a reflection in the image and the radar velocity V_r.

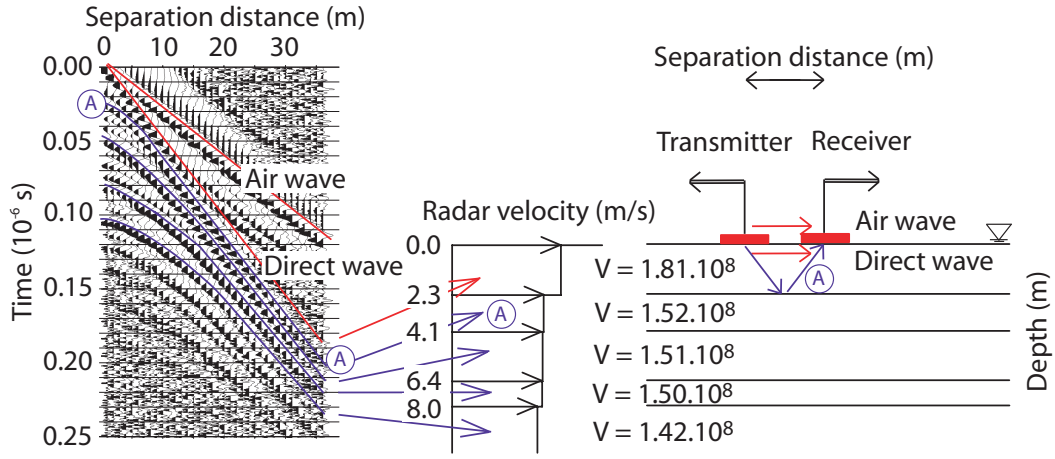

Figure 6.8: Common-midpoint gather of a survey with a 200 MHz antenna at Dumont dunes on September 18th, 2007. The transmitting and receiver antennas are separated by and additional 1 meter for each trace. The air and direct wave are straight lines in the shot record and have a velocity of 300.10^6 m/s and 181.10^6 m/s respectively. The reflection hyperbola originate from discrete layers within the subsurface–the curvature determines the radar velocity and the intersection with the origin sets the depth of the layer. Only reflections are recorded as the radar velocity decreases with depth.

The 100 MHz antenna penetrates deeper in the dune, up to 30 meters at Dumont and up to 40 meters at Eureka dunes depending on local electromagnetic properties. The 200 MHz antenna provides a better resolution near the surface of the dune, but claims a trade-off due to a shallower penetration. The results of the radar profiles for four different field experiments at Dumont are presented in figure 6.9 for the 200 MHz antenna and figure 6.10 for the 100 MHz antenna. The structure on the leeward face is dominated by parallel layers at the angle of repose in the upper regions of the dune. The slope on the leeward

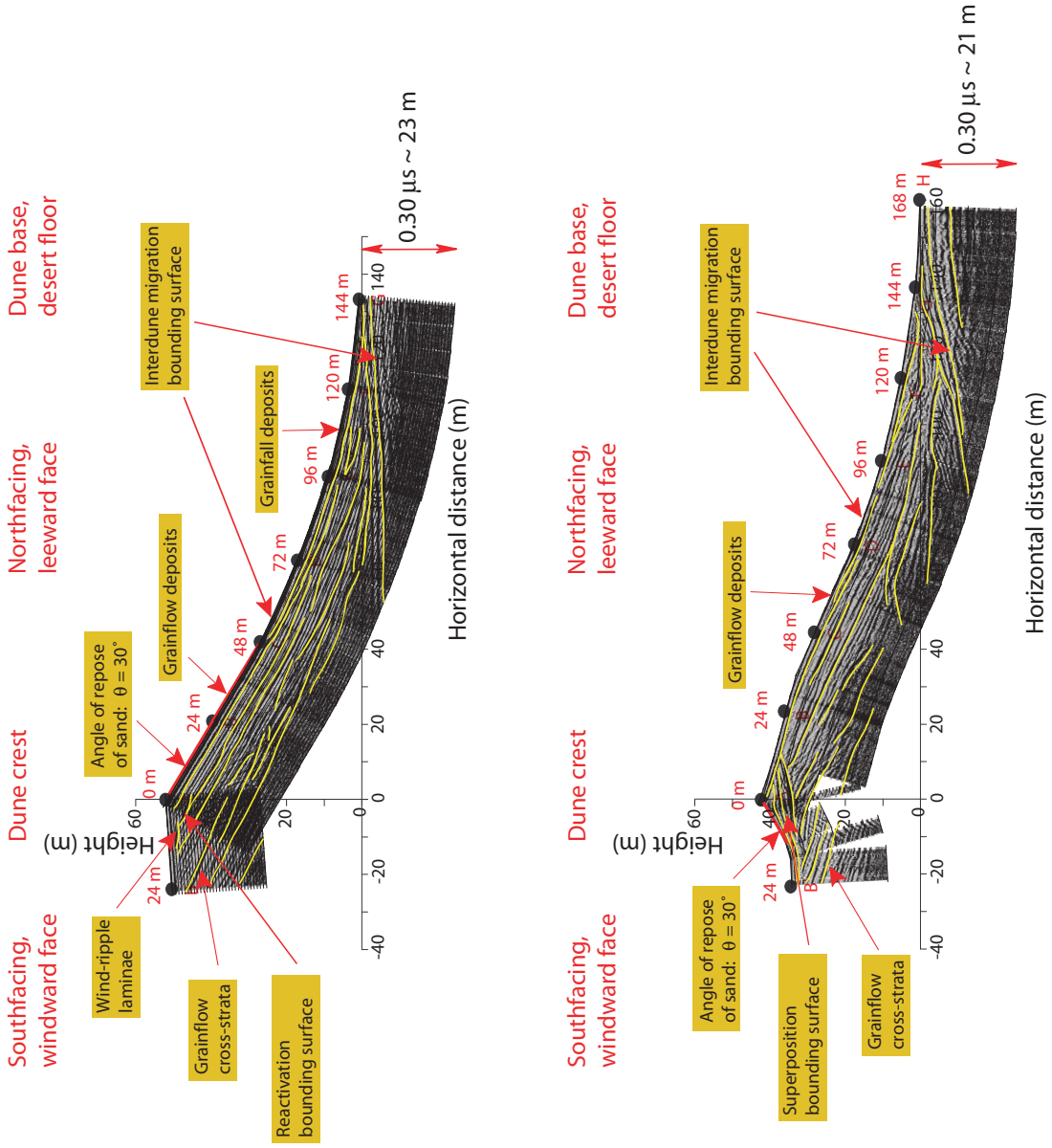

(a) 09/17/2007

(b) 03/24/2008

Figure 6.9: Stratigraphical structure of the Dumont dune measured with 100 MHz ground penetrating radar. The profile is scaled with the radar velocity such that the time coordinate is approximately equal to the spatial coordinate. The yellow lines follow the local reflection profiles and are added for interpretation.

face breaks significantly at a point between 24 and 48 meters from the crest and forms the transition between grainfall and grainflow regions. A thickening in the structure occurs at the transition between the grainfall and grainflow region and the layers become irregular and

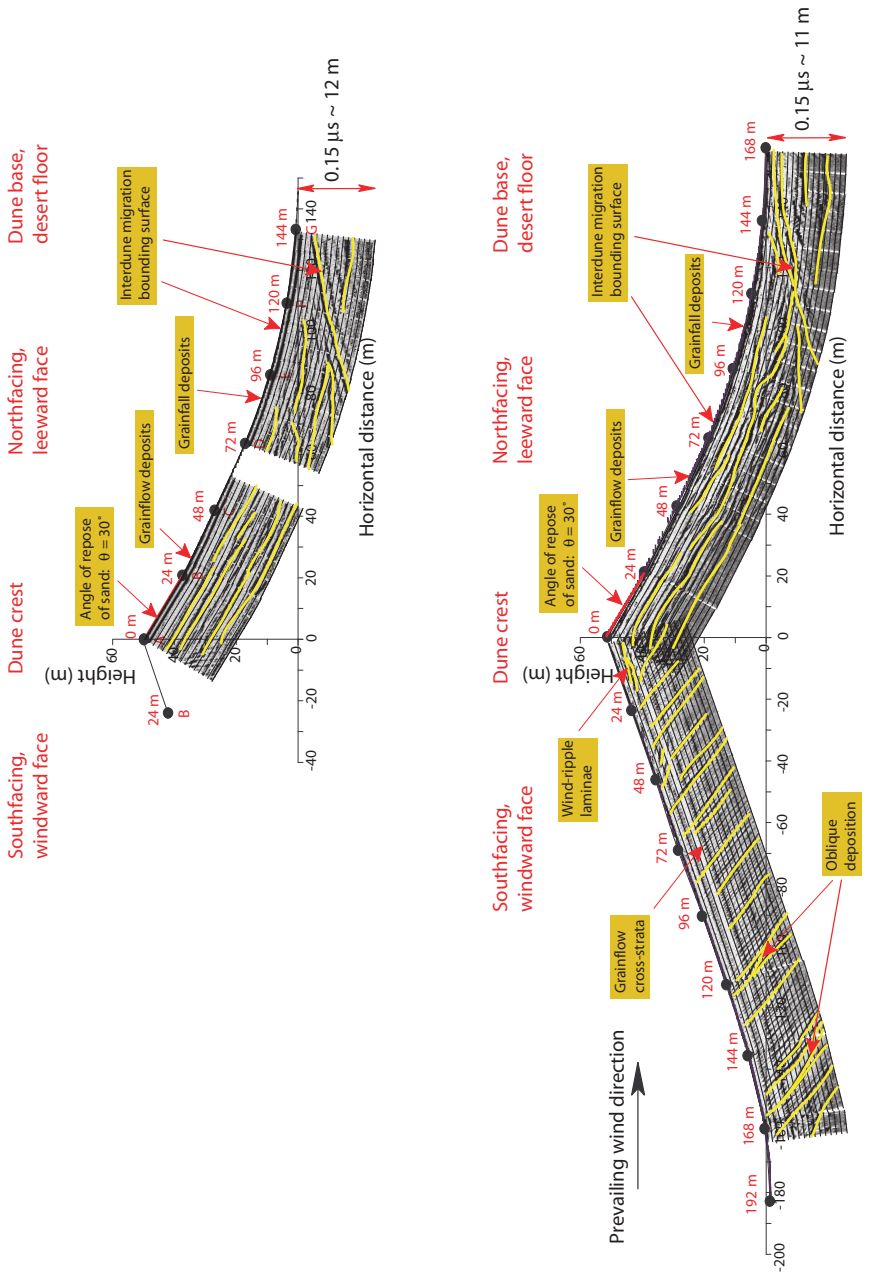

(a) 05/29/2007 (b) 06/02/2008

Figure 6.10: Stratigraphical structure of the Dumont dune measured with 200 MHz ground penetrating radar. The profile is scaled with the radar velocity such that the time coordinate is twice the spatial coordinate. The yellow lines follow the local reflection profiles and are added for interpretation.

thins near the base of the dune. The desert floor shows up distinctively in the radar profile as a horizontal layer that slightly dips underneath the dune itself. Cross-bedding occurs

on a limited basis and especially towards the base of dune. The structure on 03/24/2008 shows a flattened crest with strong cross-bedding penetrating the upper part of the leeward slope. Visual observations of the surface on the windward face do not indicate any change in structure penetrating through the surface. The internal structure from radar profiles however features for all field dates strongly dipping layers, at an angle of $\sim 30°$, penetrating up to the surface of the windward face. This cross-bedding is a direct result of migration of leeward faces in the downwind direction.

The results of the 200 MHz profiles for two different field experiments at Eureka are presented in figure 6.11. Strong subsurface parallel layering characterizes both the west and east facing slope on 10/27/2007. At the location where the slope breaks significantly the layering thickens and new layers appear closer to the surface. The radar profile of the east and west face on 07/17/2008 show continuous thinning downslope, very similar to the structure observed by (Bristow *et al.*, 2000) for linear sand dunes. Extensive cross-bedding occurs throughout the entire profile. The horizontal "supersurface" bounding surface (Kocurek, 1996) is evidence of eroded and buried compound dunes. Most noticeable is the very strong reflection of a buried dune crest in figure 6.11b at approximately 115 meters from the crest.

Kirchhoff migration on GPR profiles has been applied to translate the time dimension to a spatial dimension. The complex dune structure is resolved to a depth of over 30 meters for the 100 MHz antenna, as illustrated in figure 6.12. The migrated figures show several internal crests that oscillate slightly between west and east with depth. The stars in figure 6.12 indicate the position of the internal crests.

6.3.2 Sand Sampling

A Raman spectroscopy measurement shows that the Dumont sand is composed of quartz and K- and Na-feldspar components. A x-ray fluorescence measurement of Dumont sand quantifies heavier chemical elements ($Z > 11$) and shows in the crest sand a large component of silicium (32.66%) and intermediate quantities of aluminium (6.04 %), natrium (3.08 %), potassium (2.92 %) and calcium (2.20 %). The sand from the base of the dune has similar major components, but less calcium (1.90 %).

The granular material sand has a distribution of particle sizes. Livingstone (1987) investigated 325 samples collected from 25 sites on a linear dune in the Namib desert over

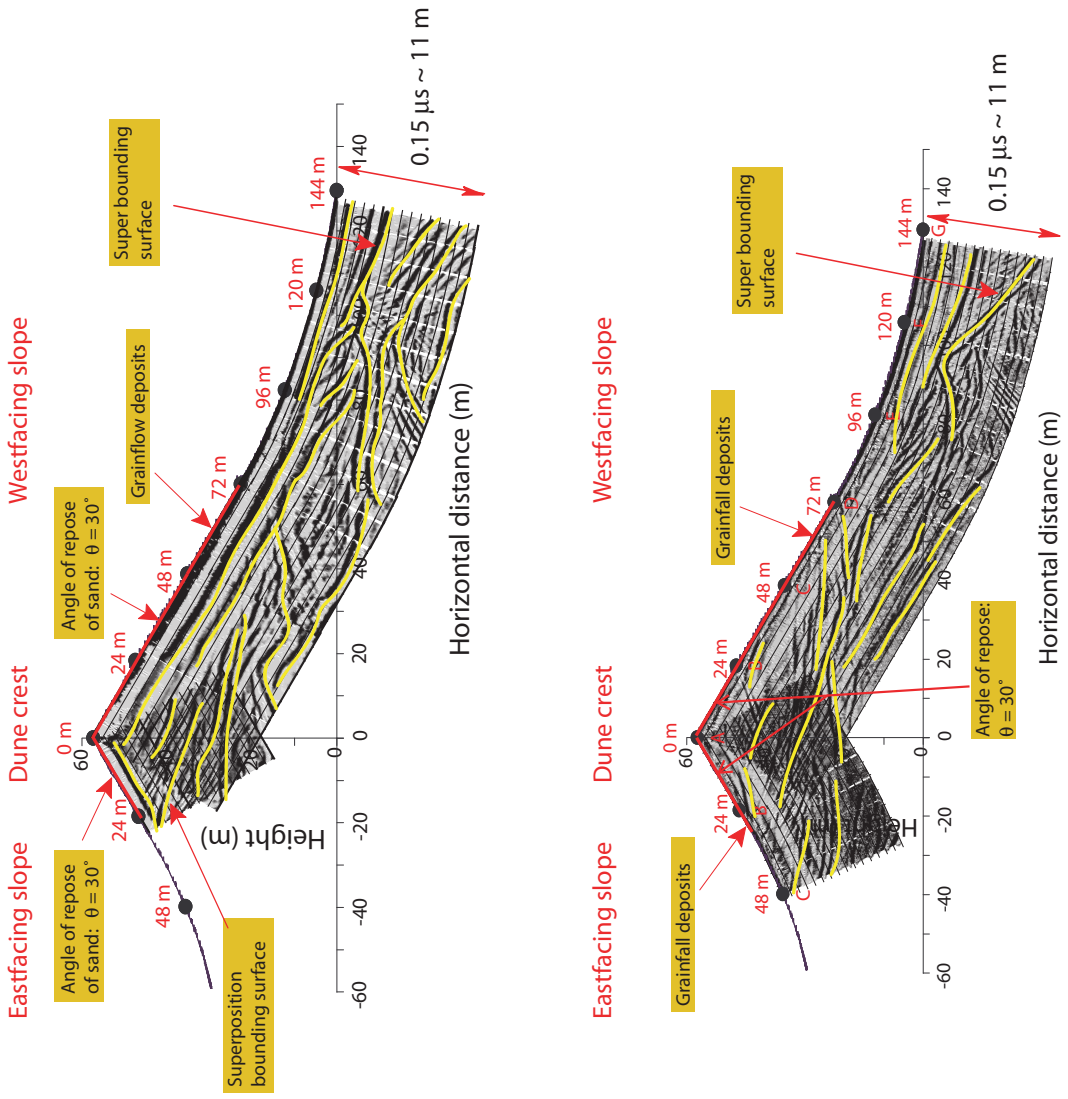

(a) 10/27/2007

(b) 07/17/2008

Figure 6.11: Stratigraphical structure of the Eureka dune measured with 200 MHz ground penetrating radar. The profile is scaled with the radar velocity such that the time coordinate is twice the spatial coordinate. The yellows lines follow the local reflection profiles and are added for interpretation.

a period of a year and concluded that changes in size distribution are gradual and have a seasonal variation. The crest samples are finer, better sorted and less skewed than samples from the dune base. If the grains originate from one population, the skewness value is close

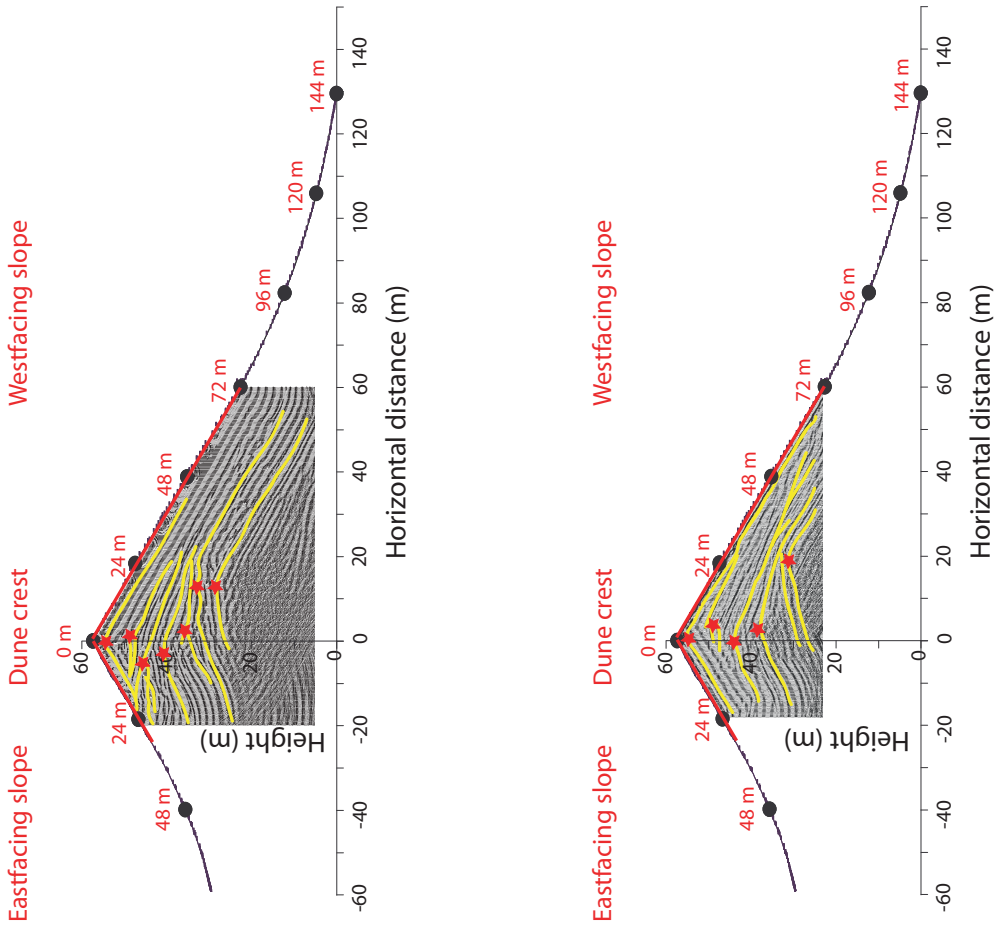

(a) Migrated 100 MHz profile

(b) Migrated 200 MHz profile

Figure 6.12: Kirchhoff migrated ground penetrating radar data of the Eureka dune on 10/27/2007 for 100 MHz and 200 MHz data.

to 0.0, the kurtosis value is close to 1.0 and sand may be approximated by a log-normal distribution with a characteristic average diameter and standard deviation (Flenley *et al.*, 1987). Analysis of surface samples taken from a Dumont dune at different positions from the crest (figure 6.13) shows that the average particle size is nearly constant along the dune,

but that the standard deviation increases strongly on the windward face and beyond 30 m from the crest on the leeward face. These results are in agreement with the trend of mean grain size as presented in Livingstone (1987).

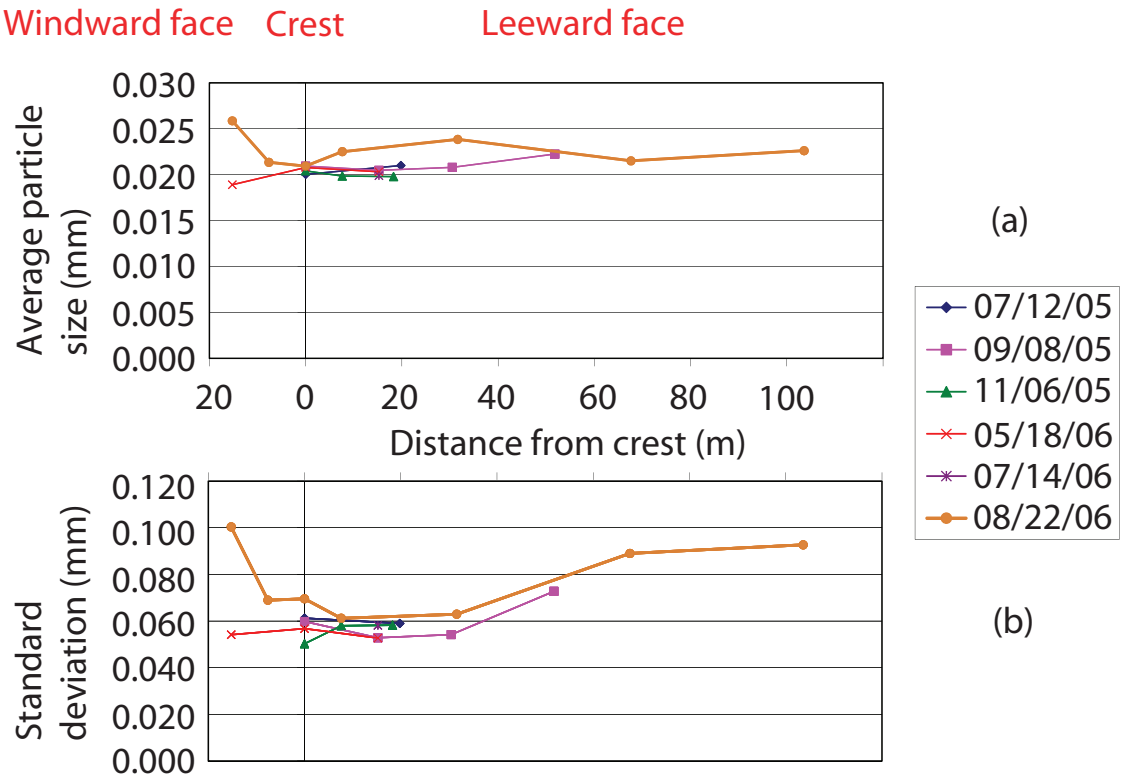

Figure 6.13: Particle characteristics of a surface sand sample from Dumont dunes: (a) Average particle size, (b) One standard deviation. The windward face of the dune is on the left-hand side of the crest, while the leeward face of the dune is on the right-hand side of the crest.

To obtain information on the grain sizes internal to the dune, a sampling probe slightly longer than 2 meters was designed and constructed to obtain samples from within the dune. The tip of the probe captures approximately 16 grams of sand at a certain depth that is locked in a air-tight container and brought to the laboratory for further analysis. The probe is inserted parallel to gravity and collects a sample perpendicular to the surface at a depth of $cos(30°)$ times the length of the probe. The moisture content, expressed as the percent by weight of a sediment sample (Namikas and Sherman, 1995), strongly increases with depth. In the summertime, the water content in sand is ∼0.1 % close to the surface and gradually increases to 1 % at a penetration depth of 1.75 meters. In the winter time, the moist (∼0.5

%) dune features a concentrated near-surface layer at a depth of 0.2 m with a high water content (2 %) and a wet (3 %) layer at a depth of approximately 1 meter. Experimental research reported in Namikas and Sherman (1995) indicates that surface moisture levels exceeding 1 % can significantly limit the sand transport due to increased cohesion between the sand grains.

A very hard, concrete-like, layer exists at the leeward face of the dune. The sampling probe cannot be forced further into the dune. Upon extraction of the probe, small conglomerates of sand are discovered the sample, as illustrated in figure 6.14. These conglomerates consist of approximately 5-10 sand grains across and are linked together with a binding glue. The connection does not disappear in water and the sand remains bonded. These conglomerates have been found for three different field dates when sufficiently deep samples were collected–on 07/12/2005 at a depth of 1.3 meters and 20 meters from the crest, on 09/08/2005 at a depth of 1.3 meters at 35 meters from the crest and on 07/16/2007 at a depth of 1.6 meters and 36 meters from the crest. Because of the discrete nature of the measurement, the extent of the layer and variation in depth between field dates is not known.

A scanning electron microscope analysis shows that the binding glue between individual grains is calcite $CaCO_3$ and dolomite $CaMg(CO_3)_2$, mixed with clay size particles. This mixtures forms layers between the grains binding a cluster of sand grains together. The cementation of the sand grains results in a decrease in porosity and a strong increase in velocity. Sand sampling at various depths shows that the strong sudden increase in velocity as observed in Vriend *et al.* (2007) is due to an abrupt occurrence of these conglomerates at a certain depth.

6.4 Discussion on the Stratigraphy

The calcium necessary for the cementation needs to be available at a depth of approximately 1.5 to 2 m from the dune surface. This calcium should be provided by dust, rain or from internal water flow. If the calcium would be provided with internal water flow, the capillary draw needs to be very strong to supply water from the ground level to a height of approximately 40 meters. Large bodies of free-surface water are not available for all booming dunes, although some dunes feature bordering large rivers (Golden Bell of Reso-

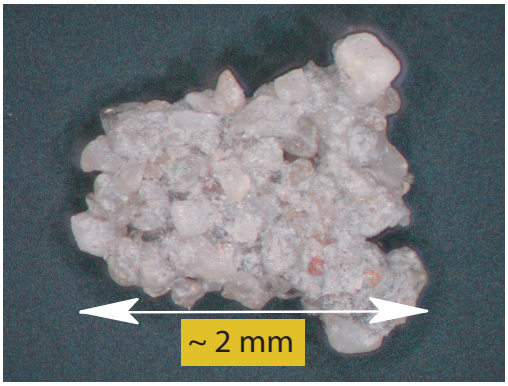

(a) Microscope picture

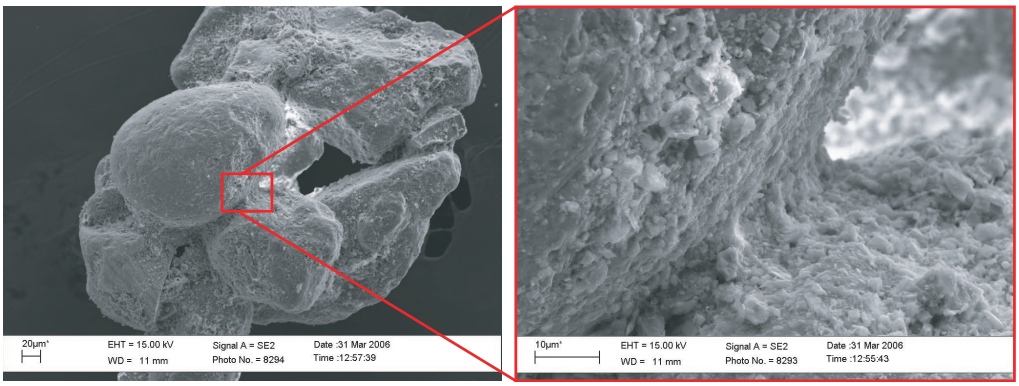

(b) Scanning Electroscope Method picture

Figure 6.14: Sand conglomerate obtained from a sample 1.3 m deep and 20 m from the crest on the leeward face at Dumont dunes on 07/12/2005.

nant Sand, near Shapotou, China) and interdune lakes (Badain-Jaran dunes, China Dong *et al.* (2003)). Precipitation may supply the minerals necessary for cementation and calcium is an important component in the precipitation in the Mojave Desert (∼8 mg/l in spring 2002, National Atmospheric Deposition Program). Another possibility is that desert dust provides the necessary calcium and is percolated into the dune by precipitation. Clay-sized particles are necessary for the creation of the bonding material, in addition to an excess calcium source. When precipitation percolates through the dune it supplies the minerals and clay-size particles needed for this process. Sand at the surface of the dune has shortage of clay-size particles (D = 0.001-0.0039 mm) present as deduced from sieving experiments and this particle size may have transported down into the dune.

Subsurface cementation has been reported in literature for various sediment types: including sandstone, subaqueous, aeolian and Antarctic dunes. MacKenzie (1964) recognized

strong bedding due to calcareous surface cementation in Bermuda sandstone. The author suggested that percolating rainwater induces rapid surface cementation, provides stabilization and preserves the structure. Slow stabilization leads to erosion and cross-bedding on the windward face of the dune, similar to the structure on the windward face of Dumont dunes. Flemming and Bartoloma (1995) collected core samples of sand in marine deposited dunes and observed strong cross-bedding and cementation at 1.9 and 3.0 m depth. The authors noticed that the cementation occurred after a layer has been buried below a critical thickness of sediments and does not form on the water-sediment interface. Dong *et al.* (2003) recognized cementation in large megadunes in the Badain-Jaran desert and argued that vegetation and cementation by calcium deposits promotes dune fixation. Subsurface ice-cemented layers in sand and snow Antarctic dunes may strongly influence the humidity balance between snow-melt and vapor transfer and fixate dunes temporarily (Calkin and Rutford, 1974).

The regular subsurface pattern on the windward face of the Dumont dune shows dipping layers close to the angle of repose. Closer to the desert floor on the windward face are a few intersecting layers that are oriented at a shallower angle. These second-order surfaces were formed when the dominant wind blew from a different direction, therefore creating a slipface at an oblique angle compared to the current topography (Kocurek, 1991). The individual layers are separated from each other with a spacing of approximately 2 meters. Figure 6.15a presents a discretization of the layers, in which the amplitude represents the strength of the layer in the GPR profile. Figure 6.15b provides an estimate of the relative annual precipitation. The raw data has been shared by Dr. Richard Hereford (USGS Flagstaff, Arizona) in personal communication and includes average precipitation records of 52 Mojave desert weather stations. The mid-century dry period between 1945 and 1977 is the most distinct feature in the precipitation records (Hereford *et al.*, 2006) and is linked to a section along the dune without significant layer formation.

The dune migrates approximately 1 meter a year based on the correlation between appearance of significant layering and large precipitation events. The weakness in the one-to-one comparison is that a constant migration speed may not be present. Wet years may freeze or slow the migration speed and not acceleration or deceleration is taken into account. A more accurate estimate of the migration rate, together with insights on the time-dependent feedback of precipitation on migration, may be obtained with carbon dating of sand samples

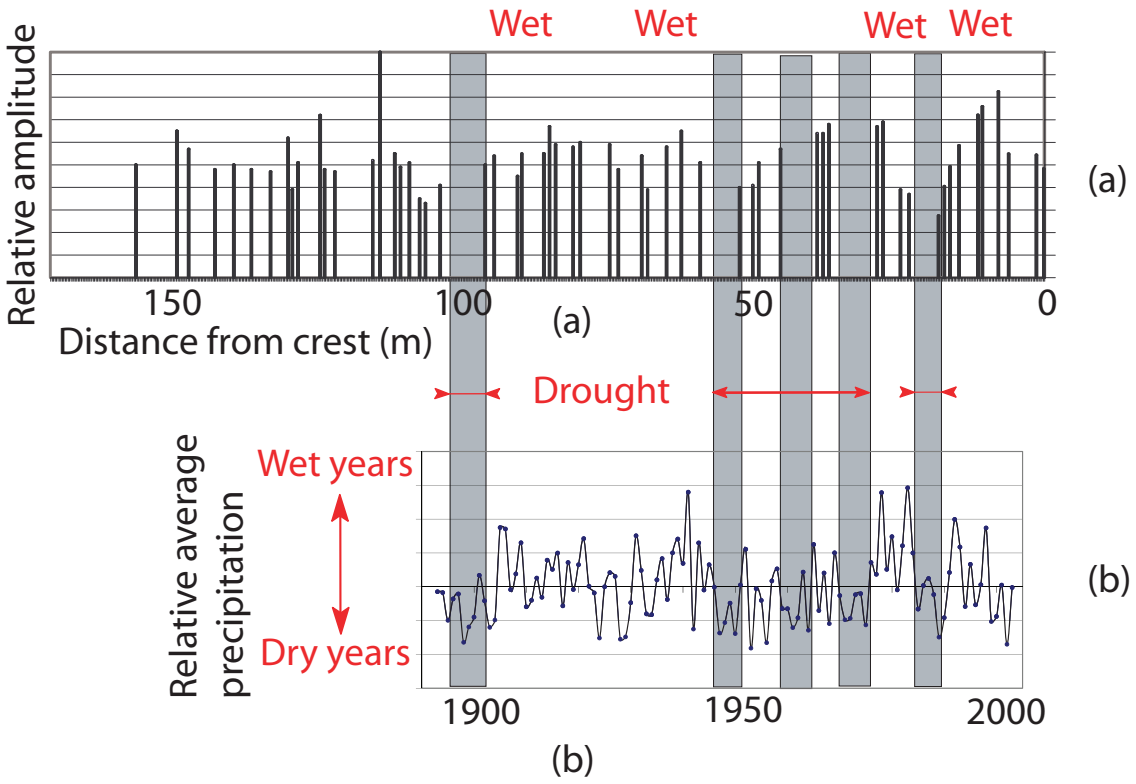

Figure 6.15: Correlation between layering and long-term precipitation: (a) Discrete representation of the layering on the windward face of Dumont dunes, (b) Relative annual precipitation for 1890-2000. Long term environmental data is collected from averaging precipitation records from 52 Mojave desert weather stations shared by Dr. Richard Hereford (USGS Flagstaff, Arizona) in personal communication.

in future work. The migration rate of 1 meter per year is the same order of magnitude that was obtained from satellite correlation in figure 6.5.

6.5 Near-surface Structure of a Dune

Figure 6.16 shows the near-surface section of the radar profiles for the four different field dates at Dumont dunes. The May 2007 profile shows that a layer materializes from the crest of the dune and continues to 33 meters where it dips down into the deeper sections of the dune. The September 2007 profile shows that the layering is deep and irregular close to the crest, but is well-defined and closer to the surface in a region from 27 to 48 meters from the crest after which it dips deeper into the dune. Furthermore, the strong radar reflection also appears slightly earlier in the record indicating a shallower layer in September. The

March 2008 data shows strongly tilting layers oriented at an angle steeper than the surface. The leeward face is at a shallower angle than usual (figure 6.3) and the crest is topped-off (figure 6.9) indicating that the original layering remains but is now in a tilted orientation with respect to the surface. The June 2008 profile shows a situation very similar to the May 2007 data, the constant layering occurs at the upper part of the dune, between 10 and 24 meters.

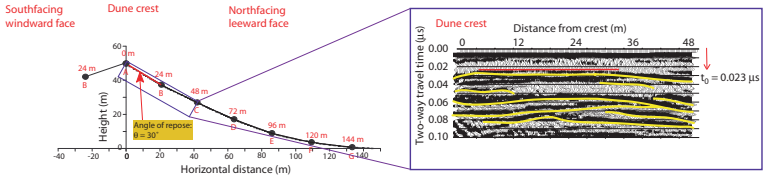

(a) 05/30/2007: near-surface layer from 4 to 33 meters

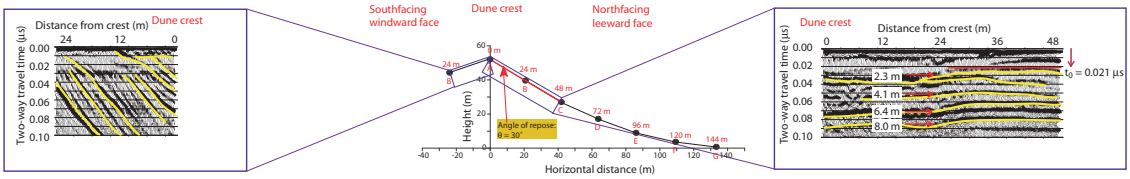

(b) 09/18/2007: near-surface layer from 27 to 48 meters

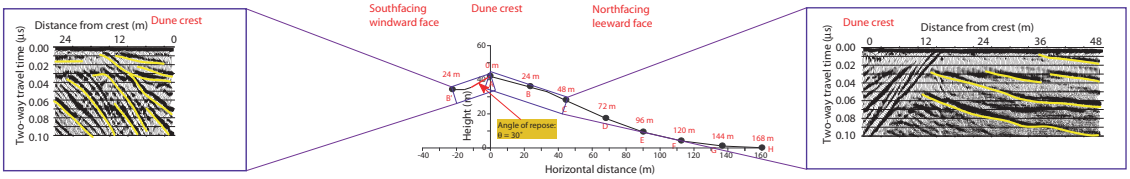

(c) 03/24/2008: strongly tilted layers penetrate to the surface

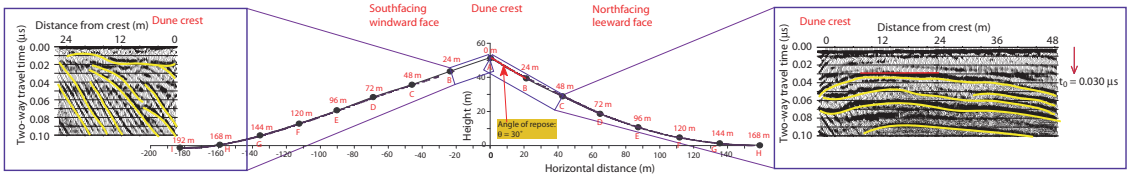

(d) 06/02/2008: near-surface layer from 10 to 24 meters

Figure 6.16: Detail of the subsurface structure of the Dumont dune system measured with a Ground Penetrating Radar survey at 200 MHz and superimposed on the topography. The windward face for all field dates show strongly tilted layers penetrating to the surface. The topography has not been measured directly on 09/18/2007 and 03/24/2008 and therefore a local interpretation of the topography is used as a framework for the radar results.

Figure 6.17 shows the near-surface section of the radar profiles for the two different field dates at Eureka dunes. The October 2007 profile shows a constant layering on both sides of the dune near the surface with tilted layering deeper in the dune. In contrast, the June 2008

data shows strongly tilted layering on both sides of the crest penetrating to the surface.

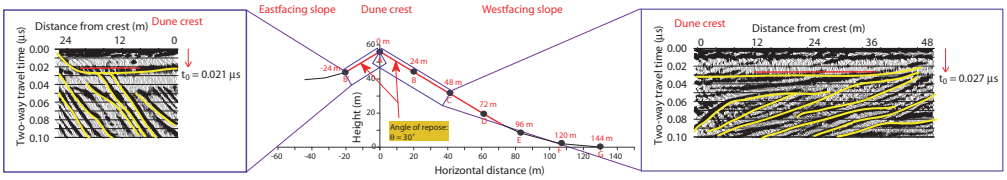

(a) 10/27/2007: near-surface layer on both faces with deeper tilted layers

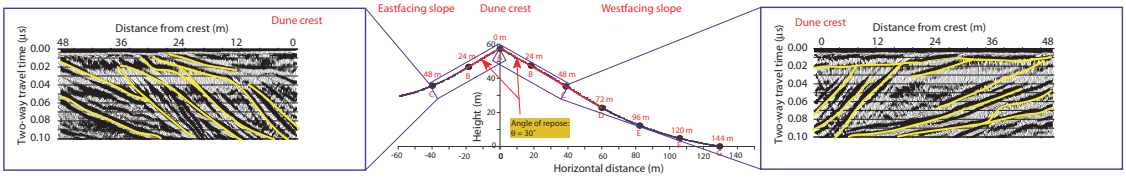

(b) 07/17/2008: strongly tilted layers penetrate to the surface

Figure 6.17: Detail of the subsurface structure of the Eureka dune system measured with a Ground Penetrating Radar survey at 200 MHz and superimposed on the topography. The topography has not been measured directly on 10/27/2007 and there a local interpretation of the topography is used as a framework for the radar results.

Table 6.1 summarizes the radar velocity V_r and two-way travel time t_0 measurements and calculates the distance to the first large reflector. The shortest distance from the surface to this subsurface layer H varies between different field dates. The error margins are obtained with an error of $\delta t = 0.0005\mu$s and $\delta V_r = 5.10^6$ m/s.

Table 6.1: Ground penetrating radar survey results at Dumont and Eureka Dunes, performed with the 200 MHz antenna.

Location & Date	Survey	V_r (m/s)	t_0 (s)	H $\pm$ δH (m)
Dumont & 05/30/2007	North face AG	$1.73.10^8$	23.10^{-9}	2.0 ± 0.10
& 09/18/2007	North face AG	$1.81.10^8$	21.10^{-9}	1.7 ± 0.10
& 03/24/2008	North face AG	$1.61.10^8$	tilted	–
& 06/02/2008	North face AH	$1.65.10^8$	30.10^{-9}	2.5 ± 0.12
Eureka & 10/28/2007	West face AH	$1.73.10^8$	27.10^{-9}	2.3 ± 0.11
& 10/28/2007	East face AB	–	21.10^{-9}	1.8 ± 0.10
& 07/18/2008	West face AG	$1.69.10^8$	tilted	–
& 07/18/2008	East face AC	–	tilted	–

6.6 Velocity Structure of a Dune

Vriend *et al.* (2007) investigated the compressional seismic velocities of the subsurface structure of dunes in detail with seismic refraction surveys and observed sharp jumps in velocity with depth and a strong lateral gradient in velocity in downhill direction. The wave propagation characteristics of the seismic refraction experiment have been analyzed in further detail in Vriend *et al.* (2010b). Both the body P- and S-wave and the surface Rayleigh wave are present in the shot record resulting from a broadband hammer impact. Waves are traveling from the impact source along an array of 48 geophones. The velocity increases as the waves penetrate deeper into the dune for the farthest sensors from the impact. An example of a shot record is presented in figure 6.18 for a field experiment at Dumont dunes on 05/29/2007. The refractive analysis shows a near surface layer of ∼180 ± 20 m/s on top of a faster layer of ∼300 ± 30 m/s which is on top of a fast half space of ∼350 ± 30 m/s. The

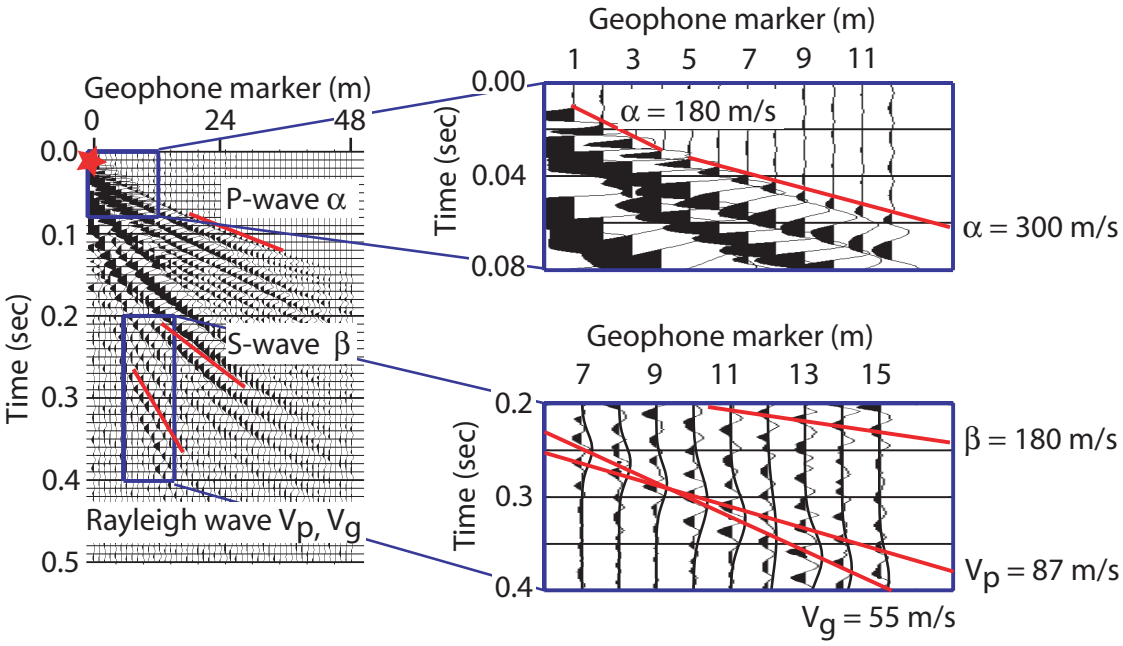

Figure 6.18: Shot record of the seismic refraction experiment of the Dumont Dune on 05/29/2007. The array of 48 geophones are laid out perpendicular from the crest in the direction of the base of the dune with a spacing of 1 meter. The impulse at position zero provides energy needed for the seismic refraction experiment. The first insert and second insert show details of the internal refraction of the first arrival P-waves, illustrated with distinct breaks in the slope.

dominant first arrival in the ground penetrating radar profile of 05/29/2007 (figure 6.16a) is the deeper layer that extends from the crest to 33 meters in downhill direction. The

surficial intermediate layer forming the first refraction (180 to 300 m/s) is only prevalent in the upper 10 meters of the dune and is weak in the shot record. Physically this intermediate layer represents the unfinished formation of a new cemented layer that will form the next parallel bedding in the migrating dune. As the structural changes of the sand within the layer have not been completed yet, the layer is not fully formed in the ground penetrating radar profile.

Combining the seismic velocity structure of the dunes with the ground penetrating radar profiles provide a comprehensive view of the subsurface structure. The Dumont May 2007 data (figure 6.19a) features an increasing seismic velocity and a thickening layered structure in downhill direction characteristic of grainflow processes. The Dumont September 2007 data (figure 6.19b) does not feature velocity data, but only ground penetrating radar profiles. The subsurface structure characteristic of grainfall processes as it thins in downhill direction. Figure 6.20a presents the seismic structure of December 2006 and the ground penetrating structure of March 2008 of the Dumont dune. The dune sand was noticeably moist for both cases. The velocity increased diffusively throughout the layer and no refraction horizons were discovered in the shot gather. The radar profiles shows strong cross-bedding parallel to the angle of repose and is reversed near at the crest. The Dumont dune in June 2008 (figure 6.20b) features an uniform seismic structure in downhill position. The seismic velocity is not measured but estimated beyond 24 m from the crest based on continuation of the profile. The radar profile shows a distinct subsurface layer that dips deeper close to the crest and further downhill.

Figure 6.21a features a near-surface parallel layering for the Eureka dune in October 2007. The seismic velocity increases downhill on the west-facing slope. The east-facing slope features a significant higher seismic velocity. Figure 6.21b shows the velocity and layering structure for the Eureka dune in July 2008. The radar profile illustrates the strongly tilted layering of the subsurface structure resulting in an irregular near-surface layering.

The environmental parameters such as precipitation, temperature and wind regime differ from day to day and therefore large differences in velocity and subsurface structure are observed.

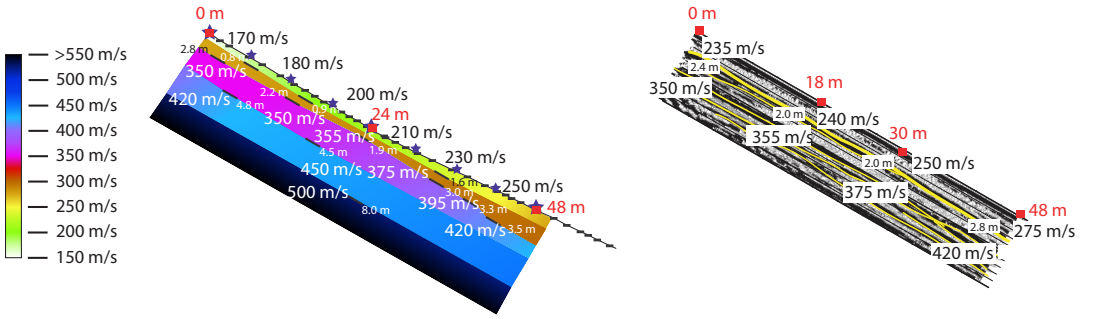

(a) Dumont dune on 05/29/2007

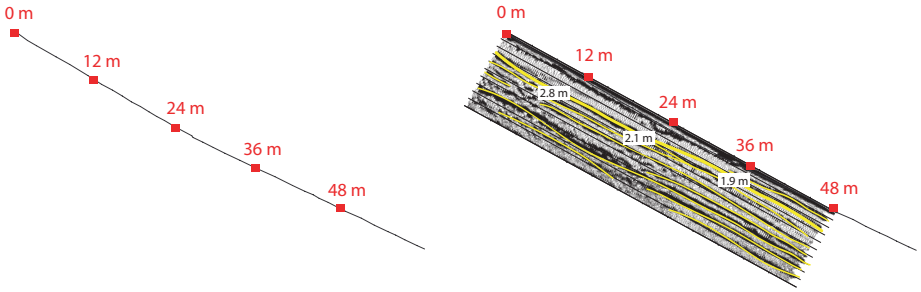

(b) Dumont dune on 09/17/2007

Figure 6.19: Near-surface velocity structure and internal layering of the Dumont dune during various field dates.

6.7 Conclusion

This study connects the internal structure of a Dumont and Eureka dune in the Mojave desert to environmental characteristics. The wind strength and direction influences the shape of sand dunes from season to season. The employment of ground penetrating radar is an efficient method to image the subsurface structure and provides a continuous interpretation of the dune stratigraphy up to a depth of 30 meters. Cross-bedding and regular layering, as revealed by ground penetrating radar surveys, are a direct result of grainfall, grainflow and other sedimentary processes in dune building dynamics. Subsurface sand sampling identifies a compacted and solidified layer at a depth of 1.5-2 meters. The layering occurs for the Dumont dune in a random pattern that correlates with large precipitation events providing direct evidence for the dune migration rate of approximately 1 meter per year.

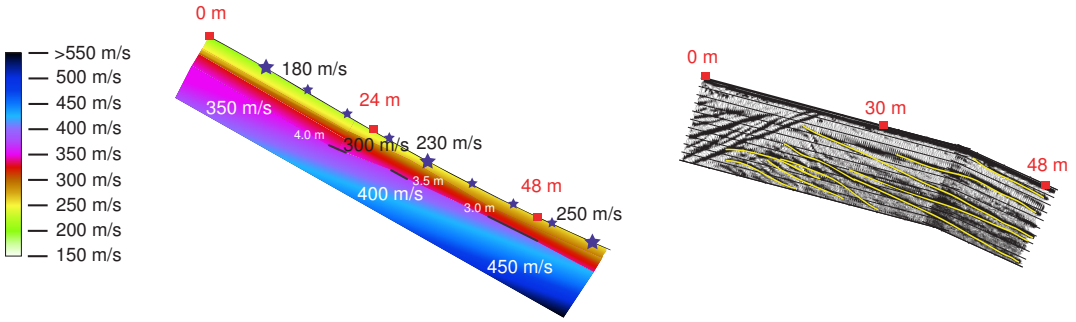

(a) Dumont dune on 03/24/2008 [a]

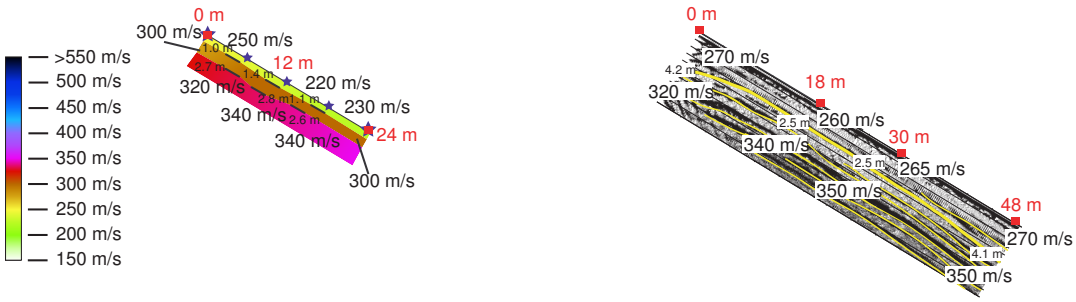

(b) Dumont dune on 06/01/2008

Figure 6.20: Near-surface velocity structure and internal layering of the Dumont dune during various field dates (continued). [a]: the velocity structure of Dumont on 03/24/2008 has not been measured. The velocity profile of the seismic refraction survey of 12/05/2006 has been used instead.

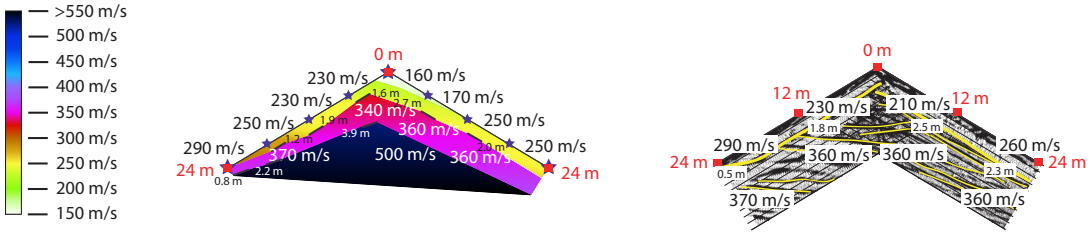

(a) Eureka dune on 10/27/2007

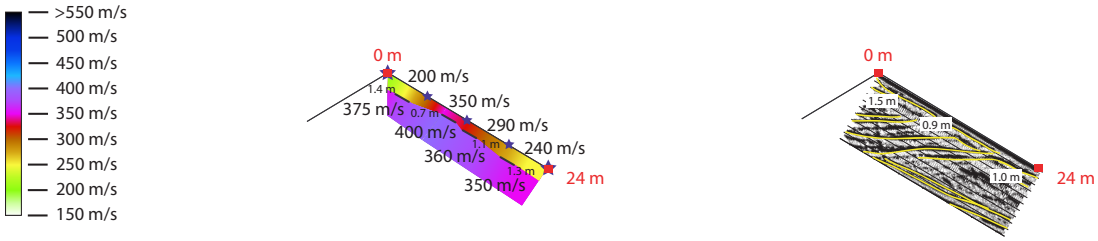

(b) Eureka dune on 07/17/2008

Figure 6.21: Near-surface velocity structure and internal layering of the Eureka dune during various field dates.

Chapter 7

Discussion

7.1 Summary

The following section is a summary of the results concerning dune migration and booming sand dunes. In this study field experiments on the acoustic emission of booming sand showed the following:

- Smooth and rounded aeolian grains, usually around $D = 0.2$ mm, may produce a small-scale brief acoustic emission upon shear or compression (figure 5.2b).
- These brief burping emissions are low amplitude with a broadband frequency (50-100 Hz) distribution (figure 2.4).
- The avalanching of a thin ($\sim$ 5 cm) surface layer down a slope at the angle of repose may produce a loud booming emission (figure 5.2a).
- These avalanches can be due to natural slumping (figure **??**) or induced sliding.
- Booming generates a dominant frequency (70-105 Hz) and several higher harmonics (figure 3.2a).
- The seismic and acoustic vibrations can continue for a minute after all visible shearing ceases (figure **??**).
- The natural resonance of the dune can on rare occasions be triggered by an impact source (figure 5.2c).
- Booming occurs only at select dunes in the world (table 1.1).

- Booming is strongly amplified: the sound is audible and vibrations are measurable at several kilometers distance (figure **??**).
- Booming is seasonal: an intense rainstorm silences the dune and booming only occurs in the dry season (figure **??**).
- Booming is regional: smaller neighboring dunes are silent (figure 3.2f).
- Booming is local: the frequency may change and the amplitude may subside in the downhill direction (figure **??**).

The booming frequency does not correlate directly with the amplitude of the emission, nor with the average particle size (figure **??**), nor with the method of initiation of the avalanche. The microphone recording of a booming slide on Eureka dune on 10/27/2007 presented in figure 7.1a shows a frequency drop from 87 to 79 Hz and increase again to 95 Hz for the later part of the slide. The booming starts after sliding for 5 seconds with a low amplitude vibration slowly growing with time. The actual active sliding stops after approximately 25 seconds, but the sound continues for another minute. The change in frequency is not directly correlated with amplitude, as illustrated in figure 7.1b. The amplitude of the booming has been represented with a sized dot and shows that the minimum in booming frequency is not at the same point in time as the maximum in amplitude. Therefore the booming frequency is not directly related to nonlinear effects in wave propagation, as this would relate the frequency directly with the amplitude.

Douady *et al.* (2006) performed laboratory experiments covering the brief acoustic emissions due to shearing and noticed that the sound frequency depends on the shear rate and the particle diameter of the sample. Vriend *et al.* (2010b) argued that these brief acoustic emissions are due to a local process at the grain scale and are fundamentally different from the booming emission. Vriend *et al.* (2007) compared the influence of the velocity of the slide on the booming frequency and found that the frequency did not change with velocity and therefore shear rate. Two natural wind-induced avalanche events recorded on 05/29/2007 and 09/17/2007 at the same Dumont dune are presented in figure 7.2. The acoustic signal has less energy than the induced slide due to the relative small slumping area. As the mechanism of sliding is in both cases due to gravity, the variation in frequency content suggests that the booming frequency varies between season and year and does not depend on method

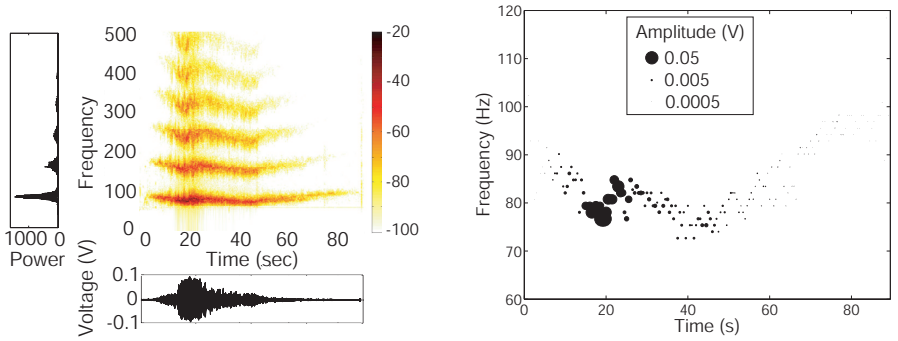

(a) High-quality microphone recording of the booming event

(b) Booming frequency as a function of time and amplitude

Figure 7.1: The high-quality microphone recording of the booming event on 10/27/2007 at Eureka dunes shows that the frequency varies in amplitude with time. The frequency has been discretized with a fast Fourier transform at an interval of 0.5 seconds. The amplitude has been plotted as the size of the data point and is multiplied by a factor of 300 for plotting purposes.

of initiation.

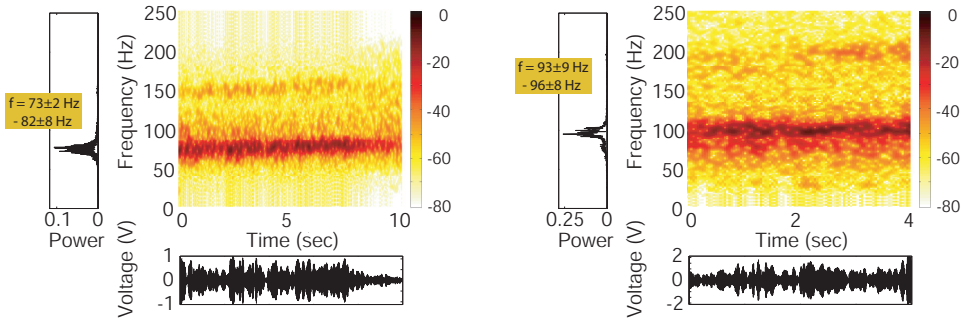

(a) 05/29/2007, frequency increases from f = 73 ± 2 Hz to f = 82 ± 8 Hz

(b) 09/17/2007, frequency increases from f = 93 ± 9 Hz to f = 96 ± 8 Hz

Figure 7.2: Spectrogram, signal and power spectrum of the recordings of natural avalanches induced by the wind on the large Dumont Dune (h = 45 m) in Mojave Desert, California, measured with a geophone at 24 meters from the crest. The frequency of the booming increased for both recordings as the natural avalanche progressed down the slope.

An assumption commonly made in literature (Andreotti, 2004; Douady *et al.*, 2006) is that the booming frequency f is a direct function of average particle size D. Vriend *et al.* (2007) showed that the frequency and average particle diameter do not correlate directly and not all characteristics of booming dunes are explained when the booming frequency is only a function of particle diameter. The average grain diameter does not change significantly

from field date to field date or in downhill position (Vriend *et al.*, 2010a), but the booming frequency may change dramatically. An extreme illustration of a large change in frequency, presented in figure 7.3, occurred on the Dumont dune on 05/18/2006. After 40 seconds in the recording the frequency abruptly shifts down from $f = 83\pm5$ to 69 ± 4 Hz. No physical change at the dune surface was observed and neither the local particle size (Vriend *et al.*, 2010a), nor the method of initiation changed during this transition. The geophysical measurements

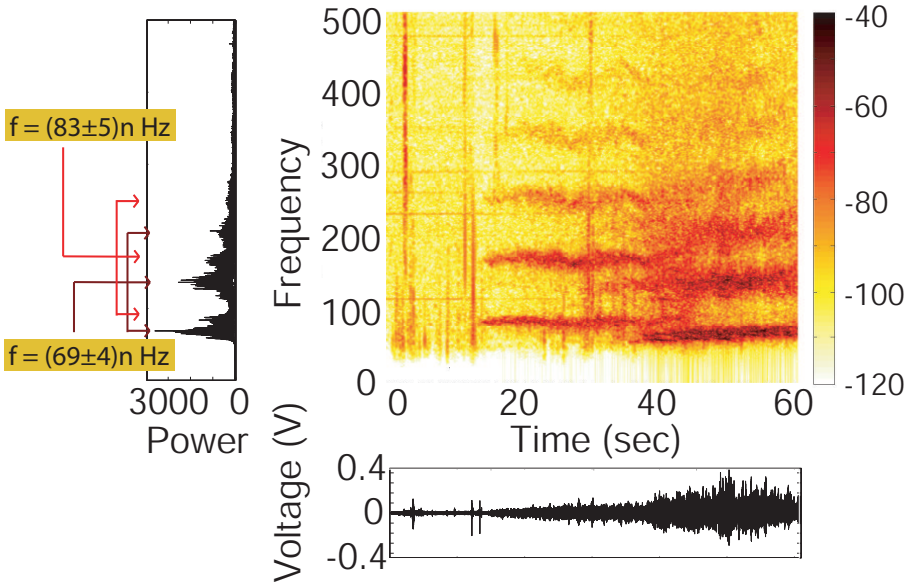

Figure 7.3: Spectrogram, signal and power spectrum of the microphone recording of the booming emission at 24 meters from the crest created by sliding down the slope of the Dumont dune on 05/18/2006. The booming frequency modulates and drops abruptly from 83 ± 5 to 69 ± 4 Hz half way through the slide.

on 05/18/2006 were limited to a coarse seismic refraction survey and covered only a limited amount of subsurface layering. The sparse data prevents an exact correlation between the frequency drop and the subsurface structure, but an internal change in the waveguide depth of $dH = 0.4m$ would provide the necessary conditions for the frequency shift.

Another common observation in studies (Criswell *et al.*, 1975; Haff, 1986) is that booming eliminates completely in high humidity environments or in rainstorms. Temperature and moisture are therefore environmental properties that influence of the occurrence of booming directly and may influence the booming frequency as well. Booming was easily generated during most field trips between May and September in the years 2003-2008, with measured

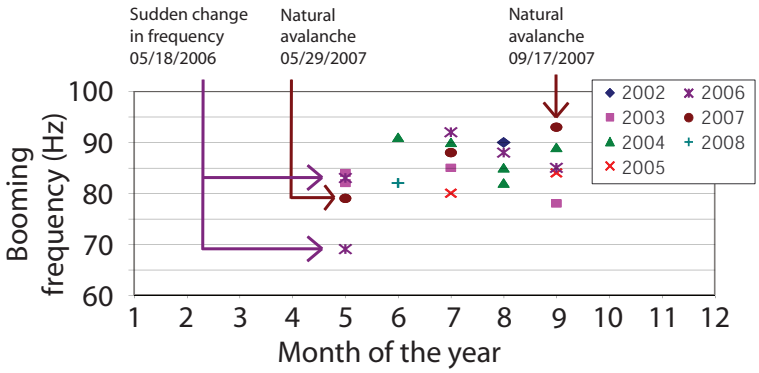

Figure 7.4: The booming frequency averaged over the recordings for one day for field trips in 2003-2008. The frequency data is obtained with microphone and/or geophone recordings of the sound. The measurement of the booming frequency on 05/29/2007 and 09/17/2007 were highlighted in Figure 7.2 highlights the measurement of 05/29/2007 and 09/17/2007 and figure 7.3 emphasizes the measurement on 05/18/2006.

booming frequencies varying between 69 and 93 Hz as illustrated in figure 7.4. During a few field trips at the edges of the field season, in September 2004, May 2005 and September 2007, booming was difficult to create but ultimately succeeded when creating the slide further downhill. Repeat visits to Dumont dunes in the winter time in November 2005, December 2006 and March 2008 showed that no acoustic emission could be initiated in situ, while the sand felt noticeably cold and moist. Although environmental factors such as humidity and temperature influence whether booming occurs, the total amount of precipitation does not directly correlate with the booming frequency. In this thesis, various geophysical methods are used to conduct an extensive study on the structure of the dune and its variation with time and space.

The migration of sand dunes results from a complicated interplay between dune building, wind regime and precipitation history. The dunes investigated in the current study, Eureka dunes in Death Valley National Park and Dumont dunes in the Mojave Desert, appear as different morphological and morphodynamical dune types. The Eureka dune is a longitudinal dune with two slipfaces at the angle of repose. The linear shape of the topography (figure 6.7) features an oscillating dune crest and ground penetrating radar surveys (figure 6.11) show strong cross-bedding with only a near-surface layer parallel to the surface. The Dumont dune is a transverse dune with one distinct leeward slipface and one windward shallow face. The crescentic shape of the Dumont dune topography (figure 6.3) predicts a net migration

rate in the northern direction. Ground penetrating radar surveys (figure 6.10) image the subsurface structure of the dune and feature a strong repetitive layering within the dune. The parallel layering at the angle of repose on the leeward face of the dune is a result of grainfall and grainflow depositional processes. The layering at the windward face is strongly tilted under the angle of repose and penetrates close to the surface.

Subsurface sampling provided sand samples from a very hard, concretelike layer at a depth of approximately 1.5 to 2 meters. The composition of the hard layer consisted of small conglomerates of sand grains (figure 6.14) cemented by calcite and dolomite. The existence of the discrete layer is a result of intense precipitation events (figure 6.15) and provides an image of the climatic history of the sand dune. Seismic refraction surveys (figure 6.19 through figure 6.21) illustrate discrete increases in velocity with depth across these interfaces and a gradual increase in downhill direction due to compaction. The seismic velocity structure of the dune correlates reasonably well with the ground penetrating radar experiments and confirms the position of the layering within the dune. The spacing between the individual layered subsurface structures correlates with the migration speed of the sand dune in a northern direction of the order of 1 meter per year (figure 6.11) and likely influences the stability in position of the Dumont sand dune.

The correlation between the observed near-surface structure (Vriend *et al.*, 2010a) and existence and characteristics of the booming phenomenon (Vriend *et al.*, 2010b) has been illustrated in figure 7.5 and figure 7.6. The Dumont May 2007 data (figure 7.5a) features an increasing seismic velocity, phase velocity (260 to 320 m/s) and booming frequency (78 to 83 Hz) in the downhill direction. The Dumont September 2007 data (figure 7.5b) also shows a strongly increasing booming frequency from 82 to 95 Hz in the downhill direction. The seismic velocities are not measured but estimated to perform a waveguide calculation. The estimate for $c_1 = 250$ m/s is based on the phase speed of booming (250 m/s) at 24 m from the crest and the estimate for $c_2 = 350$ m/s is chosen based on the mirror principle of $c_0 = c_2$. Figure 7.6a presents the seismic structure for the Eureka dune in October 2007. The seismic velocity increases downhill on the west-facing slope characterized by a phase speed of 210 m/s and a booming frequency of 84 Hz. The east-facing slope features a higher seismic velocity, a higher phase velocity (increasing from 230 to 450 m/s) and a lower booming frequency (76 Hz). The booming Dumont dune in June 2008 (figure 7.6b) features a uniform seismic structure in downhill position with a constant booming frequency at 83

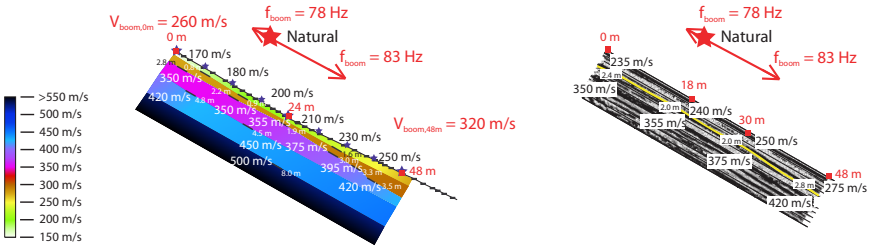

(a) Dumont dune on 05/29/2007: booming occurred between 8 and 30 m from the crest

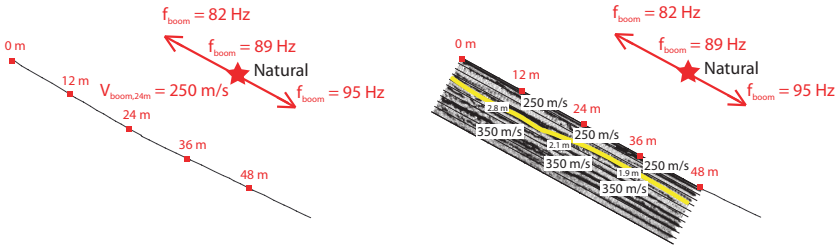

(b) Dumont dune on 09/17/2007: booming occurred between 20 and 48 m from the crest

Figure 7.5: Seismic structure of booming dunes at Dumont and Eureka. Superimposed on the seismic profile are the areas indicated where booming could be generated, the frequency and the phase velocity measured at the local geophones.

Hz. The phase velocity of booming is fairly high at 300 m/s. The seismic velocity is not measured but estimated beyond 24 m from the crest based on continuation of the profile.

Table 7.1 connects the experimental data with the theoretical predictions. The calculated and measured booming frequencies are presented in the third and fourth column of the table. The reduction of the error margins in the calculated frequency compared with (Vriend *et al.*, 2007) is largely due to the employment of ground penetrating radar to determine the dimensions of the waveguide. The results are able to correctly quantify the increase or decrease in booming frequency with downhill position due to the variations in subsurface structure.

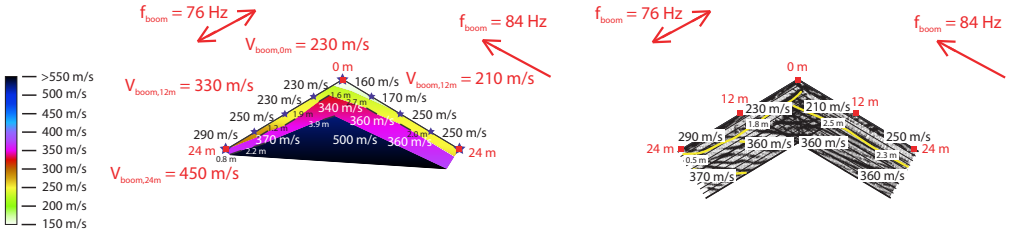

(a) Eureka dune on 10/27/2007: booming occurred from 16 m to 72 m from the crest on the west-facing slope and from 7 m to 18 m from the crest on the east-facing slope

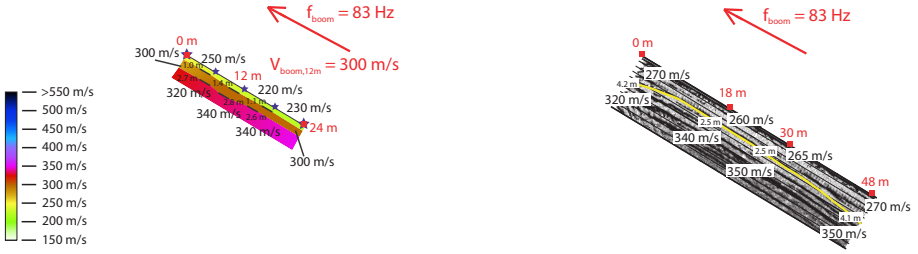

(b) Dumont dune on 06/01/2008: booming occurred from 6 m to beyond 24 m from the crest

Figure 7.6: Seismic structure of booming dunes at Dumont and Eureka (continued). Superimposed on the seismic profile are the areas indicated where booming could be generated, the frequency and the phase velocity measured at the local geophones.

The phase speed of booming shows large variations between different field dates–the phase speed at the crest varies between 180 and 260 m/s and strongly correlates with the seismic velocity of the top layer. The phase speed increases with downhill position, similar to the seismic speeds, up to 600 m/s at 100 m from the crest. The phase speed of booming attains a value between c_1 and c_2 and this is validated by the experimental phase speed data in table 7.1. The difference in measured and calculated phase speed is due to the calculation of phase speed V along the $c1$-$c2$ interface and the measurement of phase speed of the wave within the dry layer by geophones just beneath the surface.

The positive qualitative and quantitative correlation between the subsurface layering in the dune and the manifestation of the booming suggests an intimate relation between environmental factors and the booming emission. Booming occurs if three necessary factors are satisfied:

- Existence of a continuous source: smooth, rounded grains create short acoustic burping pulses when they are rubbed against each other.

- A sandwiched seismic velocity structure: a low-velocity surficial layer of sand between

Table 7.1: Waveguide and phase speed calculations.

Field measurement	Location: depth (m), c_1 (m/s), c_2 (m/s)	Frequency f (Hz)		Speed V (m/s)	
		Calc.	Meas.	Calc.	Meas.
Dumont dunes	0 m: 2.4, 235, 350	66 ± 12	no	325	260
Date: 05/29/2007	18 m: 2.0, 240, 355	81 ± 14	78 ± 7	355	–
Average frequency: 80 Hz	30 m: 2.0, 250, 375	84 ± 14	83 ± 4	355	–
	48 m: 2.8, 275, 420	65 ± 13	no	385	320
Dumont dunes	12 m: 2.8, 250, 350	64 ± 12	no	310	–
Date: 09/17/2007	24 m: 2.1, 250, 350	85 ± 16	85 ± 4	348	250
Average frequency: 90 Hz	36 m: 1.9, 250, 350	94 ± 18	95 ± 4	350	–
Eureka dunes, west	12 m: 2.5, 210, 360	52 ± 8	no	267	210
Date: 10/27/2007	24 m: 2.3, 260, 360	82 ± 16	84 ± 3	351	–
Average frequency: 84 Hz					
Eureka dunes, east	12 m: 1.9, 230, 350	80 ± 14	76 ± 8	350	330
Date: 10/27/2007	24 m: 0.5, 290, 370	–	no	370	450
Average frequency: 76 Hz					
Dumont dunes	0 m: 4.2, 270, 320	60 ± 21	no	304	–
Date: 06/01/2008	18 m: 2.5, 260, 340	81 ± 18	83 ± 4	340	300
Average frequency: 83 Hz	30 m: 2.5, 265, 350	81 ± 18	83 ± 6	350	–
	48 m: 4.1, 270, 350	52 ± 12	no	310	–

an air layer and a higher speed half space.

- A layering structure guiding the waves: the near-surface channel aligns traveling waves in a regular pattern.

The sandwiched seismic velocity structure in the layered near-surface channel creates a natural waveguide that promotes the amplification of the acoustic waves. The frequency of the booming is set by the condition for constructive interference in a waveguide and depends on the seismic speed and the width of the waveguide. The higher harmonics are expressed in terms of mode numbers as the wavelength increases for each overtone. The variation in internal layering and seismic structure determines whether booming occurs and explains the variation in booming frequency with downhill position. There are several conditions that result in the inability to generate booming or the elimination of sound:

- Diffuse velocity structure: e.g., the dune in the wetter season (figure 2.6c and figure A.2b). The gradual increasing velocity structure and the small difference in seismic speed across the interface brings the cutoff frequency beyond the maximum frequency of the source and booming cannot be excited by the burping emission.

- Short waveguide: e.g., a smaller dune (10 m high) in the same dune field (figure 2.6b and figure A.2a). The length of the waveguide channel is of the same order as the wavelength of booming and the symmetry between the half space and the atmosphere breaks down ($c_0 \neq c_2$).

- Shallow waveguide: e.g., in deposits of grainfall (figure 2.6d and figure 7.5b). The shallow depth brings the cutoff frequency beyond the maximum frequency of the source and booming cannot be excited by the burping emission.

- Deep waveguide: e.g., in deposits of grainflow (figure 7.6b). The wavelength for constructive interference exceeds the size of the source and the amplification is insufficient to sustain constructive interference.

- Tilted cross-bedding: e.g., on the windward face (figure A.2c). The waveguide depth is strongly varying in lateral direction and constructive interference cannot be initiated.

The necessary conditions for the booming emission to develop are only satisfied in a small selection of sand dunes in the world. As a result, booming is rare and continues to marvel travelers that journey unintentionally near booming sand dunes.

7.2 Future Perspective

There are several laboratory experiments (Haff, 1979; Hidaka *et al.*, 1988; Miwa *et al.*, 1995; Patitsas, 2008) that are able reproduce the sound generated from forced compression of sand. These experiments are able to obtain quantitative measurements of the high squeaking frequency of sand. X-ray photography (Hidaka *et al.*, 1988) indicates that the existence of shear bands and slip channels are necessary in the generation of sound. There are conflicting reports as to whether the velocity of the impact on the sand and the size of the object determine the squeaking frequency (Haff, 1979; Hidaka *et al.*, 1988) or that the mass of the object and the shear speeds in sand are influencing the frequency of the emission (Patitsas, 2008). Additional laboratory research should be able to identify the important parameters.

Other laboratory experiments (Douady *et al.*, 2006; Haff, 1979; Lewis, 1936) investigate sound emitted from the forced shearing of sand. The experiments include measurements of the burping frequency and sand characteristics and show that humidity and moisture affect the acoustic properties of the sand directly (Lewis, 1936). Experiments conducted

on a burping sample in an evacuated chamber of air show that air is not necessary for the creation and transmission of the sound. Douady *et al.* (2006) observe that neither the mass nor the velocity, but the mean shear determines the burping frequency that may vary greatly (25-250 Hz). The short burping emission also occurs in situ at the dune and has higher harmonics. Preliminary research indicates that the acoustic burping emission covers the even harmonics (n = 2,4,6,...) and the seismic burping emission also the odd harmonics (n = 1,2,3,...) as illustrated in figure 7.7. Extensive laboratory and field research should be conducted to parameterize the sound generation due to shearing.

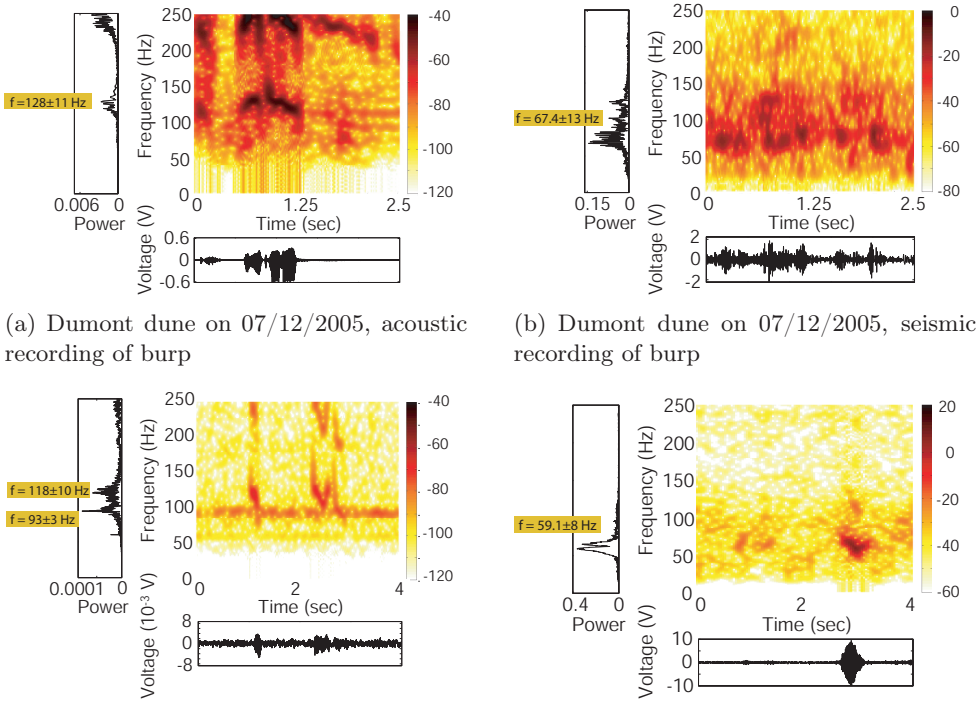

(a) Dumont dune on 07/12/2005, acoustic recording of burp

(b) Dumont dune on 07/12/2005, seismic recording of burp

(c) Eureka dune on 10/27/2007, acoustic recording of burp with remnant of booming emission at 93 Hz

(d) Eureka dune on 10/27/2007, seismic recording of burp

Figure 7.7: Discrepancy between acoustic and seismic recordings in the frequency of the burping emission.

Laboratory experiments measuring the sound emission due to slumping of sand are complicated because of scale issues. Acoustic emission from sand grains has been observed for particle sizes around $D = 0.2$ mm, but this size limits the scaling of the laboratory experiment. If the source at the surface can be reproduced in a scaled-down version of the dune, parameter studies could be conducted.

The research in this thesis presents extensive field measurements of the wave propagation of the booming emission, but additional work in situ may be performed to obtain additional insight into the dynamics. Buried sensors provide insight into the wave propagation with depth and would confirm that the booming wave travels throughout the surficial layer. Continuous imaging of the surface of the sand dune, for example with stroboscopic light at night, would expand the information on the wavelength and the propagation of the booming emission. A two-dimensional array of geophones positioned in a grid would provide information on the radial dispersion of the acoustic emission.

Numerical simulations of acoustic sand avoid the limitations of scaling encountered in laboratory and field experiments. A continuum model of the acoustic propagation in the dune would provide insight into the elastic wave propagation in the layered structure found in a desert dune. The granular properties could be incorporated in the continuum model by an alternative constitutive relation, but discrete element modeling would provide a more accurate picture of the interactions on the individual grain scale. The interaction of the two different scales is key in a comprehensive numerical model of the wave propagation of a sand avalanche on a desert sand dune.

In this thesis the geophysical field measurements, the ground penetrating radar and seismic surveys and the topography measurements and sand sampling results provided an unexpected insight into dune migration. The strong stratigraphical layering provides evidence of a long history of dune building. The continuous imaging of the subsurface structure of dunes with ground penetrating radar deserves more scientific attention. The combination of radar imaging, field observations and satellite correlation could become an important tool to quantify dune migration and to fight desertification of land areas.

Appendix A

Appendix

A.1 Booming Measurements

A.1.1 Field Expeditions

Table A.1 summarizes the measurements of each field trip.

A.1.2 Additional Seismic Data

Vriend *et al.* (2007) investigated the subsurface structure of a dune with seismic refraction experiments. The seismic surveys provide point measurements of the internal layering and do not provide a continuous profile of the layering within a dune. Ground penetrating radar (GPR) experiments provide a continuous measurement of discrete layers within a dune, but this survey type was not employed for all field experiments, as indicated in table A.1. Figure A.1 presents the seismic velocity structure for seismic surveys on booming dunes where exact layering profile has been obtained with GPR. Some of this data has been discussed and presented in Vriend *et al.* (2007). Table A.2 presents the waveguide calculations based on the seismic velocity and the waveguide depths obtained from the seismic surveys only. A large discrepancy between the measured and calculated frequency shows that the waveguide dimensions obtained with seismic surveys incorporate large errors.

Figure A.2a shows the velocity within a small (10 m) dune at Dumont that did not produce booming while the neighboring larger (45 m) dune did create booming. The smaller dune has a much shorter channel in longitudinal direction with a high deeper velocity influenced by the desert floor. The environmental parameters such as precipitation, temperature and wind regime are similar for large and small dunes in the dune field, but the large differ-

Table A.1: Overview of field trips to Dumont and Eureka dunes during field seasons 2006-2008. The first column indicates the location and the dates of the field trips. The second column explains whether booming could be generated and the range of peak frequencies measured with acoustic and seismic measurements. Note that the frequency changes with downhill position, resulting in possible large variations. The third, fourth, fifth and sixth column indicate if measurements were made covering [1] wave propagation characteristics of the acoustic emission, [2] estimated or measured topography of the slipface, [3] Ground Penetrating Radar surveys and/or [4] seismic refraction surveys.

Location & Date	Booming	Waves[1]	Laser[2]	GPR[3]	Seismic[4]
Dumont					
05/18/2006	North face	Yes	No	No	Yes
07/14/2006	North face (92 Hz)	Yes	No	No	Yes
08/22/2006	North face (82-88 Hz)	Yes	Yes	No	Yes
09/11-09/12/2006	North face (81-92 Hz)	Yes	Yes	No	Yes
12/05/2006	Burp (55 Hz)	Yes	No	No	Yes
05/29-05/30/2007	North face (77-85 Hz)	Yes	Yes	200 MHz	Yes
07/16/2007	North face (86-90 Hz)	Yes	No	No	Yes
09/17-09/18/2007	North face (87-93 Hz)	Yes	Est.	100, 200 MHz	No
03/24/2008	No boom nor burp	No	Est.	100, 200 MHz	No
06/01-06/02/2008	North face (83 Hz)	Yes	Yes	200 MHz	Yes
Eureka					
04/22/2007	No boom or burp	No	No	No	No
10/27-10/28/2007	West (84 Hz) face	Yes	Est.	100, 200 MHz	Yes
10/27-10/28/2007	East (75 Hz) face	Yes	Est.	100, 200 MHz	Yes
07/17-07/18/2008	Burp (68 Hz)	Yes	Yes	200 MHz	Yes

ence in velocity structure caused the inability for booming to create. Figure A.2b presents the seismic structure of the large Dumont dune in December of 2006 when the dune sand was noticeably moist. The velocity shows a diffusive increase in velocity (from 200 m/s to 350 m/s) without refraction horizons and clear internal layering. Figure A.2c shows the seismic velocity structure and the radar survey results of the Eureka dune in July 2008. The structure shows strongly tilted crossbedding with no constant waveguide layer.

A.2 Statistical Methods on Sand

A size classification is obtained from the logarithmic Wentworth grade ϕ scaling the sediment size:

$$\phi = -\frac{log(D)}{log(2)}, \tag{A.1}$$

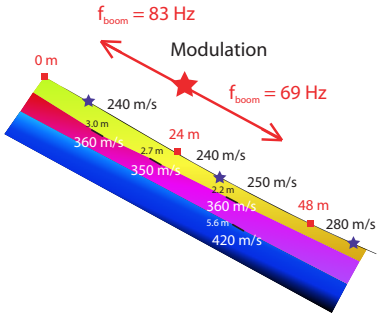

(a) booming large Dumont Dune (45 m high) on 05/18/2006

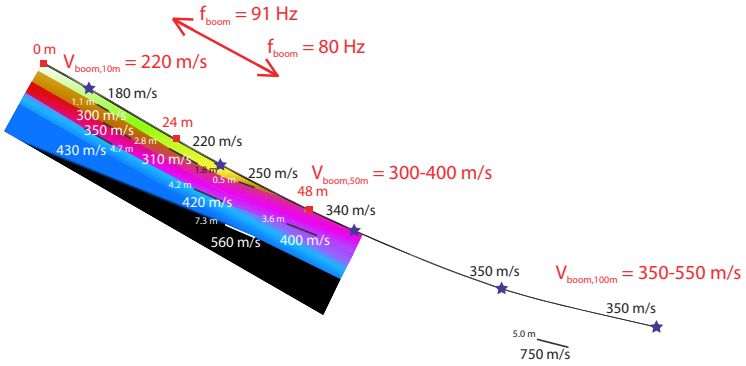

(b) booming Dumont dune (45 m high) on 08/22/2006

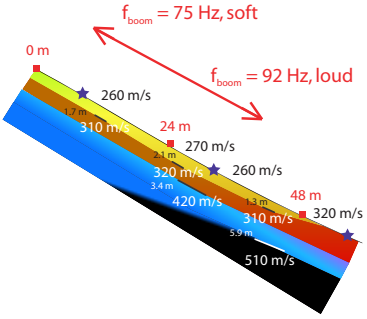

(c) booming Dumont dune (45 m high) on 07/14/2006

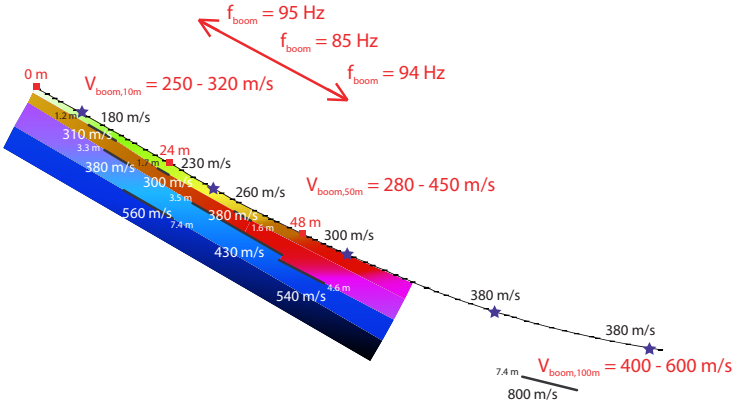

(d) booming Dumont dune (45 m high) on 09/12/2006

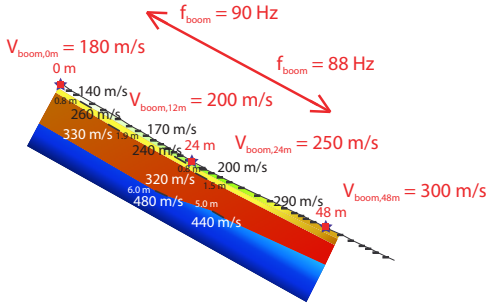

(e) booming Dumont dune (45 m high) on 07/16/2007

Figure A.1: Seismic structure of booming dunes at Dumont dunes. Superimposed on the seismic profile are the areas indicated where booming could be generated, the frequency and the phase velocity measured at the local geophones. The figure is to scale and plotted on topographic profiles with measured velocities and depths of interfaces, while the colors are added for interpretation.

with D the diameter of the sediment in millimeters (Wentworth, 1922).

Correlations for the four statistical parameters often used by soil engineers were devel-

Table A.2: Waveguide and phase speed calculations (continued).

Field measurement	Location: depth (m), c_1 (m/s), c_2 (m/s)	Frequency f (Hz)		Speed V (m/s)	
		Calc.	Meas.	Calc.	Meas.
Dumont dunes	12 m: 3.0, 240, 360	54 ± 13	83 ± 5	311	–
Date: 05/18/2006	24 m: 2.7, 240, 350	61 ± 16	69 ± 6	325	–
Average frequency: 75 Hz	36 m: 2.1, 260, 360	90 ± 24	no	360	–
Dumont dunes	12 m: 1.7, 260, 310	140 ± 56	75 ± 10	310	–
Date: 07/14/2006	24 m: 2.1, 270, 320	120 ± 47	92 ± 8	320	–
Average frequency: 90 Hz	36 m: 1.3, 270, 310	211 ± 101	no	310	–
Dumont dunes	12 m: 1.2, 180, 300	94 ± 25	91 ± 9	300	220
Date: 08/22/2006	24 m: 1.6, 200, 300	83 ± 24	80 ± 8	300	–
Average frequency: 85 Hz	36 m: 3.9, 250, 420	39 ± 10	none	287	–
	50 m: 3.6, 340, 400	–	none	400	300-400
	100 m: 5.0, 350, 750	–	none	415	350-550
Dumont dunes	12 m: 1.2, 180, 310	92 ± 24	95 ± 5	310	250-320
Date: 09/12/2006	24 m: 1.7, 230, 300	105 ± 34	85 ± 4	300	–
Average frequency: 88 Hz	36 m: 1.6, 260, 380	111 ± 29	94 ± 6	380	–
	50 m: 4.6, 300, 540	–	none	344	280-450
	100 m: 7.4, 380, 800	–	none	414	400-600
Dumont dunes	12 m: 1.9, 210, 330	72 ± 19	90 ± 5	298	200
Date: 07/16/2007	24 m: 1.5, 210, 320	93 ± 25	88 ± 3	320	250
Average frequency: 89 Hz	36 m: 1.9, 250, 320	105 ± 34	88 ± 3	320	–
	48 m: 2.0, 300, 340	–	none	340	300

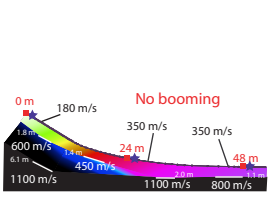

(a) small Dumont Dune (10 m high) on 09/11/2006

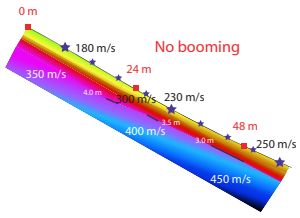

(b) large Dumont Dune (45 m high) on 12/05/2006

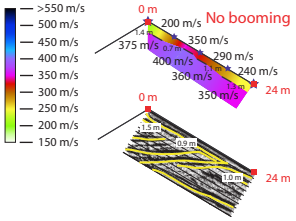

(c) large Eureka Dune (50 m high) on 07/17/2008

Figure A.2: Seismic structure of dunes without a constant velocity and structural layering close to the surface. The figure is to scale and plotted on topographic profiles with measured velocities and depths of interfaces, while the colors are added for interpretation.

oped by Folk and Ward (1957). Their graphic mean (μ), standard deviation (σ), skewness (γ) and kurtosis (κ) are defined in terms of the phi values $\phi_5, \phi_{16}, \phi_{25}, \phi_{50}, \phi_{75}, \phi_{84}, \phi_{95}$:

$$\mu = \frac{\phi_{16} + \phi_{50} + \phi_{84}}{3}, \tag{A.2}$$

$$\sigma = \frac{\phi_{84} - \phi_{16}}{4} + \frac{\phi_{95} - \phi_5}{6.6}, \tag{A.3}$$

$$\gamma = \frac{\phi_{84} + \phi_{16} - 2\phi_{50}}{2(\phi_{84} - \phi_{16})} + \frac{\phi_{95} + \phi_5 - 2\phi_{50}}{2(\phi_{95} - \phi_5)}, \tag{A.4}$$

and

$$\kappa = \frac{\phi_{95} - \phi_5}{2.44(\phi_{75} - \phi_{25})}. \tag{A.5}$$

The sediment may be classified based on mean size μ as illustrated in table A.3.

Table A.3: Classification of the size of sediments.

Wentworth grade	US standard sieve size	Diameter (mm)	Class
$\phi < -8$		> 256	Boulder gravel
$-8 < \phi < -6$	$>$ wire	64 - 256	Cobble gravel
$-6 < \phi < -2$	$>$ square	4 - 64	Pebble gravel
$-2 < \phi < -1$	5 - 10	2 - 4	Granule gravel
$-1 < \phi < 0$	10 - 18	1 - 2	Very coarse sand
$0 < \phi < 1$	18 - 35	0.50 - 1	Coarse sand
$1 < \phi < 2$	35 - 60	0.25 - 0.50	Medium sand
$2 < \phi < 3$	60 - 120	0.125 - 0.25	Fine sand
$3 < \phi < 4$	120 - 230	0.0625 - 0.125	Very fine sand
$4 < \phi < 8$	230 - pipette	0.0039 - 0.0625	Silt
$8 < \phi < 10$	pipette	0.001 - 0.0039	Clay
$\phi > 10$	pipette	< 0.001	Colloid

For the graphic standard deviation σ, the classification is given in table A.4.

σ-values in phi units	Class
$0 < \sigma < 0.35\phi$	very well sorted
$0.35\phi < \sigma < 0.50\phi$	well sorted
$0.50\phi < \sigma < 0.71\phi$	moderately well sorted
$0.71\phi < \sigma < 1.00\phi$	moderately sorted
$1.00\phi < \sigma < 2.00\phi$	poorly sorted
$2.00\phi < \sigma < 4.00\phi$	very poorly sorted
$4.00\phi < \sigma < \infty\phi$	extremely poorly sorted

Table A.4: Classification of the standard deviation of sediments.

The classification based on the graphic skewness γ is given in table A.5.

Lastly, the classification based on the graphic kurtosis κ is displayed in table A.6.

Table A.5: Classification of the skewness of sediments.

γ-values	Mathematically	Graphically
$1.00 > \gamma > 0.30$	strongly positive skewed	very negative phi values, coarse grained
$0.30 > \gamma > 0.10$	positive skewed	negative phi values
$0.10 > \gamma > -0.10$	near symmetrical	symmetrical
$-0.10 > \gamma > -0.30$	negatively skewed	positive phi values
$-0.30 > \gamma > -1.00$	strongly negatively skewed	very positive phi values, fine grained

Table A.6: Classification of the kurtosis of sediments.

κ-values	Class
$\kappa < 0.41$	extremely platykurtic, flat peaked
$0.41 < \kappa < 0.67$	very platykurtic
$0.67 < \kappa < 0.90$	platykurtic
$0.90 < \kappa < 1.10$	mesokurtic
$1.10 < \kappa < 1.50$	leptokurtic
$1.50 < \kappa < 3.00$	very leptokurtic
$3.00 < \kappa < \infty$	extremely leptokurtic, excessively peaked

A.3 Shape of Sand

The longest a, shortest c and, by assuming orthogonality, the intermediate b axis of the ellipse around a grain provide ratios of length $r_1 = b/a$ and $r_2 = c/b$. The resulting shape of the particle varies from equidimensional to disk shaped and from rod shaped to elongated. An eccentric grain has a low sphericity in both directions, as illustrated in table A.7.

Table A.7: Classification of sphericity.

Intermediate/Longest	Shortest/Intermediate	Class	Characteristic
$0 > r_1 > 0.66$	$0 > r_2 > 0.66$	Bladed	Elongated, flattened
$0 > r_1 > 0.66$	$0.66 > r_2 > 1$	Prolate	Rod shaped
$0.66 > r_1 > 1$	$0 > r_2 > 0.66$	Oblate	Disk shaped
$0.66 > r_1 > 1$	$0.66 > r_2 > 1$	Equant	Equidimensional

A.4 Theoretical Background: Wave Equation

The linear acoustic wave equation is structure independent and has a hyperbolic character. Combining the constitutive relation, Hooke's law, for an isotropic heterogeneous medium with Newton's second law results in:

$$c^2\phi_{xx} = \phi_{tt}, \tag{A.6}$$

with constant phase speed $c = c_0$ and the scalar quantity ϕ. The scalar quantity ϕ is usually either the normal pressure P or the particle displacement u.

For linear dispersive waves the phase information travels at a higher speed than the energy of the wave. The phase speed $c(k)$ depends on the wave number k as:

$$c(k) = \frac{\omega(k)}{k}, \tag{A.7}$$

with frequency $\omega(k)$. The group speed is the speed at which the energy of the wavelet travels and is defined by:

$$C(k) = \frac{d\omega(k)}{dk}. \tag{A.8}$$

The dispersion relation describes how the frequency $\omega(k)$ varies with wavenumber k. Substituting the dispersion relation in the wave equation produces the governing partial differential equation for linear dispersive waves. The dispersion relation is real if the PDE consists of solely even or solely odd derivatives. The dispersion relation for the linear Korteweg-de Vries (KdV) equation states:

$$\omega = c(k)k = c_0k - \nu k^3, \tag{A.9}$$

and leads to the following PDE:

$$c^2\phi_{xx} = \phi_{tt} + \nu\phi_{xxxx}. \tag{A.10}$$

The first term in the dispersion relation is due to the propagation of linear waves, while the second term describes the first nontrivial term of the dissipation in the Taylor expansion. Following Whitham (1974) and Nesterenko (2001) the form of the dissipation term is derived

by analyzing the integrodifferential equation for a right-traveling wave in one dimension:

$$\frac{\partial \phi(x,t)}{\partial t} + \int_{-\infty}^{\infty} K(x-\eta)\frac{\partial \phi(\eta,t)}{\partial \eta} d\eta = 0, \tag{A.11}$$

with a known Kernel $K(x)$ and a sinusoidal wavetrain as elementary solution $\phi = Aexp(i[kx - \omega t])$. As a simple case, resulting in a real dispersion relation, the phase velocity can be expanded with even coefficients as:

$$c(k) = c_0 + c_2 k^2 + ... + c_{2n} k^{2n}. \tag{A.12}$$

The first non-trivial term in this Fourier expansion is $c_2 k^2$, which is the leading-order term for the dispersion term in the KdV-equation, with $c_2 = -\nu$. The Kernel $K(x)$ is the Fourier transform of the phase velocity c(k) using the integrodifferential equation and the inversion theorem :

$$K(x) = \frac{1}{2\pi} \int_{-\infty}^{\infty} c(k) e^{ikx} dk, \tag{A.13}$$

resulting in:

$$K(x) = c_0 \delta(x) - c_2 \delta''(x) + ... + (-1)^n c_{2n} \delta^{2n}(x). \tag{A.14}$$

Substituting this Kernel into the integrodifferential equation yields the governing differential equation:

$$\frac{\partial \phi(x,t)}{\partial t} + c_0 \frac{\partial \phi(x,t)}{\partial x} - c_2 \frac{\partial^3 \phi(x,t)}{\partial x^3} + ... + (-1)^n c_{2n} \frac{\partial^{2n+1} \phi(x,t)}{\partial x^{2n+1}} = 0. \tag{A.15}$$

The first three terms describe the linear Korteweg-de Vries equation.

For a nonlinear wave, the components cannot be solved as a sum of independent variables and superposition does not apply. Weakly nonlinear waves include quadratic non-linearity terms and neglect cubic terms. In the non-linear wave equation, nonlinearity compensates the dispersion effect:

$$\phi_{tt} = c_0^2 \phi_{xx} + 2c_0 \gamma \phi_{xxxx} - \sigma \phi_x \phi_{xx}. \tag{A.16}$$

Transforming the nonlinear wave equation with $\eta = -\phi_x$ results in the nonlinear Korteweg-de Vries equation:

$$\eta_t + \left(c_0 + \frac{\sigma}{2c_0} \eta \right) \eta_x + \gamma \eta_{xxx} = 0. \tag{A.17}$$

An exact soliton solution of this equation describes the displacement η as:

$$\eta = Asech^2\left[\left(\frac{\sigma A}{24c_0\gamma}\right)^{1/2}(x - Vt)\right], \tag{A.18}$$

with amplitude A and soliton phase speed:

$$V = c_0 + \frac{\sigma}{6c_0}A. \tag{A.19}$$

The characteristic width of the soliton is:

$$L = \left(\frac{24c_0\gamma}{\sigma A}\right). \tag{A.20}$$

The important nonlinear characteristic is that the amplitude A linearly influences the phase speed V in the dispersion relation.

The phase speed c_0 and parameters γ and σ in this equation are determined using contact dynamics. Hertz's contact law relates the compressional force on spheres in a weakly compressed chain to the material and geometrical properties of the individual grains. A static force F_0 produces an initial displacement δ_0:

$$F_0 = \frac{2E}{3(1-\nu^2)}\left(\frac{R_1R_2}{R_1+R_2}\right)^{1/2}\left[(R_1+R_2)-(x_2-x_1)\right]^{3/2}, \tag{A.21}$$

with Young's modulus E, Poisson coefficient ν, and R_n and x_n the radius and coordinate of the center of grain n and the initial displacement between grains $\delta_0 = x_2 - x_1$. The phase speed c_0 and parameters γ and σ are expressed in terms of these geometrical properties:

$$c_0^2 = A\delta_0^{1/2}6R^2, \gamma = \frac{c_0R^2}{6}, \sigma = \frac{c_0^2R}{\delta_0}. \tag{A.22}$$

A.5 Reflection and Transmission Coefficients

The Rayleigh reflection coefficient for plane waves is:

$$R = \frac{\frac{\rho_2}{\rho_1} - \sqrt{\frac{\left(\frac{c_1}{c_2}\right)^2 - \left(\frac{c_1}{V_{\text{int}}}\right)^2}{1 - \left(\frac{c_1}{V_{\text{int}}}\right)^2}}}{\frac{\rho_2}{\rho_1} + \sqrt{\frac{\left(\frac{c_1}{c_2}\right)^2 - \left(\frac{c_1}{V_{\text{int}}}\right)^2}{1 - \left(\frac{c_1}{V_{\text{int}}}\right)^2}}}, \tag{A.23}$$

with phase speed along the interface $c_1 < V_{\text{int}} < c_2$ and:

$$V_{\text{int}} = \frac{c_1}{\sin(\phi_1)} = \frac{c_2}{\sin(\phi_2)} \tag{A.24}$$

The transmission coefficient T is related the reflection coefficient:

$$T = \sqrt{1 - R^2} = \frac{2\sqrt{\frac{\rho_2}{\rho_1}}\sqrt{\frac{\left(\frac{c_1}{c_2}\right)^2 - \left(\frac{c_1}{V_{\text{int}}}\right)^2}{1 - \left(\frac{c_1}{V_{\text{int}}}\right)^2}}}{\frac{\rho_2}{\rho_1} + \sqrt{\frac{\left(\frac{c_1}{c_2}\right)^2 - \left(\frac{c_1}{V_{\text{int}}}\right)^2}{1 - \left(\frac{c_1}{V_{\text{int}}}\right)^2}}}, \tag{A.25}$$

A.6 Methods and Materials

A.6.1 Moisture Content Measurement

To obtain information on the grain sizes internal to the dune, a sampling probe slightly longer than 2 meters was designed and constructed to obtain samples from within the dune. The tip of the probe captures approximately 16 grams of sand at a certain depth that is locked in a air-tight container and brought to the laboratory for further analysis. The probe is inserted parallel to gravity and collects a sample perpendicular to the surface at a depth of $cos(30°)$ times the length of the probe. In the preparation stage, the container has been

dried in the oven and weighted without content. The samples are processed within a few days after the return in the laboratory and are weighted first to obtain the total weight of the container and the sand sample. The sample is dried overnight for 24 hours at 110° C after which the total weight is measured again. The difference between the total sample weight and the dry weight divided by the dry weight determines the moisture content. The error on the scale is 0.01 gram, the container weight is ~ 50 gram and the sample weight is ~ 20 gram.

A.6.2 Sieve Analysis

Sieve analysis measures the particle-size distribution of a small (25 to 50 grams) sample of sand. The sample is dried in the oven to eliminate any cohesion due to moisture. The sample of known weight passes through a set of sieves with known mesh sizes arranged with downward decreasing mesh diameter. A stack of $4\sqrt{2}$ series sieves, with mesh sizes 28, 32, 35, 42, 48, 60, 65, 80, 100, 115, 150, covers fine to coarse sand and is most appropriate for the investigation of dune sand. The sieves are vibrated mechanically for a fixed period of time and the individual fractions are collected and weighted. The weight fractions are collected for each mesh size. The cumulative frequency distribution is obtained by plotting the "percent by weight finer" versus "grain size". The "percentage finer" is the fraction of the sample that has a smaller mesh size than the given fraction. The logarithmic probability representation resembles approximately a straight line. The statistical program "R" (the R foundation for statistical computing) is used to obtain a best fitting straight line from which an average diameter and a standard deviation of the sample is obtained. The error on the scale is 0.01 gram, the container weight is ~ 50 gram and the sample weight is ~ 20 gram.

A.6.3 Acoustic Analysis

The booming sound was recorded with a Tascam DA-P1 digital audio tape recorder and an Audio-technica AT 825 microphone. The booming emission is recorded at a sample rate of $f_s = 44100Hz$ that is sampled down in post processing to $f_s = 11025Hz$ to increase the processing speed. The data is analyzed with a fast Fourier transform code in Matlab. A Chebyshev fourth-order high-frequency filter with a passband ripple of 0.2 dB and a cutoff frequency of 60 Hz has been applied to filter out the low-frequency noise.

A.6.4 Seismic Refraction Survey

The fine-scale seismic refraction survey was executed with two linked 24-channel RAS-24 Exploration Seismographs with 48 one-component geophones. These geophones were separated 1 meter apart and could be positioned in two deployments totaling to 96 geophones. The pressure impulse to the geophones is induced by hitting a large mallet on a plate. Pressure impulses are given at a predetermined intervals. Data is acquired for 1 second at a sampling rate of 1000 Hz. The data is analyzed with the seismic data processing system SECO-ISIS producing seismographs.

A reduced seismograph is obtained by transforming all geophones output signals with the reduced time $t_{red} = t_0 - \frac{x}{V_{red}}$. Linear move-out (LMO) is applied resulting in reduced seismographs to determine the refraction velocities of the layers. Seismic waves traveling with a reduced velocity V_{red} form a horizontal line of first-arrivals and determine the refraction velocity of a specific layer n. The error-margin on the velocity measurement depends on the magnitude of the velocities and the amount of geophones captured in the refraction. This picking uncertainty is determined at ∼20 m/s for $V < 300$ m/s, ∼30 m/s for $300 < V < 400$ m/s, and ∼40 m/s for $400 < V < 500$ m/s.

The booming frequency is also recorded with the two 24-channel RAS-24 systems. Two different geophone array set ups are used to investigate properties of the booming emission, as illustrated in figure 5.3. An array of 48 geophones in a straight line downhill are used to investigate the development of the booming sound over time and space. An array of 12 geophones in a straight line parallel to the crest are used to perform high accuracy measurements of the phase speed of booming. A three-component geophone is connected to the RAS system to measure the displacement in three directions. The booming has been recorded for different sampling frequencies f_s: for 32 sec at $f_s = 500Hz$, for 4 sec at $f_s = 4000Hz$ or for 2 sec at $f_s = 8000Hz$. The data is analyzed with a fast Fourier transform code in Matlab. A Chebyshev fourth-order high-frequency filter with a passband ripple of 0.2 dB and a cutoff frequency of 20 Hz has been applied to filter out the low-frequency noise. The geophones have a natural frequency of 10 Hz according to the manufacturer specifications.

A.6.5 Ground Penetrating Radar survey

Ground penetrating radar (GPR) is based on the propagation of electromagnetic waves. The relative permeability determines the propagation velocity and the magnetic permeability and electrical conductivity influences the amplitude and attenuation of the waves (Baker *et al.*, 2007). GPR is most efficient in a medium with low conductivity and low-loss material properties. The contrast in a radargram is due to the reflection of waves off interfaces with large changes in radar velocity. The relative dielectric properties of a material influences the radar velocity directly.

Ground penetrating radar experiments are performed with a PulseEkko 100 system. The antennas are oriented perpendicular to the local slope. The separation distance and antennae length for the 100 MHz antennae are 1 meter and for the 200 MHz antennae 1/2 m. Data is collected every 0.25 m along a linear path and is obtained by stacking 8 measurements at each point. The radar velocity V_r is obtained from a common-midpoint (CMP) survey centered around a point 24 meters on the leeward face of the dune. The transmitter and receiver antenna are separated for each measurement by 1 m. The radar velocity depends on the dielectric material properties and may change slightly between different field dates. Only reflections and no refractions are expected because of the decrease in radar velocity with depth (Reynolds, 1997).

The data is converted such that it can be read with the seismic data processing system SECO-ISIS. The error margin on the radar travel time is ± 0.0005 μs and the error on the radar velocity is $\pm 5.10^6$ m/s.

Bibliography

B. Andreotti (2004). The song of dunes as a wave-particle mode locking. *Physical Review Letters* **93** (23), 238001/1–238001/4.

B. Andreotti and L. Bonneau (2009). The booming dune instability. *personal communication* , 1–4.

B. Andreotti, L. Bonneau, and E. Clement (2008). Comment on solving the mystery of booming sand dunes. *Geophysical Research Letters* **35**, L08306.

R. Bagnold (1941). *The physics of blown sand and desert dunes*. Dover Publications.

R. Bagnold (1954). Experiments on a gravity-free dispersion of large solid spheres in a newtonian fluid under shear. *Proceedings of the Royal Society of London, Series A - Mathematical and physical sciences* **225** (1160), 49 – 63.

R. Bagnold (1966). The shearing and dilatation of dry sand and the "singing" mechanism. *Proceedings of the Royal Society of London, Series A - Mathematical and physical sciences* **295** (1442), 219 – 232.

G. Baker, T. Jordan, and J. Pardy (2007). An introduction to ground penetrating radar (gpr). *GSA special paper: Stratigraphic analyses using GPR* **432**, 1–18.

P. Barnard, D. Hanes, D. Rubin, and R. Kvitek (2006). Giant sand waves at the mouth of san francisco bay. *Eos transactions, Americal Geophysical Union* **87**, 285–289.

W. Bollaert (1851). Observations on the geography of southern peru. *The Journal of the Royal Geographical Society of London* **21**, 99–130.

H. Bolton (1889). Researches on musical sand in the hawaiian islands and in california. *Transactions of the New York Academy of Sciences* **10**, 28–35.

H. Bolton and A. A. Julien (1888). The true cause of sonorousness in sand. *Transactions of the New York Academy of Sciences* **8**, 9–10.

L. Bonneau, B. Andreotti, and E. Clement (2007). Surface elastic waves in granular media under gravity and their relation to booming avalanches. *Physical Review E* **75**, 016602.

L. Bonneau, B. Andreotti, and E. Clement (2008). Evidence of rayleigh-hertz surface waves and shear stiffness anomaly in granular media. *Physical Review Letters* **101**, 118001.

C. Bristow, S. Bailey, and N. Lancaster (2000). The sedimentary structure of linear sand dunes. *Nature* **406** (6791), 56–59.

C. Bristow, G. Duller, and N. Lancaster (2007). Age and dynamics of linear dunes in the namib desert. *Geology* **35** (6), 555 – 558.

P. Brownell (1977). Compressional and surface waves in sand - used by desert scorpions to locate prey. *Science* **197** (4302), 479–482.

J. Buick, J. Chavez-Sagarnaga, Z. Zhong, J. Ooi, Pankaj, D. Campbell, and C. Greated (2005). Investigation of silo honking: Slip-stick excitation and wall vibration. *Journal of Engineering Mechanics* **131** (3), 299–307.

R. Burton (1879). Itineraries of the second khedivial expedition. *The Journal of the Royal Geographical Society* **49**, 17.

P. Calkin and R. Rutford (1974). The sand dunes of victoria valley, antarctica. *Geographical Review* **64** (2), 189–216.

C. Carus-Wilson (1888). Musical sands. *Bournemouth Society of Natural Science* .

C. Carus-Wilson (1890). Musical sands. *Nature* **42**, 568.

J. Clark (1990). *Beaches of Kaua'i and Ni'ihau*. University of Hawai'i Press, Honolulu.

D. Criswell and J. Lindsay (1974). Thermal moonquakes and booming sand dunes. *Abstracts of the Lunar and Planetary Science Conference* **5**, 151.

D. Criswell, J. Lindsay, and D. Reasoner (1975). Seismic and acoustic emissions of a booming dune. *Journal of geophysical research* **80** (35), 4963–4974.

C. Darwin (1835). *Northern Chile and Peru: In The Voyage of the Beagle.* reprinted in 1979 by Dutton, New York.

Z. Dong, T. Wang, and X. Wang (2003). Geomorphology of the megadunes in the badain jaran desert. *Geomorphology* **60** (1-2), 191 – 203.

S. Douady, A. Manning, P. Hersen, H. Elbelrhiti, S. Protière, A. Daerr, and B. Kabbachi (2006). The song of the dunes as a self-synchronized instrument. *Physical Review Letters* **97** (1), 018002/1–018002/4.

C. Doughty (1888). *Travels in Arabia Deserta Vol. 1.* University Press Cambridge.

W. Ewing, W. Jardetzky, and F. Press (1957). *Elastic waves in layered media.* McGraw-Hill New York.

B. Flemming and A. Bartoloma (1995). *Tidal signatures in modern and ancient sediments.* Blackwell Science, Oxford.

E. Flenley, N. Fieller, and D. Gilbertson (1987). The statistical analysis of "mixed" grain size distributions from aeolian sands in the libyan pre-desert using log skew laplace models: in desert sediments: Ancient and modern .

R. Folk and W. Ward (1957). Brazos river bar – a study in the significance of grain size parameters. *Journal of Sedimentary Petrology* **27**, 327–354.

L. Giles (1915). *Tun Huang Lu.* Journal of the Royal Asiatic Society of Great Britain and Ireland.

D. Goldsack, M. Leach, and C. Kilkenny (1997). Natural and artificial "singing" sands. *Nature* **386** (6620), 29.

D. Goldsack, M. Leach, C. Kilkenny, N. Belzile, and F. Ford (1998). Studies on the structure of the surface of acoustically emitting sands from barking sands beach, kauai, hawaii. *14th International AE symposium and 5th AE World Meeting* .

G. Grandjean, P. Paillou, P. Dubois, T. August, N. Baghdadi, and A. J. (2001). Subsurface structures detection by combining l-band polarimetric sar and gpr data: example of the pyla dune (france). *IEEE transactions on geoscience and remote sensing* **39** (6), 1245–1258.

R. Greeley, D. Blumberg, A. Dobrovolskis, L. Gaddis, J. Iversen, N. Lancaster, K. Rasmussen, R. Saunders, S. Wall, and B. White (1995). Potential transport of windblown sand: influence of surface roughness and assessment with radar data: in desert aeolian processes .

R. Greeley and J. Iversen (1985). *Wind as a geological process*. Cambridge University Press.

P. Haff (1979). Booming sands of the mojave desert and the basin and range province, california. *Caltech internal report* , 1–26.

P. Haff (1986). Booming dunes. *American scientist* **74** (4), 376–381.

K. Hagey and B. Hope (2008). Symphony of sand. The National Newspaper of UAE.

B. Hardin and F. Richart (1963). Elastic wave velocities in granular soils. *Journal of the Soil Mechanics and Foundations division* **89** (SM1), 33 – 65.

W. Harding King (1912). Travels in the libyan desert. *The Geographical Journal* **39**, 134.

R. Hereford, R. Webb, and L. C.I. (2006). Precipitation history and ecosystem response to multidecadal precipitation variability in the mojave desert region 1893 - 2001. *Journal of Arid Environments* **67**, 13–34.

J. Hidaka, S. Miwa, and K. Makina (1988). Mechanism of generation of sound in shear flow of granular materials. *International Chemical Engineering* **28**, 99–107.

M. Holliday (1976). *Nevada official bicentennial book*. Nevada Publications Las Vegas.

P. Hoye (1965). North from jiddah: in arabia the beautiful. Saudi Aramco World.

D. Humphries (1966). The booming sand of korizo, sahara and the squeaking sand of gower, s. wales: a comparison of the fundamental characteristics of two musical sands. *Sedimentology* **6**, 135–152.

M. Hunt and N. Vriend (2010). Booming sand dunes. *Annual Review of Earth and Planetary Sciences* **38**.

M. Hunt, R. Zenit, C. Campbell, and C. Brennen (2002). Revisiting the 1954 suspension experiments of r.a. bagnold. *Journal of fluid mechanics* **452**, 1–24.

R. Hunter (1977). Basic types of stratification in small eolian dunes. *Sedimentology* **24** (3), 361 – 387.

R. Hunter, B. Richmond, and T. Alpha (1983). Storm-controlled oblique dunes of the oregon coast. *Geological Society of America Bulletin* **94**, 1450 – 1465.

H. Jaeger, S. Nagel, and R. Behringer (1996). The physics of granular materials. *Physics Today* **49** (4), 32 – 38.

X. Jia, C. Caroli, and B. Velicky (1999). Ultrasound propagation in externally stressed granular media. *Physical Review Letters* **82** (9), 1863–1866.

G. Joseph and M. Hunt (2004). Oblique particle-wall collisions in a liquid. *Journal of Fluid Mechanics* **510**, 71–93.

J. Kakalios (2004). Resource letter gp-1: Granular physics or nonlinear dynamics in a sandbox. *American Journal of Physics* **73** (1), 8 – 22.

M. Curzon of Kedleston (1923). *Tales of travel.* reprinted in 1923 by Century Publishing.

G. Kocurek (1991). Interpretation of ancient eolian sand dunes. *Annual review of Earth and Planetary Sciences* **19**, 43–75.

G. Kocurek (1996). Desert aeolian systems, in sedimentary environments: processes, facies, and stratigraphy .

N. Lancaster (1996). Response of eolian geomorphic systems to minor climate change: examples from the southern californian deserts. *Geomorphology* **19**, 333–347.

T. Lay and T. Wallace (1995). *Modern global seismology.* Academic Press Limited.

O. Lenz (1912). Reise durch marokko, die sahara und den sudan. *The Geographical Journal* **39**, 133–134.

S. Leprince, S. Barbot, F. Ayoub, and J.-P. Avouac (2007). Automatic and precise orthorectification, coregistration, and subpixel correlation of satellite images, application to ground deformation measurements. *IEEE Transactions on Geoscience and Remote Sensing* **45** (6), 1529–1558.

A. Lewis (1936). Roaring sands of the kalahari desert. *South African Geographical Society* **19**, 33 – 49.

J. Lindsay, D. Criswell, T. Criswell, and B. Criswell (1976). Sound-producing dune and beach sands. *Geological society of America Bulletin* **87** (3), 463–473.

I. Livingstone (1987). Grain-size variations on a "complex" linear dune in the namib desert: in desert sediments: Ancient and modern .

A. A. MacDonald (1966). The dumont dune system of the northern mojave desert, california.

F. MacKenzie (1964). Geometry of bermuda calcareous dune cross-bedding. *Science* **144**, 1449–1450.

E. McKee (1977). An introduction to the study of global sand seas. *U. S. Geological Survey Paper* **1052** (3), 1 – 20.

P. Mills and F. Chevoir (2009). *Rheology of granular materials and sound emission near the jamming transition, in Powders and Grains 2009*. AIP conference proceedings.

S. Miwa and T. Okazaki (1995). Sound of booming dunes in china and america. *Sand Dune Research (Japanese)* **42**, 20.

S. Miwa, T. Okazaki, and M. Kimura (1995). Evaluation of the sound-producing properties of singing sand. *The Science and Engineering Review of Doshisha University* **36**, 67–76.

B. Muite, S. Quinn, and S. Sundaresan (2004). Silo music and silo quake: Granular flow induced vibration. *Powder Technology* **145**, 190–202.

S. Namikas and D. Sherman (1995). A review of the effects of surface moisture content on aeolian sand transport, in desert aeolian processes .

U. Nations (2009). Un global climate report. Technical report, United Nations Convention to Combat Desertification.

V. Nesterenko (2001). *Dynamics of heterogeneous materials*. Springer New York.

J. Nielson and G. Kocurek (1987). Surface processes, deposits, and development of star dunes: Dumont dune field, california. *Geological Society of America Bulletin* **99**, 177–186.

F. Nori, P. Sholtz, and M. Bretz (1997). Booming sand. *Scientific American* **277** (3), 84–89.

C. Officer (1958). *Introduction to the theory of sound transmission with application to the ocean.* McGraw-Hill Book company Inc.

A. Patitsas (2003). Booming and singing acoustic emissions from fluidized granular beds. *Journal of fluid structures* **17**, 287–315.

A. Patitsas (2008). Singing sands, musical grains and booming sand dunes. *Journal of Physical and Natural Sciences* **2** (1), 1–25.

B. Pavlik (1980). Patterns fo water potential and photosynthesis of desert sand dune plants, eureka valley, california. *Oecologia* **46** (2), 147–154.

B. Pavlik (1989). Phytogeography of sand dunes in the great basin and mojave deserts. *Journal of Biogeography* **16**, 227–238.

M. Peel, B. Finlayson, and T. McMahon (2007). Updated world map of the köppen-geiger climate classification. *Hydrol. Earth Syst. Sci.* **11**, 1633–1644.

F. Peters (1996). *Hajj, the muslim pilgrimage to Mecca and the holy places.* University Press Princeton.

M. Polo (1295). *The Travels of Marco Polo.* reprinted in 1984 by Facts on file Inc.

J. Poynting and J. Thompson (1909). *Textbook of physics: sound.* Charles Griffin and company.

J. Reynolds (1997). *An introduction to applied and environmental geophysics.* John Wiley and Sons.

K. Ridgway and J. Scotton (1973). Whistling sand beaches in the british isles. *Sedimentology* **20**, 263 – 279.

C. Schenk, D. Gautier, G. Olhoeft, and J. Lucius (1993). Internal structure of an aeolian dune using ground-penetrating radar. *Special publication no. 16 of the international association of sedimentologists* **16**, 61–69.

W. Shaw (1936). An expedition in the southern libyan desert. *The Geographical Journal* **87**, 209.

P. Sholtz, M. Bretz, and F. Nori (1997). Sound-producing sand avalanches. *Contemporary physics* **38** (5), 329–342.

N. Sleep and K. Fujita (1997). *Principles of geophysics*. Blackwell Science.

M. Slotnick (1959). *Lessons in Seismic Computing*. The society of Exploration Geophysicists.

H. Takahara (1973). Sounding mechanism of singing sand. *Journal of the acoustical society of America* **53** (2), 634 – 639.

B. Thomas (1932). *Across the mountainous sands of Uruq-Adh-Dhahiya in Arabia Felix*. J. Cape London.

D. Thomas (1987). Discrimitation of depositional environments using sedimentary characteristics in the mega kalahari, central southern africa: in desert sediments: Ancient and modern .

M. Tischer, M. Bursik, and E. Pitman (2001). Kinematics of sand avalanches using particle-image velocimetry. *Journal of Sedimentary Research* **71** (3), 355 – 364.

S. Tomlin (1999). Vast snow dunes frozen in time. *Nature* **402**, 860.

D. Trexler and W. Melhorn (1986). Singing and booming land dunes of california and nevada. *California Geology* **39** (7), 147–152.

J. Vidale (1986). Complex polarization analysis of particle motion. *Bulletin of the Seismological Society of America* **76** (5), 1393–1405.

N. Vriend, M. Hunt, and R. Clayton (2010a). Dune stratigraphy of dumont and eureka dunes - geophysical evidence of booming sand dunes. *In preparation* .

N. Vriend, M. Hunt, and R. Clayton (2010b). Linear and nonlinear wave propagation in booming sand dunes. *In preparation* .

N. Vriend, M. Hunt, R. Clayton, C. Brennen, K. Brantley, and A. Ruiz-Angulo (2007). Solving the mystery of booming sand dunes. *Geophysical Research Letters* **34** (16), L16306.

N. Vriend, M. Hunt, R. Clayton, C. Brennen, K. Brantley, and A. Ruiz-Angulo (2008). Reply to comment on solving the mystery of booming sand dunes. *Geophysical Research Letters* **35**, L08307.

S. Wentworth (1922). A scale of grade and class terms for clastic sediments. *Journal of Geology* **30**, 377–392.

G. Whitham (1974). *Linear and Nonlinear waves*. John Wiley and Sons.

R. Williams (2004). Unearthing the mechanics of burping sands. Surf-report, California Institute of Technology.

A. Yate (1897). Sand-dunes. *The Geographical Journal* **9**, 672–673.